2 p (mix)

NATIONAL AERONAUTICS AND SPACE ADMINISTRATION

Technical Memorandum 33-598

Evaluation of the Electro-optic Direction Sensor

Final Report

Alan R. Johnston
Phil M. Salomon

JET PROPULSION LABORATORY
CALIFORNIA INSTITUTE OF TECHNOLOGY
PASADENA, CALIFORNIA

February 1, 1973

128

TECHNICAL REPORT STANDARD TITLE PAGE

1. Report No. 33-598	2. Government Accession No.	3. Recipient's Catalog No.
4. Title and Subtitle EVALUATION OF THE ELECTRO-OPTIC DIRECTION SENSOR FINAL REPORT		5. Report Date February 1, 1973 6. Performing Organization Code
7. Author(s) Alan R. Johnston, Phil M. Salomon		8. Performing Organization Report No.
9. Performing Organization Name and Address JET PROPULSION LABORATORY California Institute of Technology 4800 Oak Grove Drive Pasadena, California 91103		10. Work Unit No. 11. Contract or Grant No. NAS 7-100 13. Type of Report and Period Covered Technical Memorandum
12. Sponsoring Agency Name and Address NATIONAL AERONAUTICS AND SPACE ADMINISTRATION Washington, D.C. 20546		14. Sponsoring Agency Code

15. Supplementary Notes

16. Abstract

Evaluation of a no-moving-parts single-axis star tracker called an electro-optic direction sensor (EODS) concept is described and the results are given in detail. The work involved experimental evaluation of a breadboard sensor yielding results which would permit design of a prototype sensor for a specific application. The Laboratory work included evaluation of the noise equivalent input angle of the sensor, demonstration of a technique for producing an acquisition signal, constraints on the useful field-of-view, and a qualitative evaluation of the effects of stray light. In addition, the potential of the silicon avalanche-type photo diode for this application was investigated. No benefit in noise figure was found but the easily adjustable gain of the avalanche device was useful. The use of mechanical tuning of the modulating element to reduce voltage requirements was also explored. The predicted performance of EODS in both photo-multiplier and solid state detector configurations was compared to an existing state-of-the-art star tracker.

17. Key Words (Selected by Author(s))	18. Distribution Statement
Control and Guidance Optics	Unclassified -- Unlimited

19. Security Classif. (of this report)	20. Security Classif. (of this page)	21. No. of Pages	22. Price
Unclassified	Unclassified	92	

HOW TO FILL OUT THE T[illegible]ORT STANDARD TITLE PAGE

Make items 1, 4 [illegible]3 agree with the corresponding information on the report cover [illegible] letters for title (item 4). Leave items 2, 6, and 14 blank. [illegible]maining items as follows:

[illegible]nt's Catalog No. Reserved for use by report recipients.

Author(s). Include corresponding information from the report cover. In addition, list the affiliation of an author if it differs from that of the performing organization.

8. Performing Organization Report No. Insert if performing organization wishes to assign this number.

10. Work Unit No. Use the agency-wide code (for example, 923-50-10-06-72), which uniquely identifies the work unit under which the work was authorized. Non-NASA performing organizations will leave this blank.

11. Insert the number of the contract or grant under which the report was prepared.

15. Supplementary Notes. Enter information not included elsewhere but useful, such as: Prepared in cooperation with... Translation of (or by)... Presented at conference of... To be published in...

16. Abstract. Include a brief (not to exceed 200 words) factual summary of the most significant information contained in the report. If possible, the abstract of a classified report should be unclassified. If the report contains a significant bibliography or literature survey, mention it here.

17. Key Words. Insert terms or short phrases selected by the author that identify the principal subjects covered in the report, and that are sufficiently specific and precise to be used for cataloging.

18. Distribution Statement. Enter one of the authorized statements used to denote releasability to the public or a limitation on dissemination for reasons other than security of defense information. Authorized statements are "Unclassified—Unlimited," "U. S. Government and Contractors only," "U. S. Government Agencies only," and "NASA and NASA Contractors only."

19. Security Classification (of report). NOTE: Reports carrying a security classification will require additional markings giving security and downgrading information as specified by the Security Requirements Checklist and the DoD Industrial Security Manual (DoD 5220.22-M).

20. Security Classification (of this page). NOTE: Because this page may be used in preparing announcements, bibliographies, and data banks, it should be unclassified if possible. If a classification is required, indicate separately the classification of the title and the abstract by following these items with either "(U)" for unclassified, or "(C)" or "(S)" as applicable for classified items.

21. No. of Pages. Insert the number of pages.

22. Price. Insert the price set by the Clearinghouse for Federal Scientific and Technical Information or the Government Printing Office, if known.

NATIONAL AERONAUTICS AND SPACE ADMINISTRATION

Technical Memorandum 33-598

Evaluation of the Electro-optic Direction Sensor

Final Report

Alan R. Johnston
Phil M. Salomon

JET PROPULSION LABORATORY
CALIFORNIA INSTITUTE OF TECHNOLOGY
PASADENA, CALIFORNIA

February 1, 1973

Prepared Under Contract No. NAS 7-100
National Aeronautics and Space Administration

FOREWORD

This document is the final report covering a one-year investigation of an Electro-Optic Direction Sensor (EODS), a no-moving-parts single axis star-sensor.

The purpose of this document is to present a comprehensive set of results from the investigation. The results and conclusions are collected here under a single cover, and are given in greater detail than would be expected in a journal paper. This report should enable the reader to understand all facets of the work, and if desired, to duplicate the results. For the reader who is not interested in this level of detail, it will be sufficient to read the Introduction, Section I, and the Discussion, Section IX.

This task was supported by the Advanced Applications Flight Experiments Program, NASA Task No. 630-52-86-05-55. It was proposed in response to the Spring 1970 AFO, and falls under the Applications Technology portion of the AAFE program, and is concerned with sensing techniques for attitude control of satellites or spacecraft. The direction sensor task was an analytical and laboratory investigation directed toward establishing the capability of a new and untried Electro-Optical Direction sensing concept. No flight experiments were planned or conducted. The overall purpose of the work was to collect sufficient data through laboratory experimentation to permit a prototype sensor to be designed to a given set of requirements with a good level of confidence. The work was intended to show what applications could be advantageously served by EODS.

The feasibility of the concept was established during an R&AD effort preceding the initiation of the present AAFE task. The paper, "An Electro-Optic Direction Sensor," resulted from this early work, and has been included with this report as an addendum for convenient reference. A second paper, "Noise in the Electro-Optic Direction Sensor," covering the noise measurements is also appended.

Several specific objectives were identified:

1) Obtain data defining the noise-effective input angle of the sensor.
2) Determine the sensitivity of the breadboard EODS to stray light.
3) Evaluate the range of angular field-of-view that can be accommodated, and demonstrate an acquisition signal.
4) Identify a technique for lowering modulator drive voltage requirements by mechanical tuning of the modulator element.
5) Demonstrate a horizon tracker configuration of EODS.
6) Evaluate the relative merit of an avalanche type photodetector compared to a silicon PIN device.

Each of these topics is discussed in turn in the following sections. The experimental approaches used and the results obtained are presented. The pertinent conclusions in each area are discussed.

CONTENTS

ABSTRACT

Evaluation of a no-moving-parts single-axis star tracker called an electro-optic direction sensor (EODS) concept is described and the results are given in detail. The work involved experimental evaluation of a breadboard sensor yielding results which would permit design of a prototype sensor for a specific application. The Laboratory work included evaluation of the noise equivalent input angle of the sensor, demonstration of a technique for producing an acquisition signal, constraints on the useful field-of-view, and a qualitative evaluation of the effects of stray light. In addition, the potential of the silicon avalanche-type photo diode for this application was investigated. No benefit in noise figure was found but the easily adjustable gain of the avalanche device was useful. The use of mechanical tuning of the modulating element to reduce voltage requirements was also explored. The predicted performance of EODS in both photomultiplier and solid state detector configurations was compared to an existing state-of-the-art star tracker.

EVALUATION OF THE ELECTRO-OPTIC DIRECTION SENSOR

Alan R. Johnston
Phil M. Salomon
Jet Propulsion Laboratory

I. INTRODUCTION

General

Orientation by reference to fixed stars and also pointing of an instrument or device with respect to some luminous object is a common control problem. Many approaches have been successfully used in the past for these purposes, but significant improvements in a few areas would be very useful if they could be made available. Star sensors typically use either mechanical scanning or chopping, which tends to be cumbersone, or use detectors in a dc mode with its attendant drift problem, or employ image dissector tubes for the modulation function, which are expensive.

The Electro-Optic Direction Sensor, or EODS, represents an approach which has the potential for providing a considerably smaller, simpler, and presumably cheaper single axis star sensing device than is now available. A tracker 5 cm x 5 cm x 15 cm including electronics should be feasible. The possibility of using several individual star sensors in one optical orientation device thus appears to become practical to obtain redundancy, and, in the case of stars, to avoid the usual uncertainty with star identification. Alternatively, design of an EODS for highly precise tracking also appears to be possible.

Conversely, there are limitations inherent in the EODS type of sensor with regard to field-of-view, and also, because of unavoidable detector noise, with regard to the use of a solid-state detector. These points will be discussed in detail in the following sections.

A complete analysis of the EODS concept has been presented in a paper, "An Electro-Optic Direction Sensor," (ref. 1), and will not be repeated here. A very brief description of the principle of operation of EODS follows, but reference 1 should be consulted for further detail.

The electro-optic direction sensor (EODS) depends on the anisotropy of the refractive index of a pair of wave plates for its directional sensitivity. Quartz, calcite, KDP, or other uniaxial material may be used. One wave plate is cut with its optic axis at an angle to its surfaces, and, as a result, its retardation varies linearly on the direction of propagation. This plate has been called the Directional Wave Plate, or DWP. A second plate called the compensator, cut with the appropriate thickness and with its axis in the plane of its surfaces, is oriented for exact compensation on-axis. These two plates are placed between crossed polarizers along with an electro-optic modulator plate to form what is called the direction-sensitive modulator (DSM). Its transmission depends in sinusoidal fashion on angle, in rough analogy with interference fringes. Geometrically it behaves like a plane-parallel window. The function of the modulator element is to produce an ac photosignal by modulation of the DSM transmission function such that the angular position of a distant point source can be extracted by phase detection. Thus, the directional reference is embedded in the passive crystal optics and the detector is able to operate in an ac mode. The telescope serves as a light gathering function only.

Description of Breadboard Sensor

A number of figures follow, which illustrate the apparatus used to conduct all of the experimental work.

A breadboard sensor was constructed using optical bench hardware. It was convenient to space out the elements along the axis to facilitate independent adjustment of the orientation of each element. The electronics used for modulator drive and signal detection were commercial laboratory instrumentation. No attempt was made to package the sensor in a flight configuration.

An overall view of the bench is shown in figure 1. The collimator providing the simulated star is seen on the right. Its angular position was monitored by means of the dial gages shown. The star was simulated by means of a pinhole source illuminated by a ribbon-filament lamp. Filters were introduced behind the pinhole to adjust the color temperature to approximately 5500°K and to control the intensity.

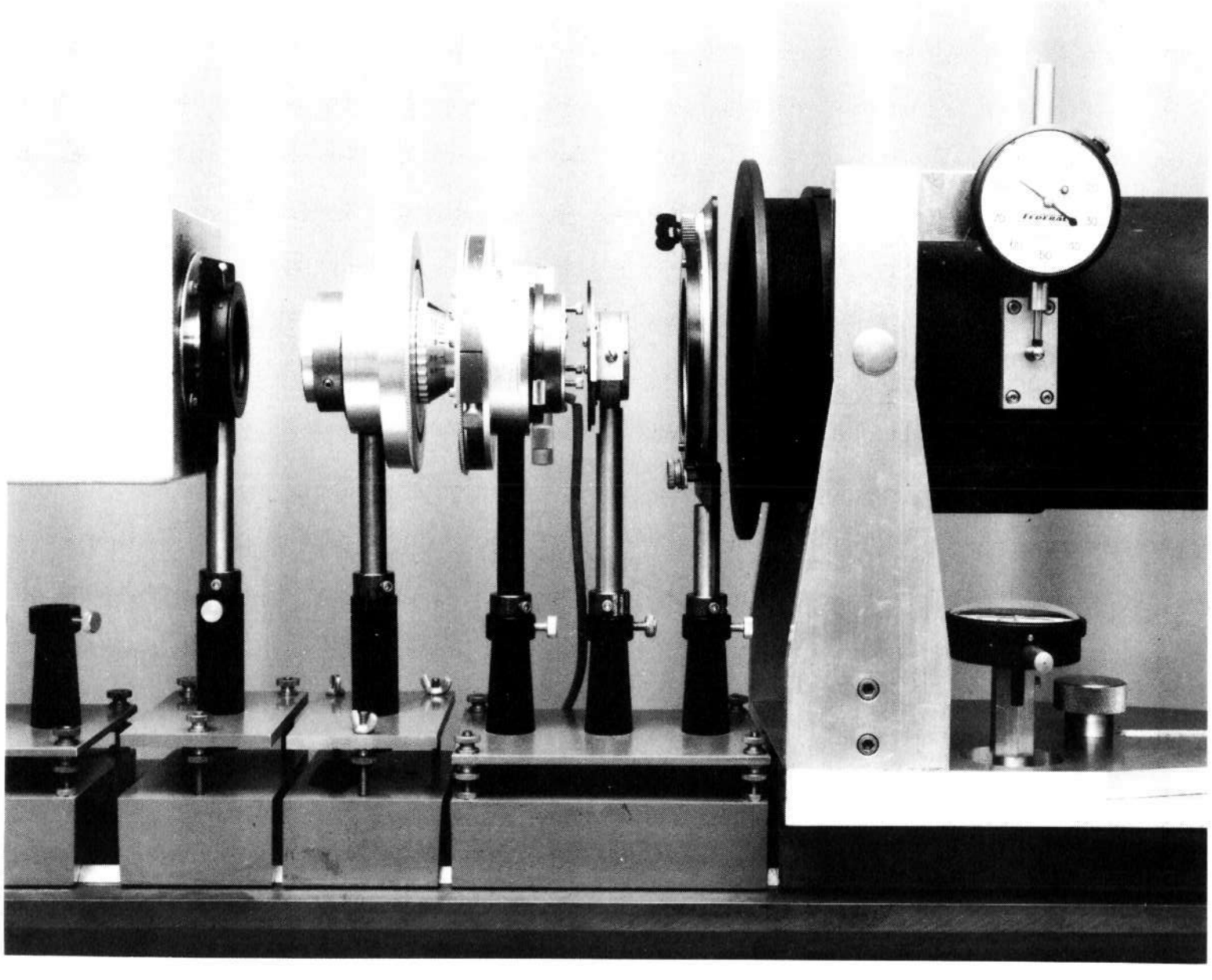

Figure 1. View of the Electro-Optic Direction Sensor (EODS) Laboratory Breadboard

A field stop and the photomultiplier housing are at the extreme left in the picture.

The geometrical configuration of the optical elements is shown in figure 2. The sketch is drawn to scale. The telescope lens was a commercial 100 mm efl f/4.5 enlarging lens, although it is shown in the sketch as a simple lens at the location of the stop. The limiting aperture in this apparatus is the 1 cm diameter of the wave plates.

Another view of the lab bench is shown in figure 3. In this configuration a solid state detector has been substituted for the photomultiplier. A microscope objective serves as a field lens, and there is no field stop other than the aperture of the microscope lens. The detector is mounted in a metal box for shielding. The box was mechanically supported and positioned by being attached to the PAR Type D high input impedance preamplifier ($R_i = 10^8\ \Omega$) for a HR-8 phase sensitive detector. A separate PAR Type 113 preamplifier was substituted in some of the runs, and yielded similar results. A closer view of the detector box and field lens is given in figure 4, and the detector with the cover removed in figure 5. Part of the biasing battery and load resistor can be seen beneath the baffle.

II. EVALUATION OF THE EQUIVALENT NOISE INPUT

An investigation of the signal-to-noise ratio to be expected from the EODS was conducted because the new modulation scheme which it employs is sufficiently different from that used in other forms of star trackers to make prior experience an unrealible indicator. Noise is a limiting factor in the application of a star tracker, because of the very low intensity of even the brightest stars. The noise superimposed on the output signal typically originates in the photodetector. At best, a tracker will be photon-noise limited due to the statistical nature of the light itself, a limitation that can be encountered in

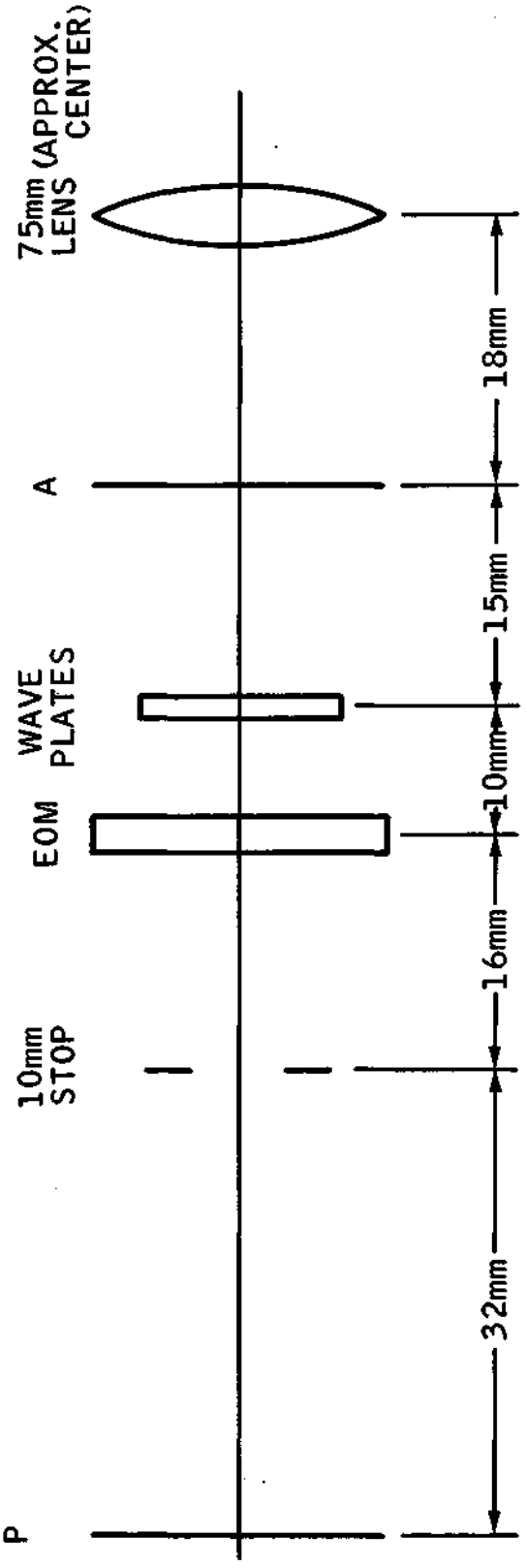

Figure 2. Geometric Layout of Direction Sensor

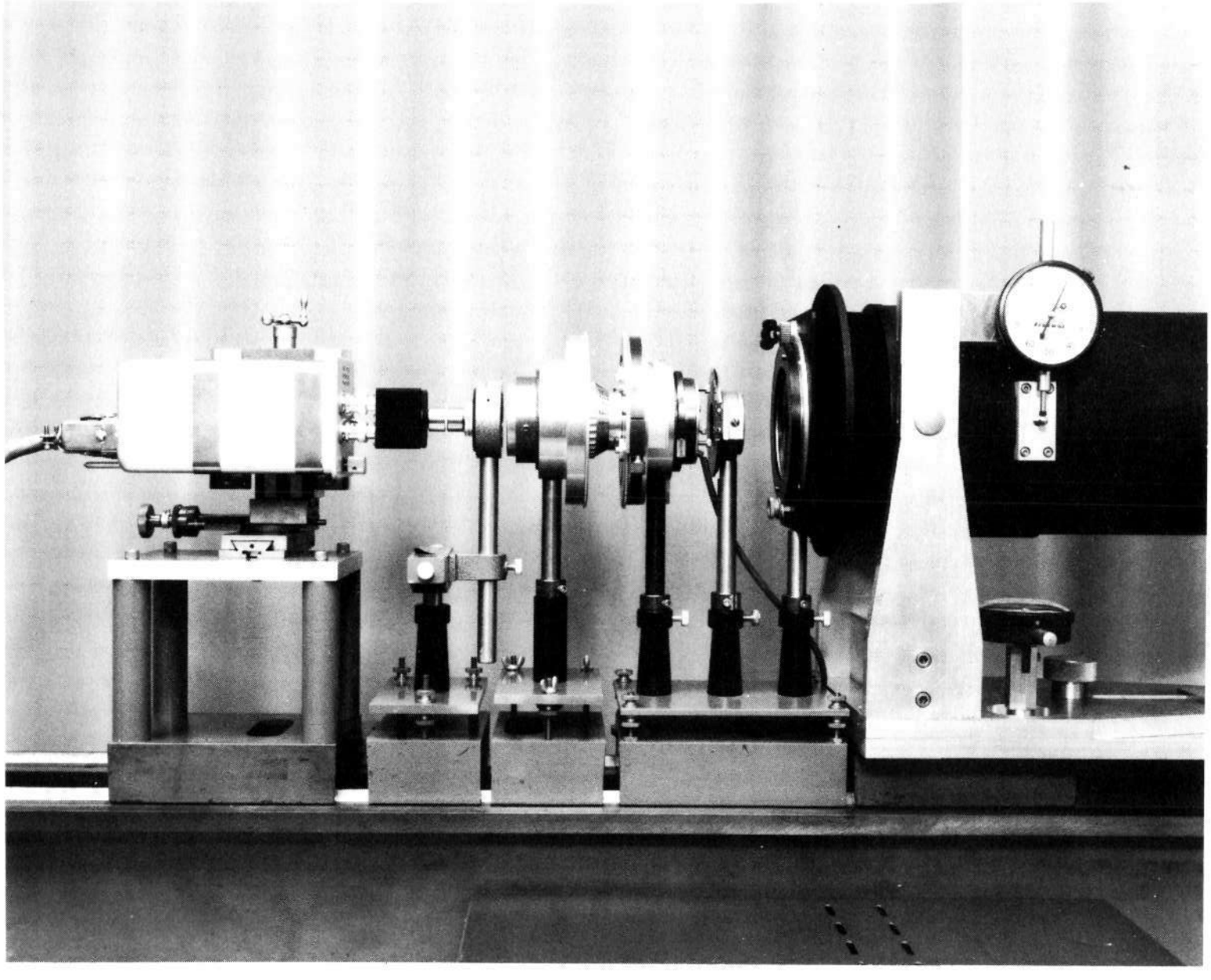

Figure 3. EODS Laboratory Breadboard Setup with a Solid-State Detector

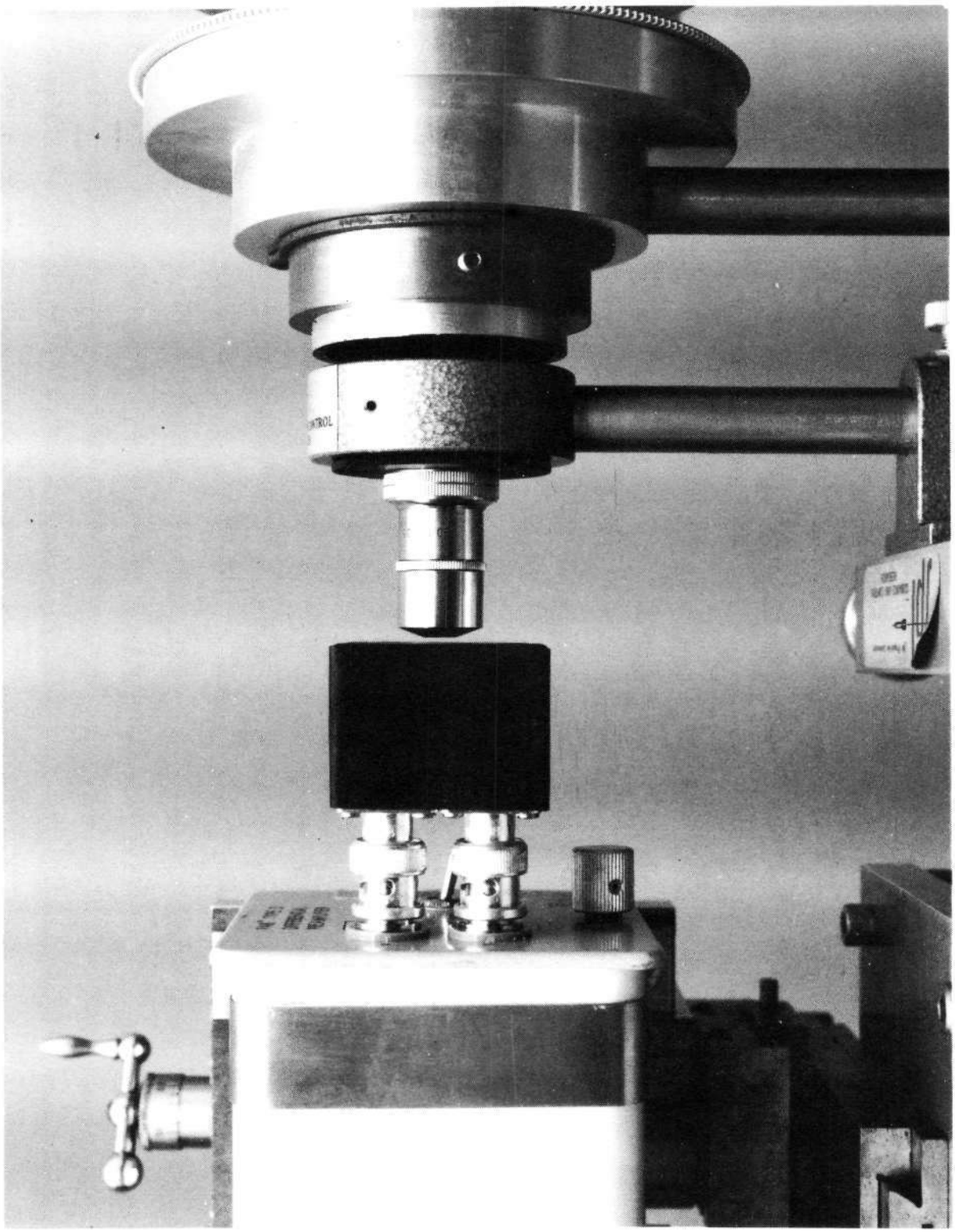

Figure 4. Close Up of the Micrioscope Objective used as a Field Lens, and the Detector Housing

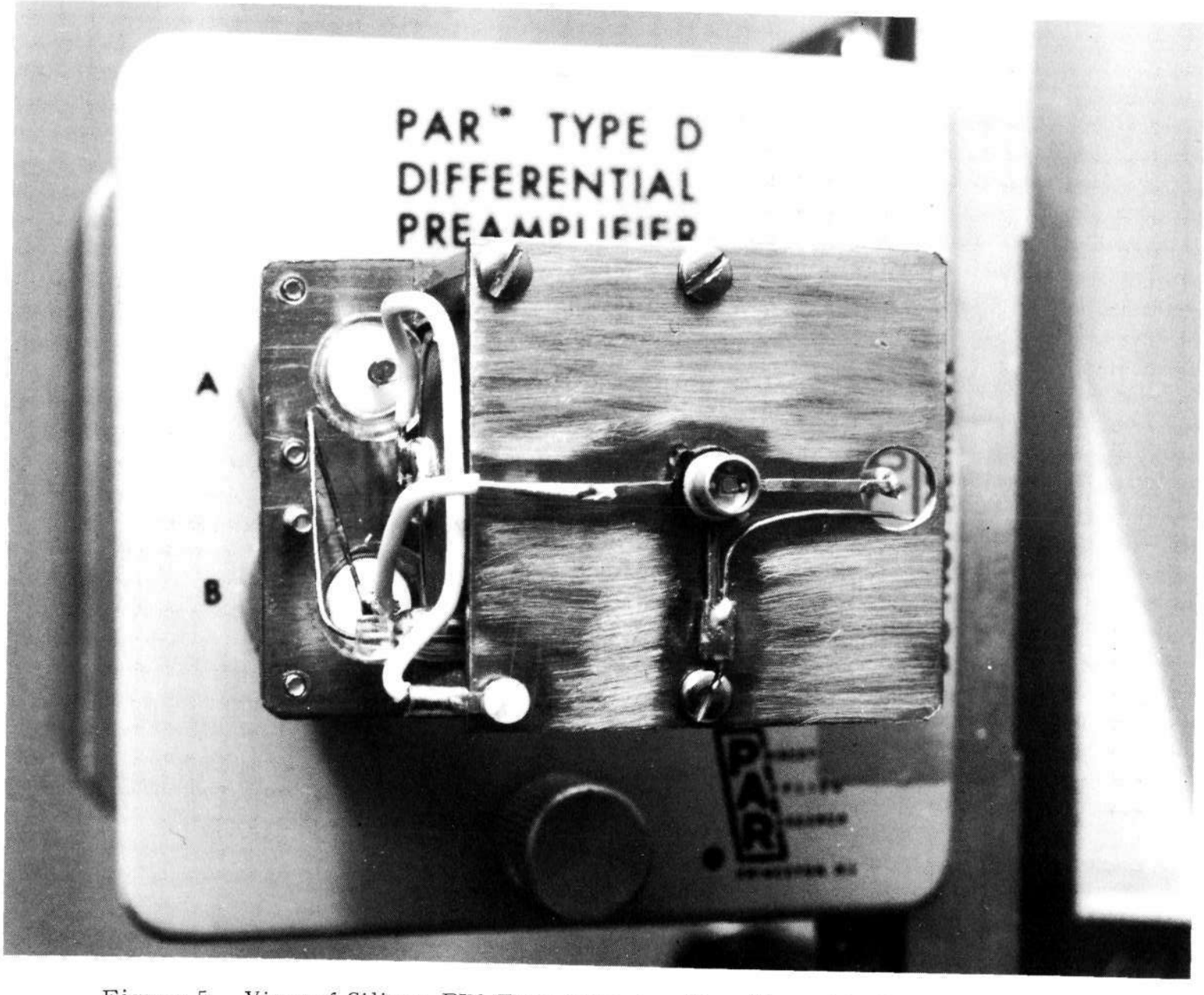

Figure 5. View of Silicon PIN Type Detector Mounting with Cover Removed

practice. Real detectors, particularly the small solid-state detectors that one would like to use, add their own noise, which may be orders of magnitude larger. Noise of course varies inversely as the square root of the response time of the sensor so that if a tighter pointing accuracy is required, slower response must be tolerated.

The problem addressed in this work was to determine the noise equivalent input angle (nea) of the EODS as a function of bandwidth, collected light flux, and other parameters. From this data, collecting aperture, detector type and sensor response time could be selected to fit a given application.

Both theoretical and empirical approaches were pursued. First, the noise equivalent input of a hypothetical ideal sensor was calculated to serve as a point of reference for comparison. The basic photon noise was calculated, as well as the noise effective angle with real photodetectors, which was calculated from detector N. E. P. and quantum efficiency data. The noise effective input angle of the EODS was then calculated and compared with the above. The calculated noise input for the EODS is larger because of the imperfect efficiency of its modulation scheme and transmission losses in its optics.

Noise inputs were then measured with the laboratory breadboard sensor, described in the Introduction, using both a representative photomultiplier and several different solid state detectors.

The detailed results are given in reference 2, and will not be repeated here.

The principal findings were first, that the calculated noise input was in agreement with experiment, thus lending confidence to the theoretical approach used, and secondly, the EODS is noisier by a factor of 3.5 than the ideal sensor under the same conditions. This factor is not unduly large, and is a reasonable price to pay for the benefits of a no-moving-parts ac photodetector operation.

The information necessary for sizing the components of an EODS sensor for a specific application is summarized in figure 6, which is reproduced from reference 2. The data in the figure was calculated, but as mentioned above, they agree satisfactorily with experiment. The equivalent noise input is normalized by the factor α_{max} representing the full-scale angular range of the sensor.

Thus, the noise is expressed as a fraction of the full-scale sensor output, which is like an inverse signal-to-noise ratio. A narrower field of view inherently results in smaller noise when measured in angular units. All the data shown are for τ = 1 sec; different time constants change the equivalent noise input proportional to $\tau^{-1/2}$. The time constant τ may be interpreted in two ways; either as the time constant of the sensor output, in which case the equivalent noise angle applies to the sensor output signal; or τ may be considered a control loop time constant, and the noise as the fluctuation in the orientation of the controlled inertia.

In the context of a practical application, the EODS, when incorporating a photomultiplier detector, can easily track the brightest stars with a 1 cm^2 aperture. However, to fully realize the potential of the concept, one would like to combine it with a compact solid-state detector. Our results indicate that this is possible, but that a considerably larger collecting aperture would be necessary. If a 1 sec time constant is assumed, 4 cm diameter optics could be used with a zero magnitude star. Thus, a trade-off is necessary between the size and complexity of the detector and the size of the collecting optics themselves.

It is also implicit that the use of a solid-state detector involves state-of-the-art design of the detector-preamp combination; not an important consideration when using a photomultiplier.

A separate effort was made to determine whether an avalanche type of photodetector could offer significant advantages over the silicon PIN type used

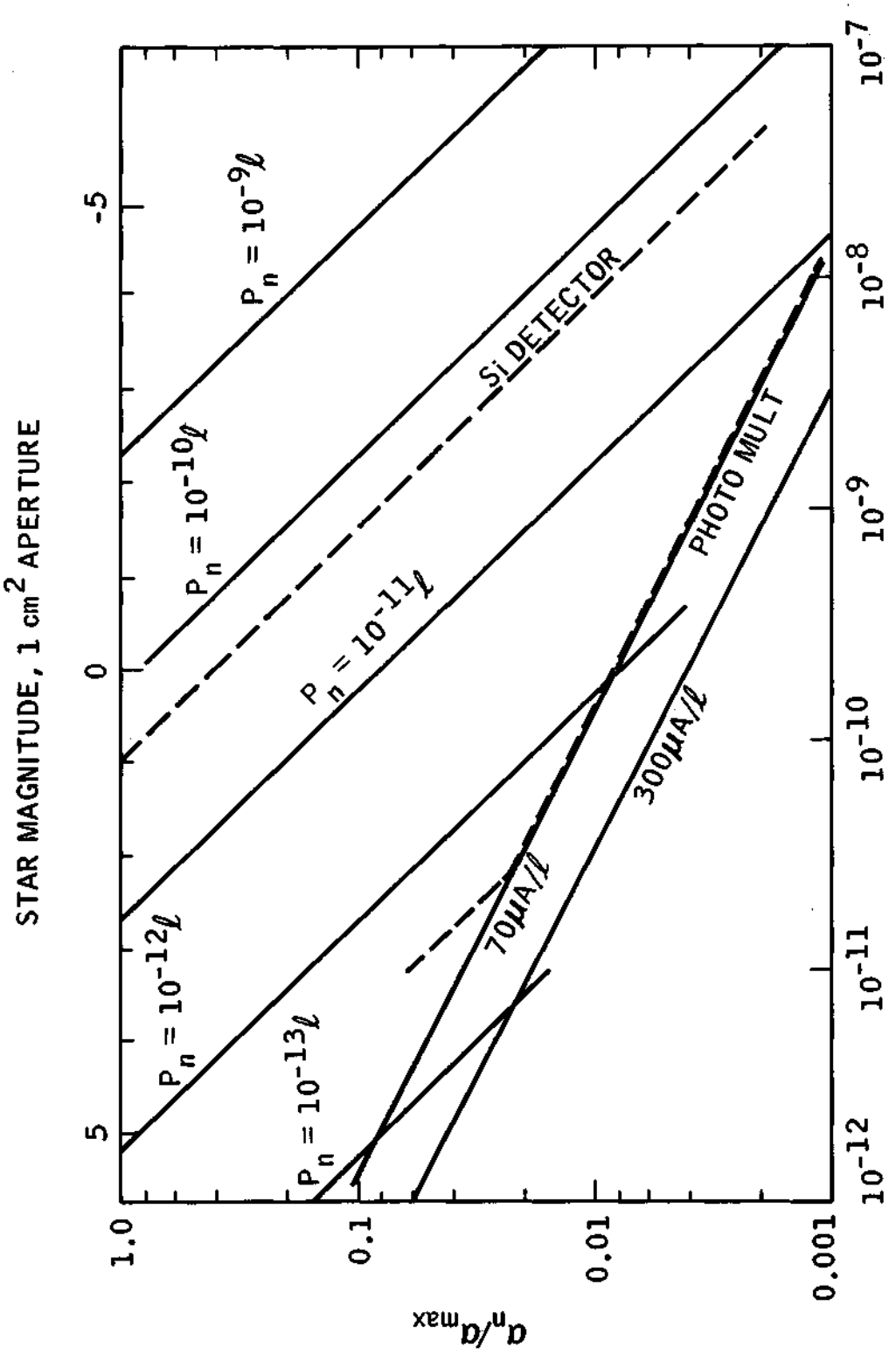

Figure 6. Noise Equivalent Input Angle of an EODS Star Tracker as a Function of Collected Flux and Detector Characteristics

in the above study. This involved measuring detector N. E. P. for the specific operating conditions encountered in the EODS. Results from this investigation will be described below in a separate section.

III. SILICON AVALANCHE PHOTODIODE EVALUATION

Background

The primary objective of this phase of the investigation was to evaluate the suitability of silicon avalanche photodiodes to serve as detectors in the Electro-Optic Direction Sensor. The principle parameters to be evaluated included noise-equivalent luminance, responsivity, avalanche gain, and dynamic output resistance. All measurements were to be made at light flux levels which are representative of star tracking operations in typical spacecraft flight situations.

Avalanche photodiodes are wide-band devices, with frequency response determined by the finite time required to collect the secondary holes and electrons. This time is approximately one half the transit time through the depletion region; on the order of 1×10^{-12} seconds for silicon. The gain-bandwidth product of the internal gain process can be 100 GHz. Avalanche photodiodes with active areas of 1.8×10^{-2} cm^2 (~1-1/2 mm diameter) are currently available for evaluation.

Noise is added to the light-induced signal because of the statistical nature of the avalanche process. The noise figure increases with gain, but significant improvements in signal-to-noise ratio are still obtained with avalanche multiplication because the excess noise is always much smaller than the noise of the following amplifier stage.

The dominant noise source is dark current, arising from both leakage current through the bulk diode material, and from surface leakage between electrodes. The internal leakage current is amplified by the gain process,

while the surface leakage is not. Improvement in overall noise figure can be obtained in three ways. By maximizing the gain, the contribution of surface leakage is made less important. This step was taken in making gain measurements, and can also be easily done in practice. Once the avalanche multiplication is optimized, the diode dark current becomes the limiting parameter, and further improvements in sensitivity can only be realized through cooling the diode, or by reducing the surface leakage in manufacture.

Because of the extremely fast response time of the silicon avalanche diode, the device is typically used as a wideband photon detector. To obtain high speed performance, it is necessary to use a low impedance preamplifier. Under these conditions, the ultimate sensitivity of the diode may be degraded because of the input noise current from the low resistance circuit. In the case of the EODS detector, the response time requirements are quite modest and the avalanche detector can operate into a high impedance preamplifier. Noise data obtained under these conditions was not found in the literature.

Experimental Results

Four silicon avalanche photodiodes were selected for evaluation as representative of the current art in the manufacture of these types of devices. Two of the photodiodes were designated TIXL59, while the other two were designated TIXL69 (ref. 10). The principal difference between the two types is that the TIXL69 has fourfold increase in sensitive area over the TIXL59.

Prior to evaluating the photodiodes, it was necessary to design and fabricate a high-voltage bias regulator. The bias regulator included a closed-loop solid-state regulator circuit with output current limiting. Very precise regulation of the voltage applied to the detector was necessary during all tests because of the sensitivity of photodiode characteristics to applied voltage when operating in the avalanche region. A schematic diagram of the bias regulator is shown in figure 7.

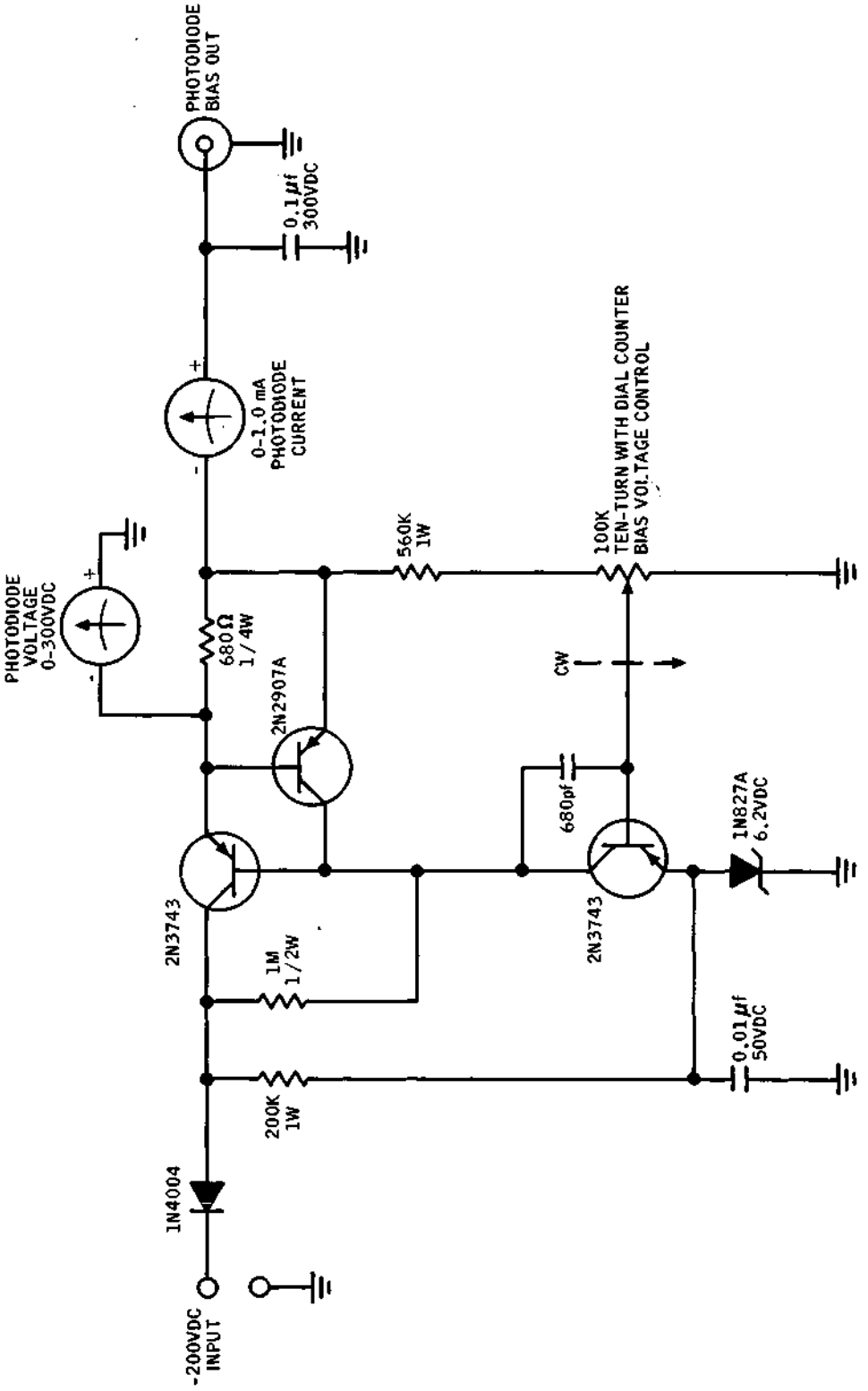

Figure 7. Bias Voltage Control and Current Limiter

A special test fixture was designed to provide a shielded mounting for the avalanche photodiode and to allow coupling of the output signal to a low-noise preamplifier (PAR Type D). The test fixture provided a differential readout of the signal voltage to reject any common-mode signals such as power supply ripple, extraneous signal pickup, etc. The schematic details of the test fixture are shown in figure 8.

The optical stimulus used in the evaluations consisted of a collimated point source whose intensity was carefully measured prior to the evaluations. Source control was maintained by metering the collimator lamp current and making any required brightness changes by means of neutral density filters. The collimated point source was chopped by a mechanical chopping wheel (PAR Model 222) and then imaged on the sensitive area of the avalanche photodiode under test. A Wollensak Raptar lens having a 75 mm focal length was used as the final imaging device.

Measurements of the avalanche diode output were made with a PAR Type HR-8 Lock-In Amplifier. Measurements of noise voltage were made with a pen recorder to allow an accurate estimate of the rms value to be made. Noise voltage was also measured with the avalanche bias removed to allow evaluation of the test equipment noise contribution. The chop frequency was 80 Hz, and the measurement bandwidth was 0.125 Hz.

Avalanche photodiode evaluations consisted of determining noise-equivalent luminance, responsivity, and output resistance. Each of these parameters was measured as a function of bias voltage, input illumination, and load resistance. The measured parameters were strongly bias-dependent with each avalanche photodiode exhibiting an optimum bias voltage for maximum responsivity.

Table I lists the measurement results for the four avalanche photodiodes tested. In each case, responsivity of greater than one amp/lumen was obtained with a noise-equivalent luminance of typically 10^{-12} lumens/$\sqrt{\text{Hz}}$. Values of avalanche gain in excess of 10^{-3} were recorded for all devices tested, with

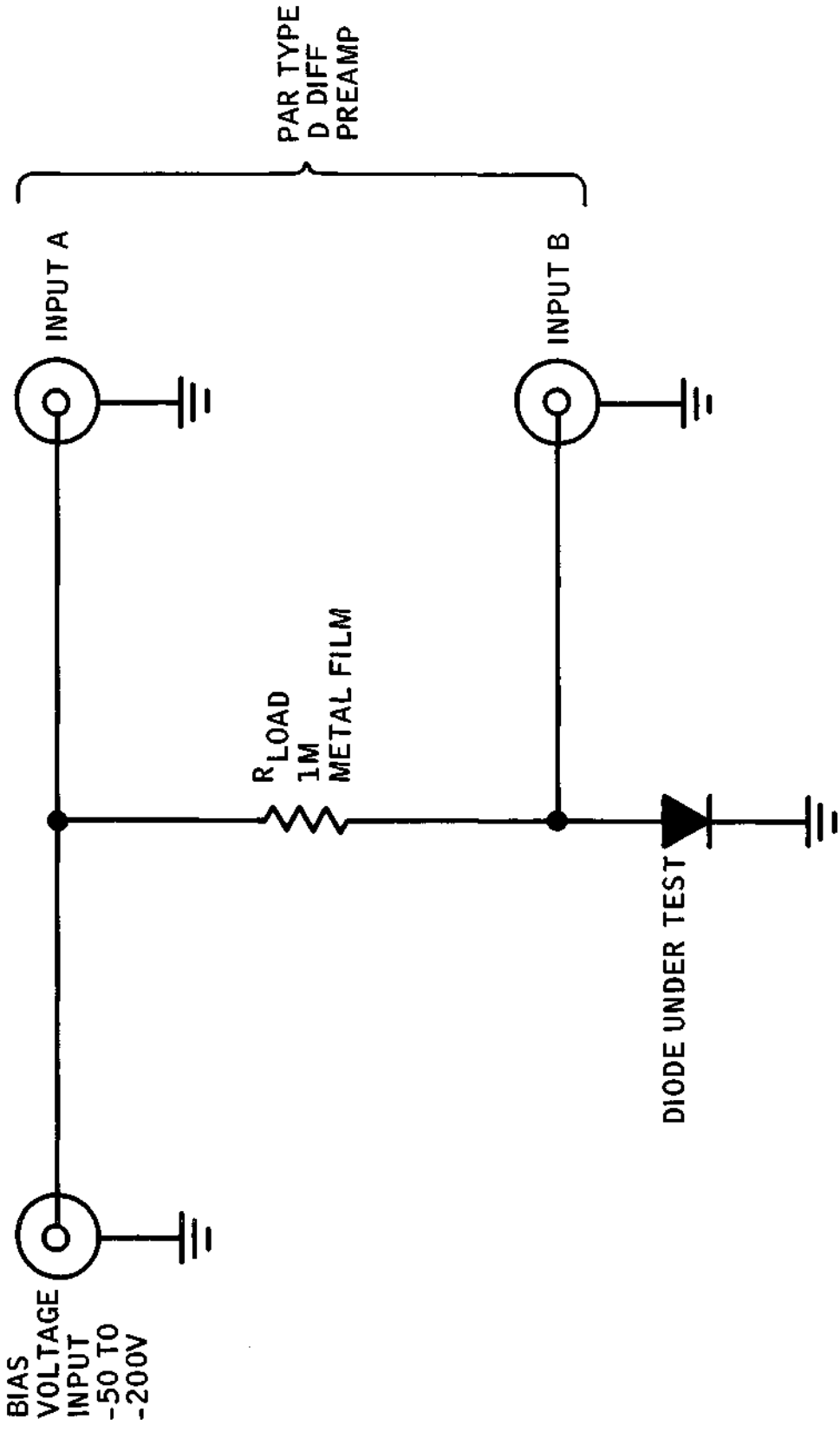

Figure 8. Photodiode Test Fixture Details

TABLE I – AVALANCHE DIODE DATA SUMMARY

Performance Tests at Optimum Bias						
Item	Parameter	T1XL69 No. 1	T1XL69 No. 2	T1XL59 No. 2	T1XL59 No. 5	Comments
1.	Optimum Bias	-159 v	-152 v	-153 v	-152 v	±3 percent reading accuracy
2.	NEP $\left(\frac{\text{lumen}}{\sqrt{\text{Hz}}}\right)$	8.0×10^{-11}	8.9×10^{-11}	4.1×10^{-10}	3.9×10^{-12}	Flux level was 1.7×10^{-8} lumen (T1XL69) and 1.0×10^{-7} lumen (T1XL59)
3.	NEP $\left(\frac{\text{lumen}}{\sqrt{\text{Hz}}}\right)$	2.1×10^{-11}	1.9×10^{-11}	5.3×10^{-11}	1.8×10^{-11}	Flux level for T1XL69 devices was 1.5×10^{-10} lumens, and 1.1×10^{-9} for T1XL59
4.	R (amp/lumen)	3.44	5.06	2.73	9.6	
5.	Avalanche Gain	2120	1950	4833	5368	Flux level was 1.7×10^{-8} lumen (T1XL69) and 1.0×10^{-7} lumen (T1XL59)
6.	Avalanche Gain	3604	3463	4605	2812	Flux level was 1.5×10^{-10} lumen (T1XL69) and 1.1×10^{-9} lumen (T1XL59)
7.	S/N Ratio	20	22	56	162	
8.	Output Resistance	>100 M	>100 M	>100 M	>100 M	Measurements not accurate above 100 M.

considerable variation being exhibited between devices. The dynamic output resistance of all devices was greater than 100 megohms at the operating bias point listed in Table I with a reduction in output resistance occurring as the bias voltage was reduced. The noise-equivalent luminance was relatively independent of the value of the load resistor used.

Summary. — The use of a silicon avalanche photodiode in place of the photomultiplier offers many attractive possibilities for the EODS. The most significant of these is probably the reduction in size and weight that would result from using an avalanche photodiode. Another definite advantage would result from the elimination of high-voltage power supplies normally required by photomultipliers along with their attendant corona discharge and insulation breakdown problems.

Silicon avalanche photodiodes are rugged, long-lived, require very little operating power, and have wideband spectral response characteristics. They do not suffer overload or fatigue failures as do photomultipliers. The ability to vary the sensitivity of the avalanche photodiode by changing the bias voltage allows automatic gain control to be incorporated as has been done with photomultipliers in the past.

IV. DEMONSTRATION OF AN ACQUISITION SIGNAL

Objective

A laboratory demonstration of means for producing an acquisition signal with the EODS is described in this section. The acquisition signal indicates the presence of the reference source in the useful field of the sensor. It is separate from the primary tracking signal. In a control system, it would be used to actuate a switchover between a search mode and a tracking mode. The same acquisition signal may also be used to help in identifying the star being tracked because at null it is proportional to brightness.

The objective of this part of our work was to demonstrate with the EODS a means for obtaining an acquisition signal, and to determine whether the signal to noise ratio obtainable is acceptable. Our present conclusion is that the amplitude of the component of the photosignal at the second harmonic of the modulator drive frequency should be used as the acquisition signal. Since the amplitude of the second harmonic (2ω) component of the photosignal is less than the fundamental, it is important to show that a source bright enough to track is also bright enough to produce an acquisition signal.

Although the dynamics of the acquisition process are not considered, it is assumed to be desirable for the tracker to provide a valid control signal over as wide an angular field as possible. The system must be able to switch to a tracking mode and stop a search sweep before the reference object passes from the field-of-view. Thus, in general, there is an inverse relationship between field-of-view and the time required for acquisition. Brief consideration was given to optical means for extending the field, but use of the 2ω acquisition signal in combination with the primary error signal is felt to be preferable. This scheme will be described further below.

Analysis

An analysis has been made of the EODS optics to obtain the expected photosignal as a function of the angle α between the reference star and sensor axis (ref. 1). The result, taken from that paper, is:

$$\frac{I}{I_O} = 1/2 - 1/2 \cos\left(\frac{\pi}{2}\frac{\alpha}{\alpha_{max}}\right) J_0(\Gamma_{mo}) - \sin\left(\frac{\pi}{2}\frac{\alpha}{\alpha_{max}}\right) J_1(\Gamma_{mo}) \sin\omega t - \cos\left(\frac{\pi}{2}\frac{\alpha}{\alpha_{max}}\right) J_2(\Gamma_{mo}) \cos 2\omega t + \text{higher harmonics} \quad (1)$$

I represents the time-dependent modulated light flux incident on the detector, and I_o is the total flux transmitted by the polarizer. I_o is half the incident unpolarized flux because of the attenuation of the polarizer for unpolarized light.

The above expression shows that the photosignal will be composed of a dc component plus a series of harmonics of the modulator drive frequency ω. The relative amplitude of the harmonics depends on the modulator drive, which determines the quantity Γ_{mo}, the peak amplitude of the sinuosoidal retardation of the modulating element.

An acquisition signal could be obtained either from the average value of the photosignal, the first two terms in eq. 1, or from the 2ω component. However, it is desirable to avoid dc operation of the photodetector, so our attention was directed toward the 2ω component.

The magnitude of the 2ω and 1ω terms may be compared by referring to eq. (1). Since both terms vary with α, but in a different way, the maximum amplitude of each term is compared.

$$\frac{V_a(\max)}{V_o(\max)} = \frac{J_2(\Gamma_{mo})}{J_1(\Gamma_{mo})} \tag{2}$$

The quantity V_a represents the acquisition signal, which is proportional to $(I)^{2\omega}$ and is largest when $\alpha = 0$. Similarly, V_o is the control output, which is proportional to $(I)^{\omega}$ and is largest at $\alpha = \alpha_{max}$. The ratio is plotted in figure 9 as a function of Γ_{mo}. At a modulator drive of $\Gamma_{mo} = 0.9$, a typical operating level, the magnitude of the second harmonic signal is seen to be about 1/4 of the fundamental.

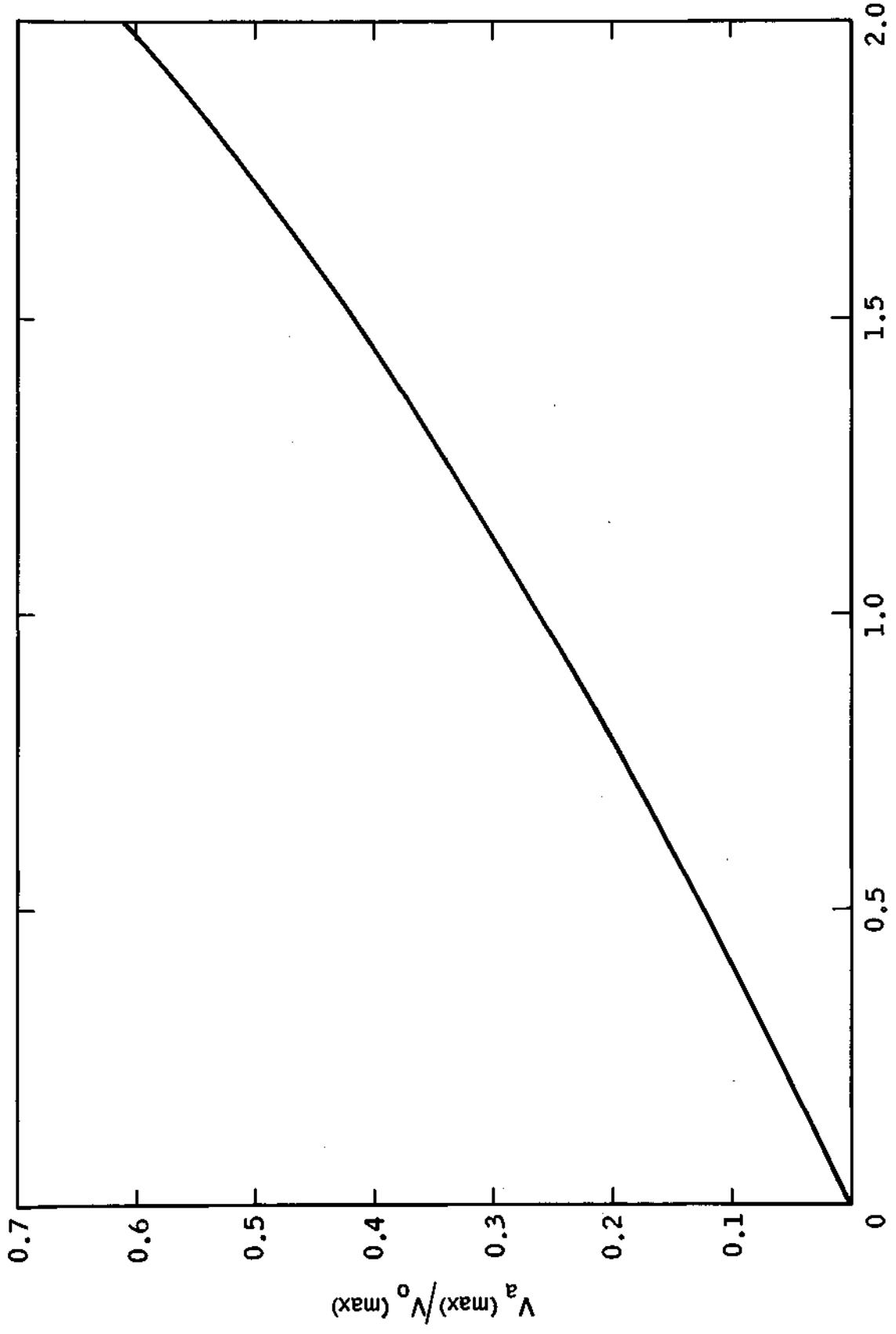

Figure 9. Ratio of the Second Harmonic Component of the Photosignal to the Fundamental

Laboratory Demonstration

The 2ω acquisition signal was demonstrated using the electronics illustrated in block diagram form in figure 10. Note that figure 10 is the same as figure 3 from reference 1 except that additions from which the V_a output is provided have been inserted. The two phase sensitive detectors measured the amplitude of the 1ω and 2ω harmonics separately. The modulator frequency was doubled by a simple diode bridge before supplying it as the reference for the 2ω phase sensitive detector. The PAR lock in amplifiers function as a very narrow band tuned amplifier precisely set to the desired harmonic. A tuned amplifier could be substituted for the 2ω phase detector, although in this case, the negative portions of V_a would be rectified resulting in an always positive signal.

When using the solid state detector (HP 4207), it is necessary to preamplify before splitting off the 1ω and 2ω signals. A PAR Type 113 preamplifier was used. The preamplifier must, of course, be able to handle both the 1ω and 2ω signals simultaneously.

Plots were made by scanning the collimator in the angle α at a very slow rate with a motor, while recording the signal outputs. Figure 10, reference 1 was plotted in the same way. Figure 11 shows one of these plots made with a relatively bright simulated star such that noise was not significant. The scan was carried over a much larger angular range than $\alpha_{max} \leq \alpha \leq \alpha_{max}$, showing the sinusoidal nature of the two signals V_a and V_o. For this plot, the modulator drive was 1000 V rms, which corresponds to $\Gamma_{mo} = 1.00$ and $V_{a(max)}/V_{o(max)} = 0.3$.

The observed value of $V_{a(max)}/V_{o(max)}$ was 0.25, in satisfactory agreement.

To evaluate the noise limitation of the acquisition signal, similar plots were made for lower and lower star intensity until the signals became lost in

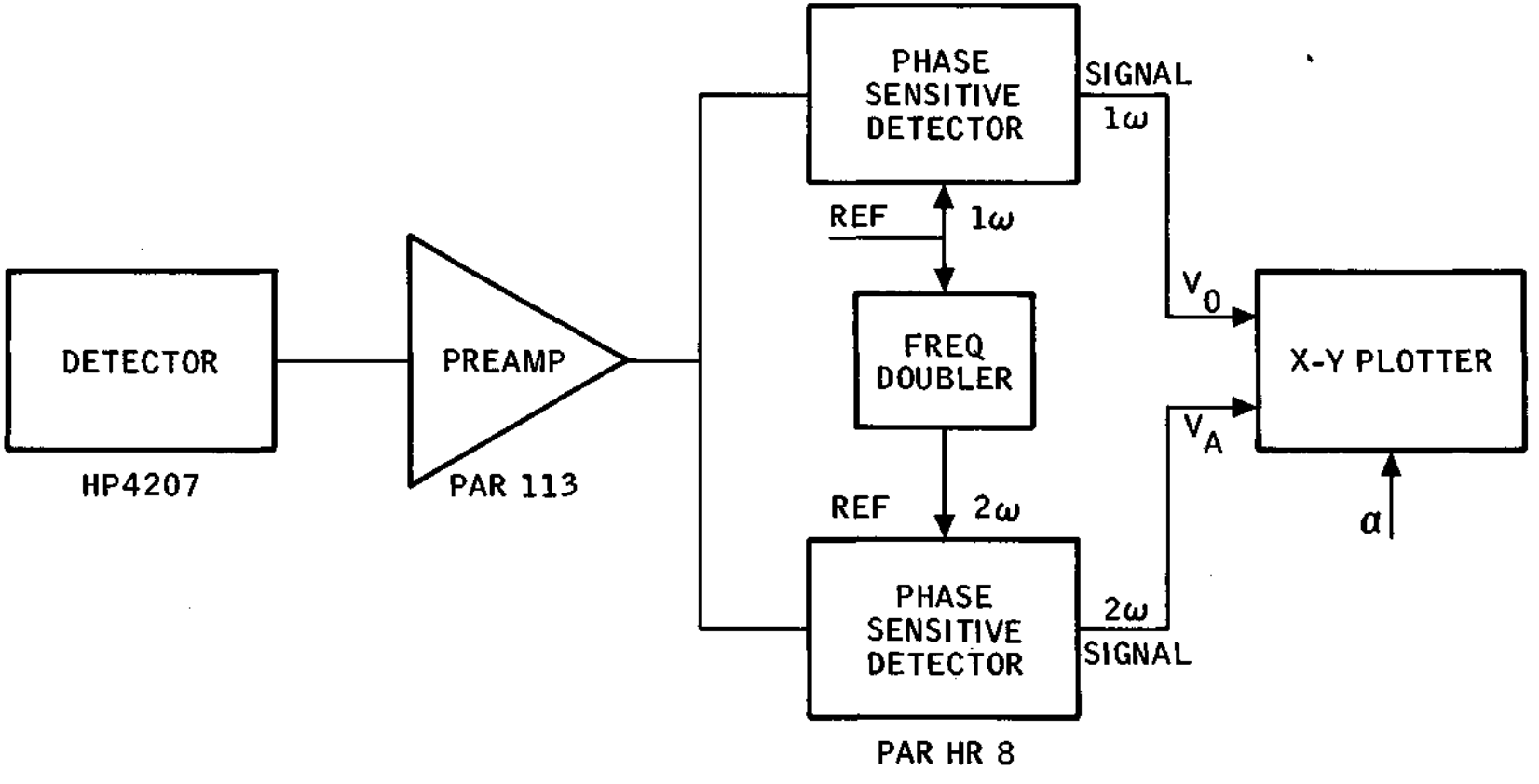

Figure 10. Block Diagram of Electronics used to Evaluate Acquisition Signal

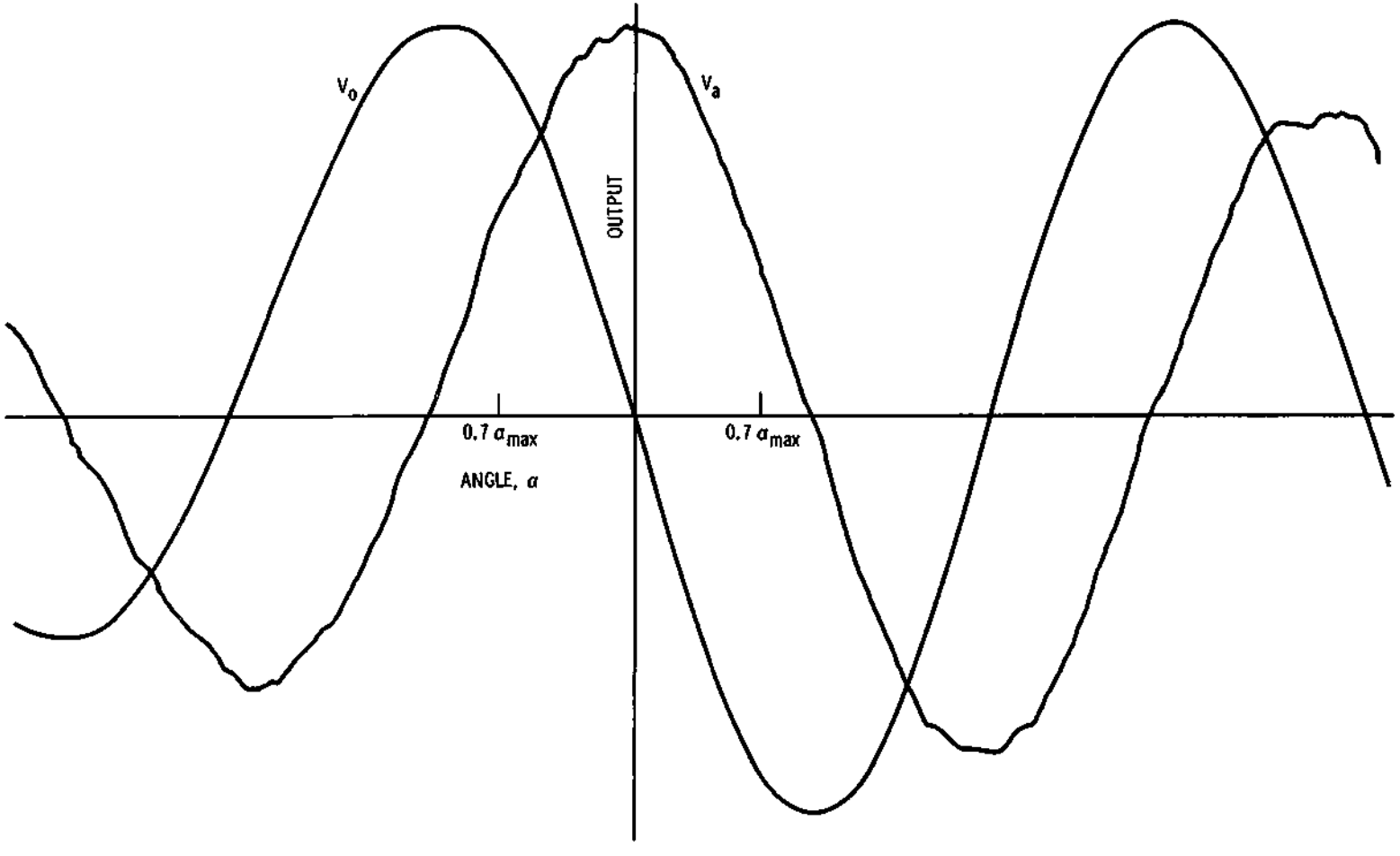

Figure 11. A Tracing of an Acquisition Signal and the Error Signal Itself Made with an X Y Plotter. The Simulated Star was Slowly Scanned in Angle at a Constant Rate in Order to Make the Plot of Signal Voltage as a Function of Angle

noise. An example of one of these plots is given in figure 12. In this plot, the gain in the 2ω channel was 10 times that of the signal channel, rather than 4 times, as in figure 11. As a result, the relative magnitude of the plotted acquisition signal is larger. The time constant for the two channels was the same. The signal to noise level in the acquisition channel is poorer than in the signal channel, as expected, but it is apparent that a useful acquisition signal is available.

A similar plot, was also made with a 9536 B photomultiplier as the detector. The internal gain of the photomultiplier is sufficient to drive the phase sensitive detectors directly, so no common preamplifier was used.

Referring back to figure 11, only the central portion of the plotted angular travel, say $-0.7\,\alpha_{max} \leq \alpha \leq 0.7\,\alpha_{max}$ would be used for control. This range is indicated on the figure. Since the signal outputs are inherently periodic, the field-of-view must be limited optically to $\pm 2\,\alpha_{max}$ to ensure that a control signal can be generated in the proper sense to drive toward null during an acquisition sequence. Suitable logic will ensure that the system does not switch back to a search mode over the $-2\,\alpha_{max} \leq \alpha \leq 2\,\alpha_{max}$ because the acquisition signal goes through zero at $\alpha = \pm\alpha_{max}$. The condition for continuing in track mode should be that either $|V_o|$ or $|V_a|$ be larger than a predetermined threshold.

The present conclusion is that a suitable acquisition signal can be obtained by selectively amplifying the 2ω component of the photosignal, and that the magnitude of the second harmonic component is large enough to ensure a useful signal-to-noise level provided the star is bright enough to track in the control signal channel. The magnitude of the 2ω signal is proportional to I_o at null, and therefore can be used for an intensity gate if desired. Calibration of such an intensity gate would require that the modulator drive be held constant, and would depend on the photodetector responsivity.

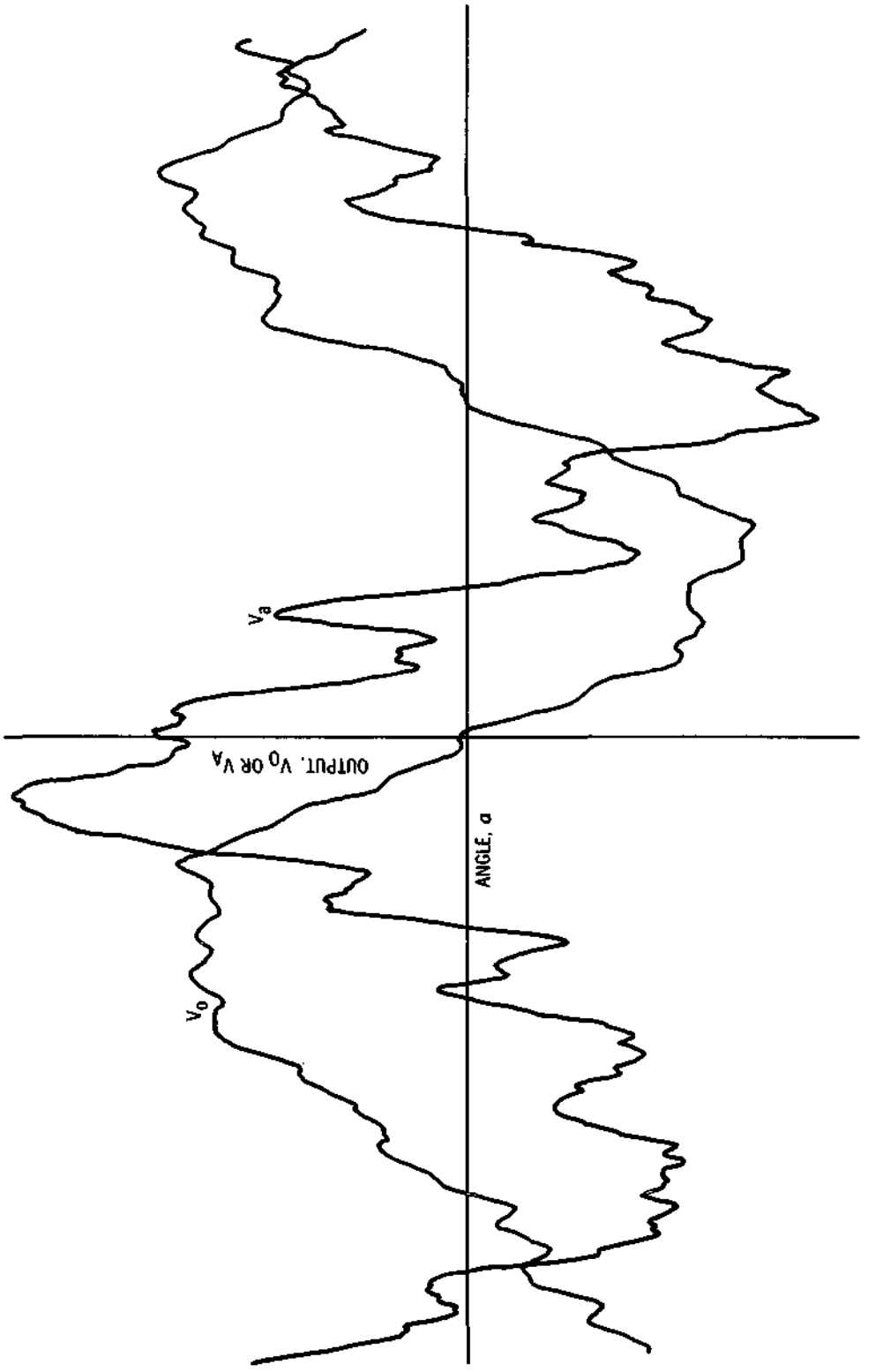

Figure 12. A Tracing Similar to Figure 11, but Made from a Weak Simulated Star so that Considerable Noise is Present

By using appropriate logic circuitry the angular rate for acquisition can be extended to $\pm 2\,\alpha_{max}$ in a very simple manner. To do so, the condition that either $|V_a|$ or $|V_o|$ is larger than a preset threshold level should command a track mode.

V. FIELD OF VIEW CONSTRAINTS

Background and Objectives

Several factors that influence the field-of-view of the EODS are discussed in this section. Results are given in graphical form useful for designing an EODS type sensor for a specific application. Several conclusions are summarized at the end of this section.

There are a number of optical constraints in the EODS field-of-view, all tending to restrict the maximum field-of-view that can be obtained. On the other hand, no optical restrictions are apparent that set a lower limit on field-of-view. We assume that diffraction effects can be neglected, a resonable assumption if the angular field is larger than a few arc seconds.

The factors which would prevent decreasing the field-of-view, thus increasing the pointing precision without limit are systems considerations rather than optical ones. For example, the control loop in which the EODS sensor is an element will require an input over a certain angular range to perform properly. Acquisition dynamics also demand a finite angular range, and the problems of exact pointing of an individual sensor in the cross axis direction require a certain field-of-view in that direction. These factors can be evaluated quantitatively only in terms of a specific application, so the following discussion will be in general terms. The factors to be treated include geometrical constraints associated with collecting light from a large aperture onto a small detector, optical anisotropy of the modulating element, and second-order effects relating to the cross-axis angular field.

The relation between the thickness of the DWP-compensator pair and the angular range α_{max} of the EODS will also be reviewed because it ties in closely with the field-of-view question. The quantity α_{max} is determined by the DWP and compensator only. Its evaluation was discussed in detail in reference 1 and numerical results were given in figure 5 of reference 1 for ADP, calcite and quartz. Note that it was $2\ _{max}$ that was plotted in reference 1. Table II presents numerical values for α_{max} for $\lambda = 0.55$ as a function of DWP thickness for different values of θ, the angle between the DWP optic axis and the sensor axis, and Δn, the natural birefringence of the DWP material.

The angular field-of-view will be defined as the maximum off-axis angle at which the reference source can be seen by the EODS. The angular field would typically be defined by a field stop or the equivalent in the light-collecting optics. The field-of-view in the sensitive direction, α_f, can be different than the field in the cross direction, β_f, and in fact, the two can be chosen independently. The angular range, measured by α_{max}, is independent of both α_f and β_f but, as we have seen in Section III, we would choose $\alpha_f = 2\alpha_{max}$.

Geometrical Constraints

The geometry related to collecting light onto a small detector will be considered first. Basically, attempting to collect light with a large aperture over a large angular field onto a small detector area is a contradictory requirement. This is a well-known trade-off and is not tied specifically to the EODS concept. Numerical results specific to EODS will be presented here.

Figure 13 is a sketch showing the pertinent geometry in which a field stop and field lens is used. This approach eliminates any effect that spatial non-uniformity of the detector area might have on the sensor operation. α_f (or β_f) is the angle between the sensor axis and the edge of the allowable field. The parameters d and b would normally be specified by other considerations; d being the aperture required to collect the desired light flux, and b being the

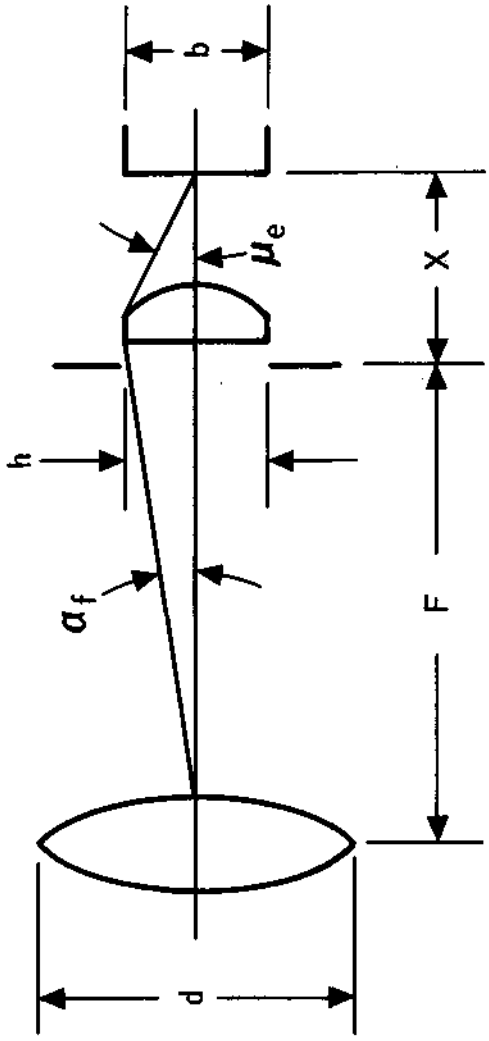

Figure 13. Light Gathering Geometry for Case where a Field Lens is Used.

TABLE II – ANGULAR RANGE α_{max} AS A FUNCTION OF DWP THICKNESS FOR VARIOUS VALUES OF Δn AND θ

$\lambda = 0.55\mu$ is assumed, as is an average wave-plate index of 1.55. α_{max} is given in degrees.

t mm	$\Delta n = 0.01$ $\theta = 45$	$\theta = 80$	$\Delta n = 0.05$ $\theta = 45$	$\theta = 80$	$\Delta n = 0.10$ $\theta = 45$	$\theta = 80$	$\Delta n = 0.20$ $\theta = 45$	$\theta = 80$
0.5	2.36	6.90	0.47	1.37	0.23	0.67	0.118	0.345
1.0	1.18	3.45	0.23	0.67	0.118	0.34	0.059	0.172
1.5	0.78	2.28	0.15	0.43	0.078	0.23	0.039	0.114
2.0	0.59	1.72	0.118	0.34	0.059	0.17	0.029	0.084
5.0	0.23	0.67	0.047	0.14	0.023	0.067	0.011	0.035
10.0	0.118	0.34	0.023	0.067	0.012	0.035	0.0059	0.0172

diameter of the detector sensitive area. In addition, μ_e representing the angular aperture of the field lens, must be within reasonable limits. The quantities shown in the figure are interrelated by simple geometrical considerations, such that the expression

$$\tan \alpha_f = \frac{b \tan \mu_e}{d} \tag{3}$$

may be derived. Note that h, F, and X do not enter, and therefore may be chosen independently.

A number of curves are presented giving numerical values for the important parameters in different combinations. If this detail is not of immediate interest, the graphs may be skipped over, because the results are summarized later. Figure 14 shows α_f and F plotted against b, the detector diameter.

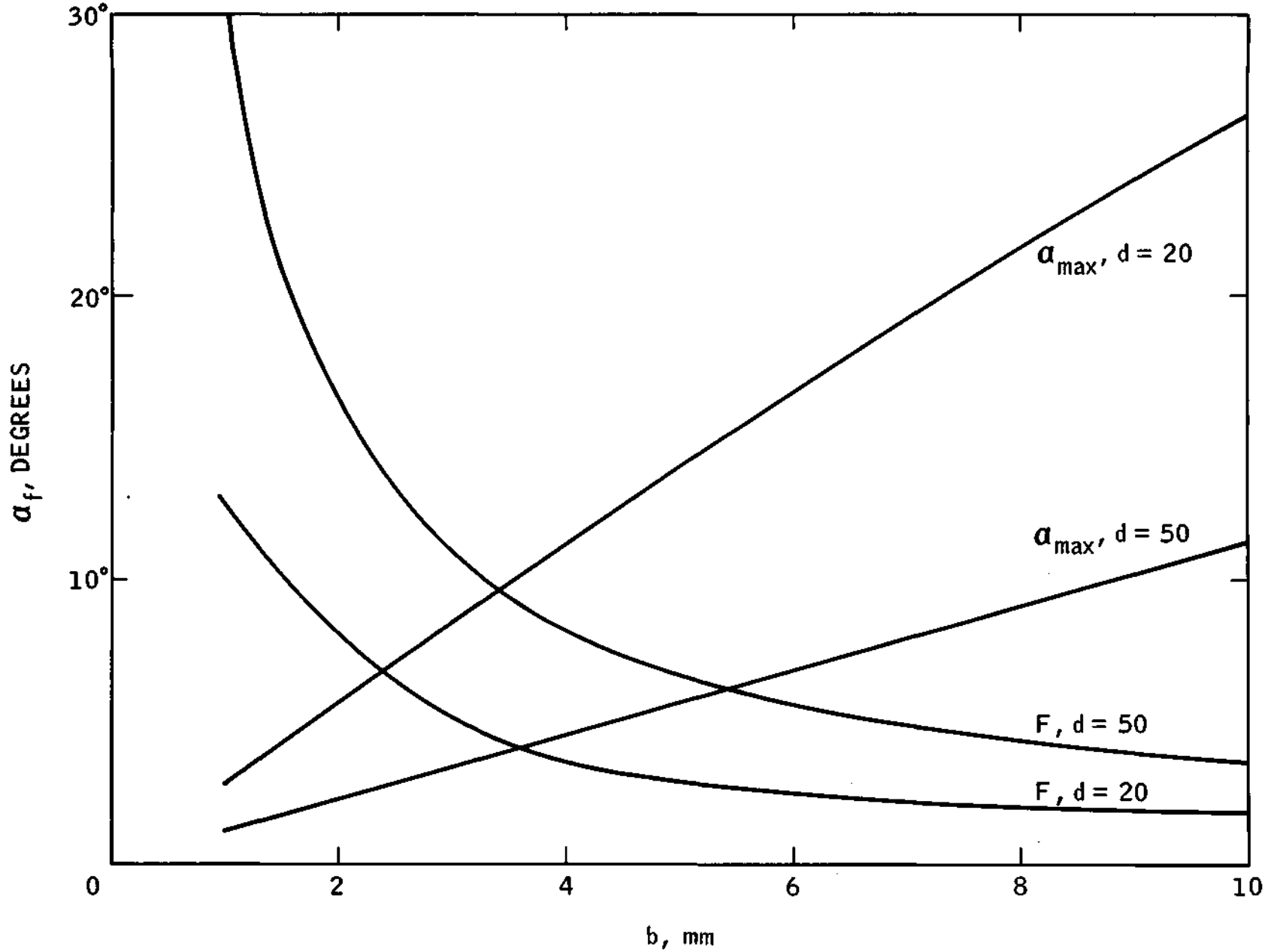

Figure 14. Telescope Focal Length and Field of View α_f Given as a Function of Detector Diameter

Representative numbers were used for the collecting aperture d, the field lens focal length f_f and field lens angular aperture μ_e. The same data are presented in somewhat different form in Figure 15, 16, and 17, by plotting α_f and F versus d, the diameter of the collecting aperture.

Similar results will be obtained if the field lens is eliminated and the detector itself used as the field stop. If this approach is taken, either an appropriately dimensioned rectangular detector or a field stop placed as close as possible to the detector would be necessary to define a specified rectangular field. The geometry is shown in figure 18. Here μ_e refers to the angular aperture of the objective lens as seen by the detector. μ_e thus measures the speed of the objective lens. The expression 5-1 for tan α_f is also obtained for this case.

The curves in figure 14 relating α_f to b and those in Figures 15, 16, and 17 relating α_f to d are therefore valid for either the field lens or objective only configuration. The values for F apply only to the field lens case. For the objective only set up, the objective focal length is given by

$$F = \frac{d}{2 \tan \mu_e} \tag{4}$$

If the diameter of the detector is 1 mm and the objective is 50 mm in diameter, a field lens with $\mu_e = 45^\circ$ (NA = 0.7) and focal length 10 mm would yield a 1.1° half angle field-of-view and an objective focal length of 500 mm. A smaller aperture or a larger detector would increase the accepted field proportionately.

Without a field lens, a 25 mm focal length, f/0.5 lens would be required. A photomultiplier would be a more useful alternative in the objective-only configuration. In this case, d = 1.0 cm, b = 1 cm, and α_f (or β_f) could be 15° with f/2 optics. Note that the field angle α_f will be proportional to tan μ_e, if all

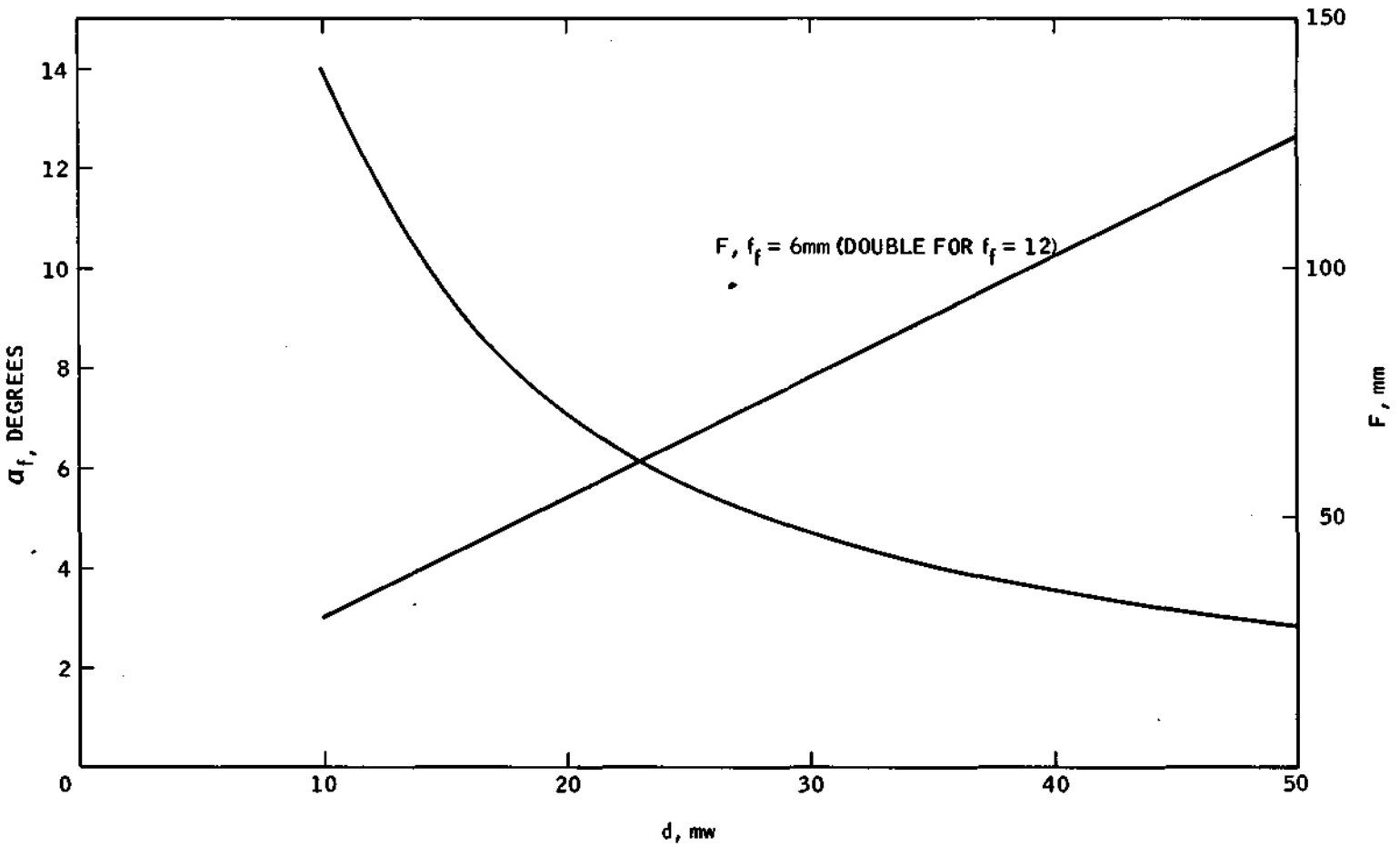

Figure 15. Field of View and Telescope Objective Focal Length Given as a Function of Collecting Aperture

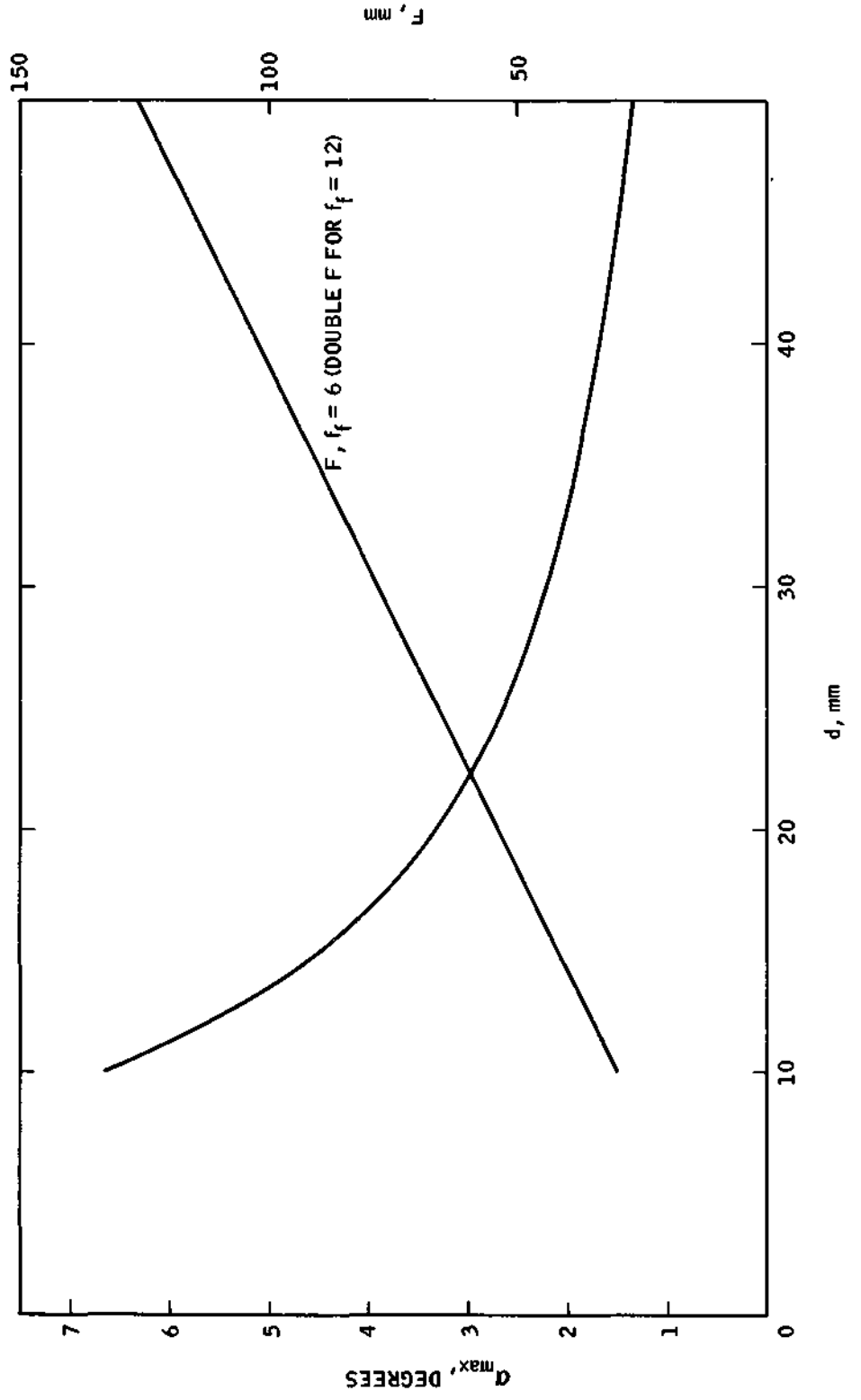

Figure 16. Field of View and Telescope Objective Focal Length Given as a Function of Collecting Aperture

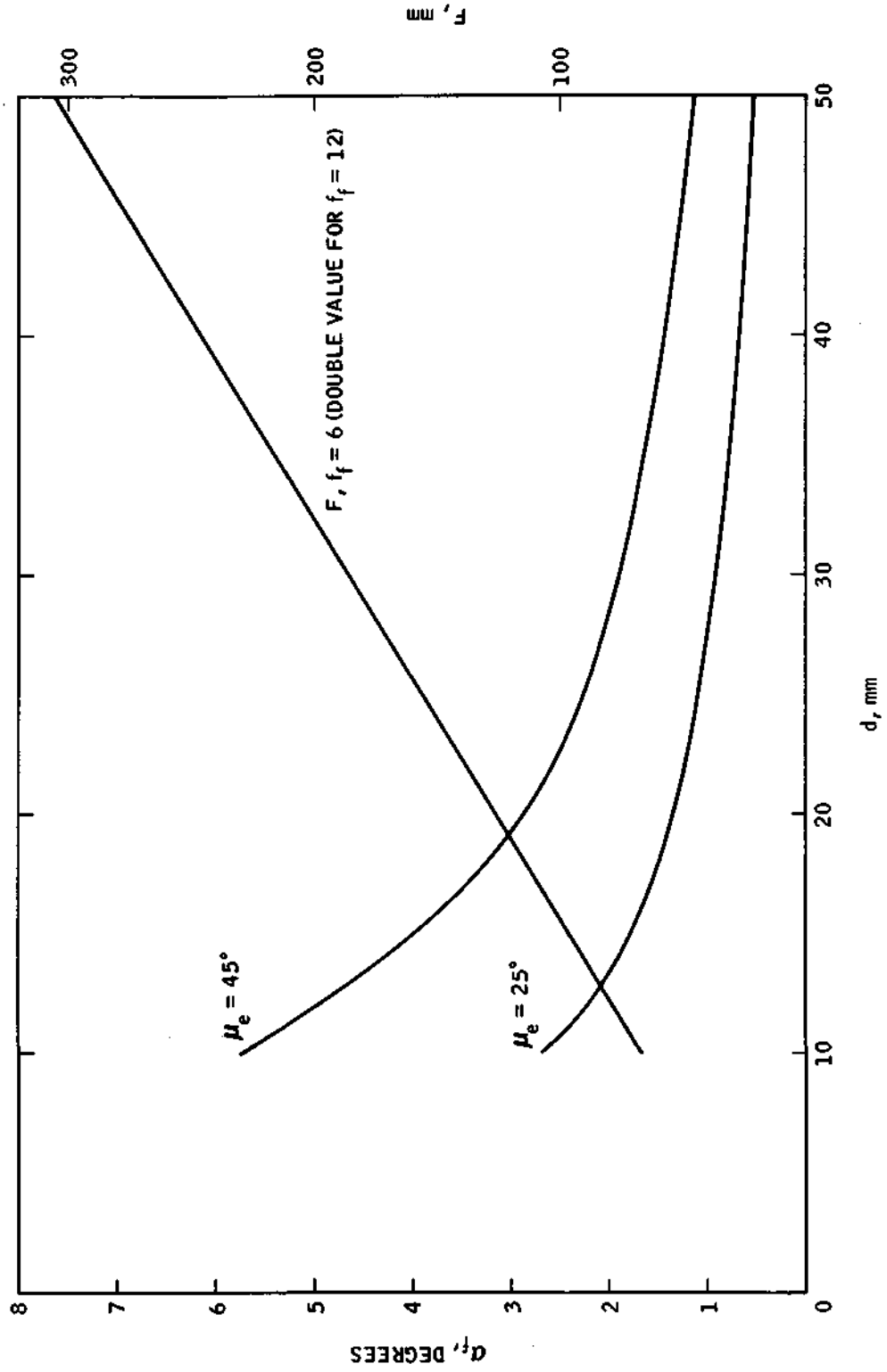

Figure 17. Field of View, α_f Plotted as a Function of Telescope Objective Diameter. Objective Focal Length is also given for Field Lens Case

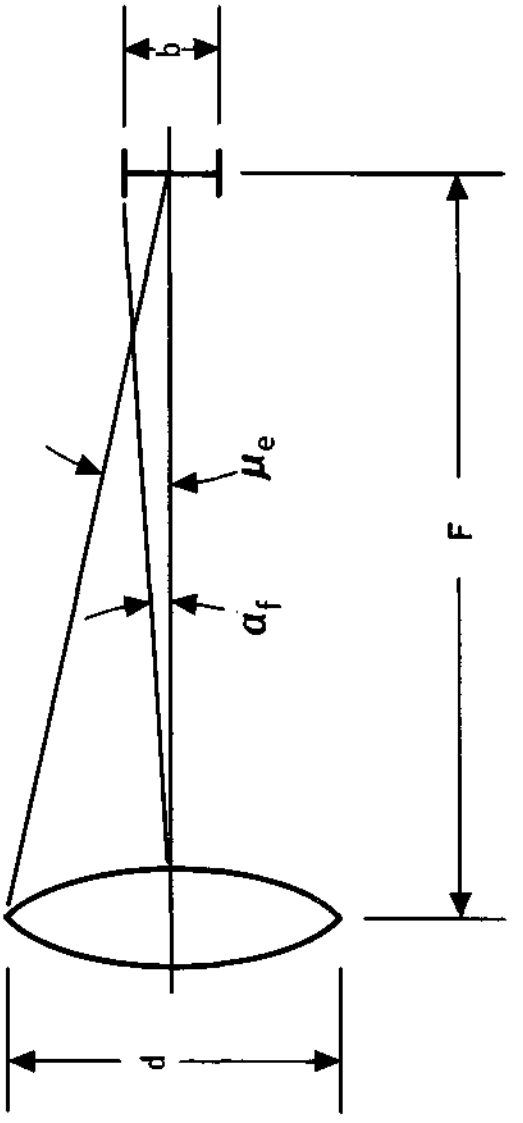

Figure 18. Light Gathering Geometry When No Field Lens is Used

other quantities remain the same. Thus, field-of-view is coupled with the speed of the collecting optics, large field requiring a fast lens.

Modulator Field-of View

A second and independent constraint is introduced by the KDP modulator element. Since the modulator is itself an anisotropic optical element, it introduces a retardation for rays inclined to the sensor axis. As a result, the fringe pattern produced by the DSM as a whole is altered. It is therefore necessary to limit the angular field, α_f, β_f, to values for which the added retardation of the modulator is a small perturbation.

Manufacturers of KDP modulator elements often quote an angular field, one common definition being the angle at which the light leak between crossed polaroids becomes 1 percent. This angle can be computed using the approach of reference 1.

The effective extraordinary index for a wave normal at an angle α from the axis in a crystal is given by

$$n^2 = \frac{n_e^2}{1 + \cos^2 \alpha \frac{\left(n_e^2 - n_o^2\right)}{n_o^2}} \tag{5}$$

from reference 1. The quantities n_e, n_o are the principal indices of the crystal. The transmitted intensity between crossed polaroids, I, is given by

$$I = I_o \sin^2 \frac{\Gamma}{2} \tag{6}$$

where Γ is the retardation and I_o the incident flux. Therefore, if $I/I_o = 0.01$,

Γ must be 0.2. Since the retardation of the DWP is $\pi/2$ when $\alpha = \alpha_{max}$, the added retardation $\Gamma = 0.2$ is small, and represents a reasonable, though arbitrary, choice for the largest allowable perturbation. $\Gamma = 0.2$ would distort the DSM fringe pattern by roughly 10 percent.

The retardation of the modulator plate (no applied voltage) is (ref. 1)

$$\Gamma = \frac{2\pi t}{\lambda \cos \theta} (n(\theta) - n_o) \tag{7}$$

$n(\theta)$ being the effective extraordinary index at the angle θ given by eq. (5). Correcting for the difference in wavefront orientation external to the modulator plate, and using eq. (5), (7) one can compute the angle α_f corresponding to any retardation Γ. The result is

$$\alpha_f = \beta_f = = \frac{\Gamma \lambda n^2}{2\pi t \Delta n} \tag{8}$$

n is an average index $n \approx n_o \approx n_e$. α_f is plotted in figure 19 for KDP as a function of t, the modulator thickness.

The angle α_f or β_f represents a maximum angular field of view. Subject to the constraint that the passive retardation of the modulator be less than 0.2. It can be seen that for $t = 2$ mm and $\Gamma = 0.2$, $\alpha_f = 1.2^\circ$, which is compatible with the 1.1° derived earlier from geometrical considerations.

Considerably larger angles, say, corresponding to a 10 percent leak, could be used at the cost of some distortion in the output signal transfer function and some cross coupling. Both effects are constant and predictable. There is a small curvature of the fringes produced by the DSM, which is reflected as a cross-coupling over an extended angle β normal to the sensitive direction. Correction of this curvature has been observed empirically from a propitious combination of the angular retardation functions of the DWP and modulator.

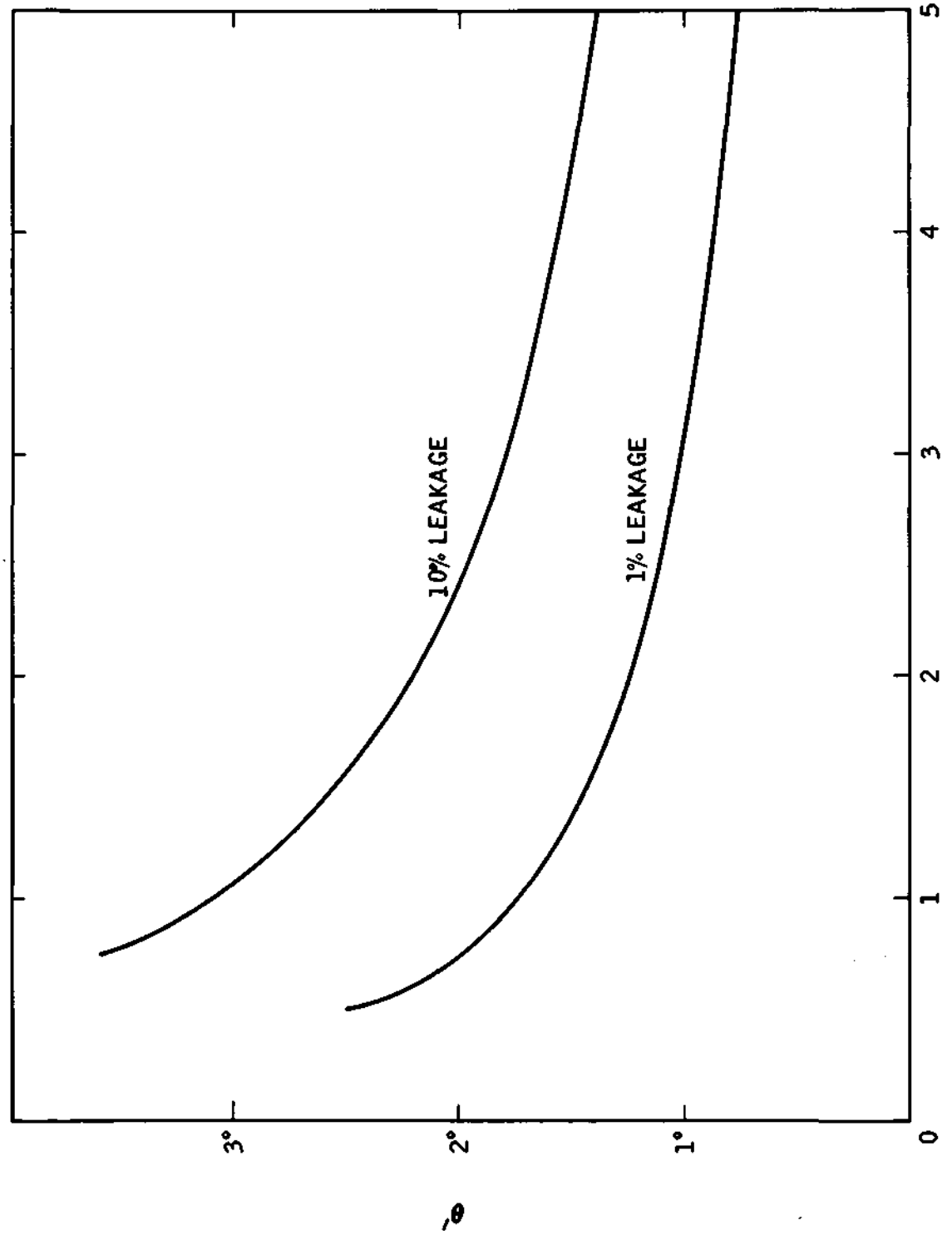

Figure 19. Field of View of KDP Modulator Plate as a Function of Plate Thickness

The small retardation of the modulator, increasing quadratically with β, can combine subtractively with the second order retardation of the DWP along the null axis ($\alpha = 0$). By proper choice of materials and dimensions of all elements of the DSM, we feel it is possible to operate with negligible cross-coupling over a considerably larger angle than the $\beta \approx 1^{\circ}$ calculated above. However, no detailed work has been done on this point. Though straightfoward, calculation of the retardation function over a two-dimensioned range of α and β would have to be done numerically by computer because of algebraic complexity.

Summary

In summary, for a solid-state detector configuration, a field-of-view (center to edge) of a little more than 1° or any smaller value can be easily designed for. This limitation applies both the the sensitive direction and perpendicular to it, but the actual field angles can be chosen independently; for example, $\alpha_f = 0.1^{\circ}$, $\beta_f = 1.0^{\circ}$, or $\alpha_f = 1.0^{\circ}$, $\beta_f = 0.1^{\circ}$.

If it is necessary to reach a larger angular field, some increase could be obtained with the same general configuration. For example, if the modulator were made 1 mm thick, a difficult but not impossible fabrication problem, and if distortion of the DSM fringe pattern is allowable so that $\Gamma = 0.4$ (10 percent leak) defines the field limitation, a field half-angle of 3.1° could be reached. A very fast field lens (N. A. 0.7 or better) and a 2.5 mm diameter detector would be necessary.

To reach a field of view of greater than 3°, a different approach would be taken. Use of a photomultiplier removes the geometrical light-gathering constraint discussed above because of its large area and the fact that smaller collecting aperture will do the same job. If the modulator is then eliminated by incorporating the piezoelectrically driven, mechanically tuned ADP directional wave plate, an approach that is described in Section VII below, then the modulator field-of-view is completely eliminated as a constraint. Since the minimum reasonable DWP thickness is ~ 1 mm for ADP, an $\alpha_{max} \leq 0.6^{\circ}$ is obtained (ref. 1). Thus, α_f in the sensitive direction would be 1.2°. Therefore, a field α_f 1.2° by $\beta_f = 10^{\circ}$ (an arbitrarily chosen number) could be reached. If a DWP modulator could be made of quartz, mechanically tuned and driven in the same

manner as the ADP, then $\alpha_{max} = 5^{o}$; $\alpha_f = 10^{o}$ becomes possible, together with $\beta_f = 10^{o}$ as mentioned previously. Alternatively, the stressed-plate modulators described in Section VII are themselves isotropic and therefore have no defined field-of-view limitation. The use of this type of modulator and quartz DWP and compensator would permit $10^{o} \times 10^{o}$ fields to be accommodated.

VI. STRAY LIGHT

Background and Objectives

The effect of stray light on the sensor response is discussed in this section. Two cases are treated; light scattered onto the EODS detector from outside of its geometrically defined field-of-view, and light from sources other than the reference star within the field-of-view.

The investigation of effects from scattered light was a purely empirical study done in the laboratory using the breadboard sensor. The results are qualitative in nature, and should be taken as an order of magnitude indication of the stray light illumination level at the entrance aperture that is tolerable. They form a basis for defining the effectiveness of the baffling that a prototype sensor would require. Evaluation of the effect of a spurious source within the field-of-view is straightforward and was done analytically.

Results

The EODS laboratory breadboard was set up such that the polarizer was in the plane of the entrance aperture. A white light projector illuminated the entrance aperture from the side at an angle γ as shown in figure 20. The illumination fell directly onto the polaroid material of the polarizing element of the DSM. The angle γ was variable, from 30^{o} to 80^{o}. The illuminance on a white surface at right angles to the direction of illumination located at the EODS entrance aperture was measured with a photometer. Light was not permitted to enter the EODS other than through the entrance aperture. The sensor was operated on a simulated star of intensity such that a typical signal-to-noise ratio was obtained (~ 30).

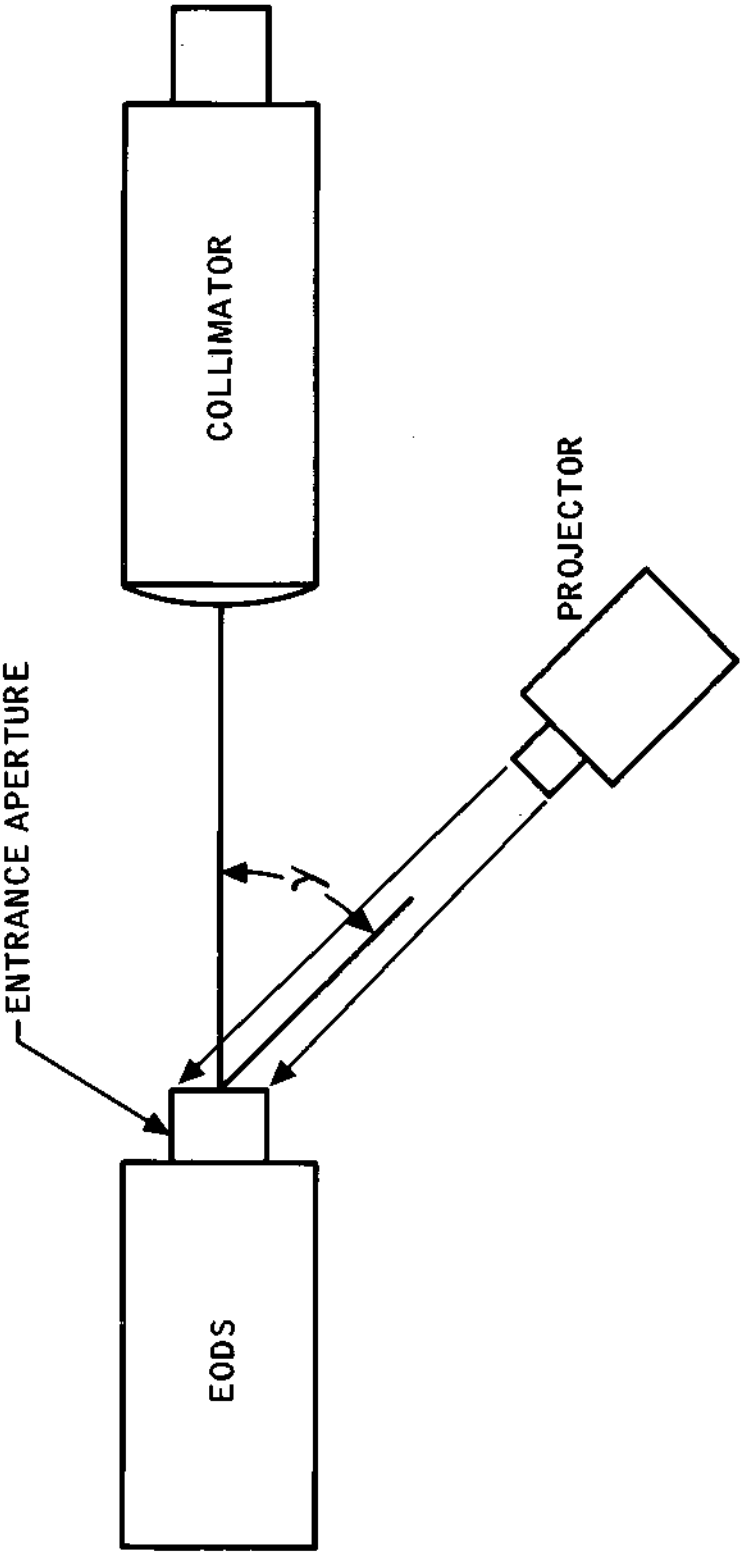

Figure 20. Laboratory Set-up Used for Study of Stray Light Effects

The resulting change in the noise level and null position of the sensor were then observed as a function of illumination level and direction. The detailed data are not presented because the results would be expected to be sensitive to the exact mechanical configuration of the sensor parts and also its surroundings in the laboratory. The observed effect on the sensor output results from very small amounts of light scattered to the detector by the optical elements or by the surrounding parts.

The EODS was set up in both the HP4207 solid-state detector and the EMI 9536B photomultiplier configurations. Not surprisingly, the results differed. The closer the stray light direction approached the axis, the larger its effect. The primary perturbation using the HP 4207 detector was a null-shift, while for the EMI 9536B, it was an increase in noise level. Representative numbers are given in Table III for illumination of the entrance aperture from 45° to the axis.

The effect of a secondary source within the geometrical field can be calculated by superimposing the outputs for the reference source and the spurious one. If the secondary source is a star, it is convenient to express the two signals in a normalized form: For a point source of arbitrary intensity I_S;

$$V_S = \frac{I_S V_{ref}}{I_{ref}} \sin \frac{\pi}{2}\left(\frac{\alpha}{\alpha_{max}}\right) \tag{9}$$

where

V_S is the sensor output;

I_{ref} is the intensity of the reference object; that is, the star being tracked;

V_{ref} is the maximum, hard-over sensor output if observing the reference object only.

To evaluate the angular null shift resulting from the presence of a secondary star of intensity I_o, let this angle be $\delta\alpha$. The quantity $\delta\alpha$ was evaluated by equating the EODS output for the secondary source to the output resulting from the reference at the angle $\delta\alpha$. The result is

$$\frac{\delta\alpha}{\alpha_{max}} = \frac{2}{\pi} \frac{I_S}{I_{ref}} \sin \frac{\pi}{2} \left(\frac{\alpha_S - \delta\alpha}{\alpha_{max}} \right) \tag{10}$$

α_S represents the position of the secondary source measured from the reference star position. Its coordinate in the cross axis or β direction is irrelevant.

The error angle $\delta\alpha$ from eq. (10) is plotted in figure 21 as a function of I_S/I_{ref} and α_S.

A second case is likely to be encountered, that of a diffuse but nonuniform source, such as the Milky Way. The continuous source can be described by an intensity $I(\alpha, \beta)$ depending on the direction, specified by angles α and β. The output from the distribution I is an expression similar to eq. (9).

$$V_S = \iint_{field} I(\alpha, \beta)\, V_0 \sin \frac{\pi}{2} \frac{\alpha}{\alpha_{max}}\, d\alpha\, d\beta \tag{11}$$

Following a procedure analogous to the one used to arrive at eq. (10), and after some manipulation, one obtains

$$\Delta \alpha_S = \frac{4\, \alpha_{max}\, \beta_f}{\pi\, \Delta^2\, I_{ref}} \int_{-2}^{2} \int_{-1}^{1} I(x, y) \sin \frac{\pi}{2} x\, dx\, dy \tag{12}$$

x, y are dimensionless integration variables replacing α and β, respectively. They are scaled such that $x = 1$ when $\alpha = \alpha_{max}$ and $y = 1$ at β_f. The field of view is assumed to be rectangular, $\alpha_f = 2\alpha_{max}$ by β_f. The distributed intensity I is to be interpreted as the intensity per unit solid angle and Δ represents

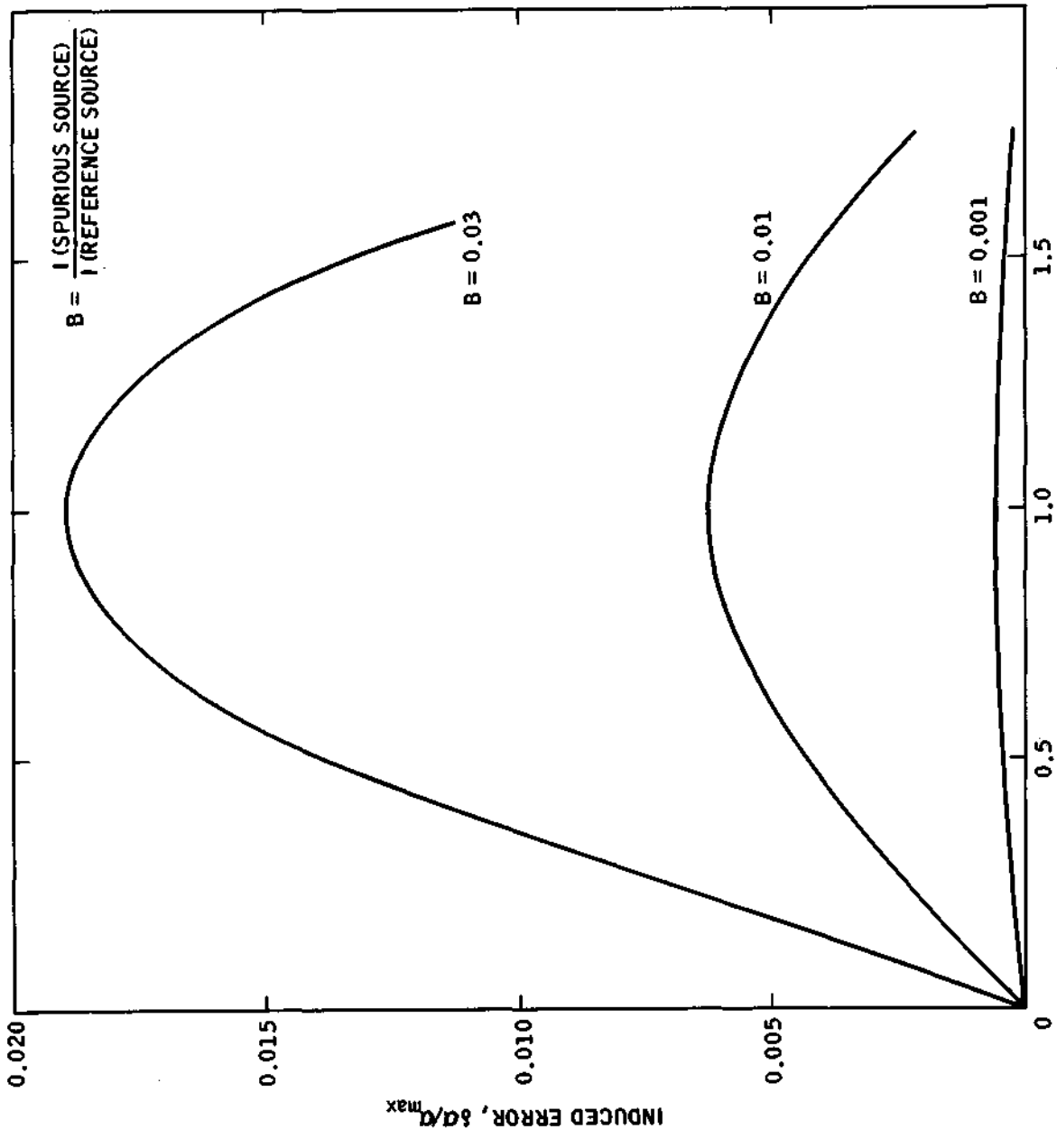

Figure 21. Induced Bias as a Function of Position and Intensity of Spurious Source within the Sensor Field-of-View

the unit selected. For example, I(x, y) could be given in terms of lumens/cm^2 at the entrance aperture received from one square degree of sky in direction x, y. In this case, Δ would be 1° or 0.01745 rad. I_{ref} is the illumination by the reference star and its units are to be compatible with I.

In agreement with one's intuition, the expression 6-4 shows that the influence of a given distribution of light should be proportional to the total geometrical field-of-view accepted by the sensor, $2\,\alpha_{max}\,\beta_f$. The magnitude of the integral is not as easily visualized, but would be largest when the diffuse luminance is confined to one side of the reference, around the angle where the sensor output is large, at $\alpha = \alpha_{max}$. In this situation, the offset of the null would be comparable in magnitude but never worse than the effect of a star located at $\alpha_S \approx \alpha_{max}$, and having intensity equal to the integrated intensity of the diffuse source over the sensor field-of-view.

TABLE III.– THE EFFECT OF OUT-OF-FIELD SCATTERED LIGHT EODS LABORATORY BREADBOARD

Detector	Illumination at 45° in terms of Reference Star	Null Shift	Noise Increase Factor
9536B	6×10^5	0	2.0
4207	0.9×10^8	$0.1\,\alpha_{max}$	1.9

VII. TUNED MODULATOR DEVELOPMENT

Background and Objectives

The primary objective of this portion of the work was to demonstrate a technique for increasing the efficiency of the EODS light modulator by mechanically resonating the modulating element at the drive frequency. Without such techniques, the best modulator available is the longitudinal KDP (potassium dihydrogen phosphate) type, using the deuterated form, usually designated KD*P. KD*P is clear, and can be fabricated into a thin, large aperture modulator plate.

The half-wave voltage of KD*P is 3.2 kV. In terms of the EODS application, a sinuosoidal drive of approximately 1000 V RMS is required for the KD*P plate. This voltage requirement is a constant, independent of the modulator dimensions. Modulators with much lower half-wave voltage can be made from other materials (e.g., $LiTaO_3$ and several niobates), but these materials do not lend themselves to incorporation into a thin plate modulator of 1 cm or larger aperture.

There were two motivations for our investigation of mechanical tuning: lowering the drive voltage requirement, and eliminating the off-axis static birefringence of the modulator.

Although the 1000 V rms sinuosoidal drive is not difficult to obtain, one would prefer to work at lower voltages. In general, excitation of an appropriate vibrational mode will have the potential of increasing the optical response by a factor on the order of the mechanical Q of the resonance. Additionally, the use of mechanical tuning permits entirely different approaches to be made to the modulation function. These eliminate the modulator crystal and with it, the perturbation to the action of the DWP caused by its own static birefringence. Several references in the literature examine the question of resonant effects in an electro-optic or birefringence modulator and should be consulted for background. Both resonance in electro-optic crystals (ref. 3) and pure stress-optic effects (ref. 4) are discussed.

Several approaches were initially considered, including: (1) Resonating a KD*P modulator by adjustment of drive frequency to the proper value; (2) The use of high-Q quartz crystal elements as modulators; (3) External piezo-electric drive of a passive optical element; (4) Combination of DWP and modulator functions into one resonated optical element.

Approaches (3) and (4) were the most likely to yield favorable results, and experimental investigations of these two ideas were conducted. These experiments are discussed separately below.

Piezo-Electrically Driven Stressed-Plate Modulators

Principle of operation. — When a light source is observed through a pair of crossed polarizers with a normally isotropic transparent material inserted between the polarizers, the extinction will be destroyed if the isotropic material becomes strained. If the strain is time-dependent, then the material exhibits time-varying birefringence and modulates the intensity of the transmitted light at the frequency of the induced strain, just as an electro-optic modulator would. A stressed-plate modulator can utilize this birefringence effect by mechanically stressing an optically isotropic modulator element in response to an applied excitation voltage. The transformation of an applied voltage to a proportional mechanical stress is accomplished by piezo-electric transducers of lead zirconate-lead titanate (PZT) ceramic. The entire modulator structure is driven in a fundamental extensional resonance mode, thereby minimizing the required driving voltage. The optical retardation of the plate is proportional to the stress, a response called the stress-optic or piezo-optic effect.

In the stressed-plate modulator, the active element can be any transparent material; glass and several types of epoxy casting resins were chosen. The retardation of a plate will depend upon the stress-optic constants of the material selected, the thickness of the element, and the applied stress along the selected axis. The stress is of extensional form (compressional or tensional) along that axis, not shear. The desired vibrational mode is the fundamental extensional mode of the entire structure along its length (X direction in fig. 22).

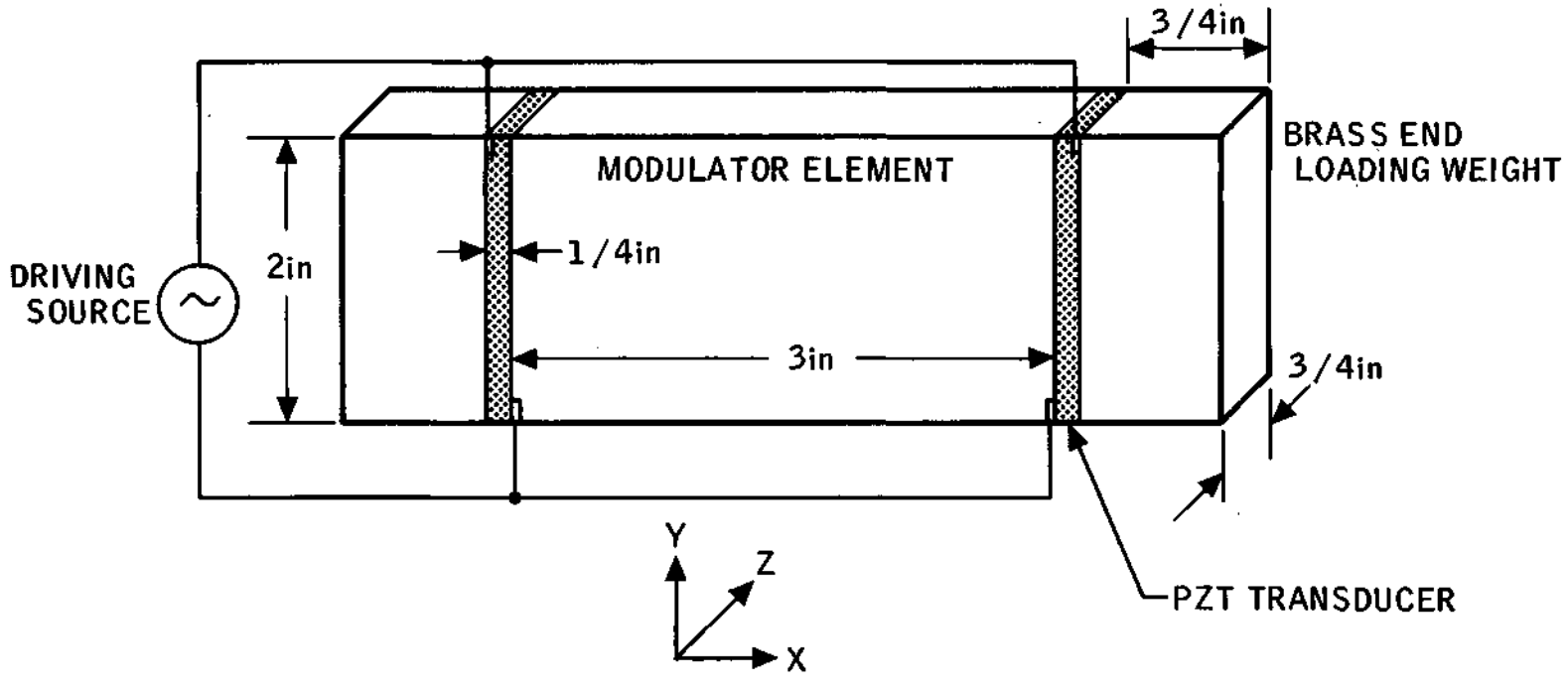

Figure 22. Piezoelectric Stressed-Plate Modulator

The particle motions are all in the X direction, with a maximum velocity at the ends of the bar and with a node at its center. The corresponding stress pattern depends only on X, being constant in the Y and Z directions. The magnitude of the strain exhibits a broad maximum around the center of the bar. In a uniform bar, the strain amplitude would be a half cycle of a sinuosoid, but it is broadened by the presence of the end loading.

The overall efficiency of the stressed-plate modulator will also depend upon achieving good electromechanical coupling between the PZT driving wafers and the vibrational mode they excite. Further increases in efficiency will result from increases in the mechanical "Q" of the modulator assembly. Care was taken to minimize the mechanical losses of the experimental stressed plate modulator, and to obtain effective coupling to the transducers. Time did not permit a detailed and quantitative acoustical design; but the present results are representative. Further optimization should be possible, but a large increase in overall performance is not likely.

Construction details.— The configuration of the piezo-electrically-driven stressed-plate modulator is shown in figure 22. The ends of the stressed plate are loaded by means of the PZT transducers and brass weights. Electrical excitation is applied to the PZT transducers in parallel. The PZT transducers operate in a thickness expansion mode and provide an induced strain along the length of the stressed plate modulator element. The brass end-weights provide a means of modifying the coupling between PZT element and the desired mode of the complete modulator structure. Adjustment of the coupling was accomplished by modifying the end-weights. Little effect was observed in response to this variation.

The piezo-electric transducer material used was PZT-4 ceramic, operating in a thickness expansion mode in response to an excitation field directed normal to the surfaces of the wafer. The piezo-electric constant in this mode is -246×10^{-12} meter/volt, a value which is large compared to that of other piezo-electric materials. This particular PZT ceramic is frequently used in high-power acoustical transducer applications because of its high resistance to depolarization and its low dielectric and mechanical losses.

Assembly of the modulator structure was accomplished by cementing the brass end-weights, PZT-4 transducers, and modulator element together with EPON 828 bonding agent. Type D curing agent was used in a volume proportion of 10 percent. The completed structure was mechanically rugged and no difficulties were experienced with any of the bonded surfaces during evaluation. A photograph of two stressed plate modulators is shown in figure 23. The smaller one was incorporated into the lab breadboard EODS sensor for demonstration.

Experimental configuration.— The stressed-plate modulator was electrically driven over a range of frequencies of from 5 Hz to 500 kHz at a level of 10 volts peak-to-peak. Once the fundamental mode resonance had been located, a constant drive of 80 volts peak-to-peak was maintained throughout the tests. The drive voltage was applied in parallel to the two piezo-electric transducers.

The modulator was supported by two rubber isolators placed centrally along the length of the modulator assembly, near the central node of the vibration pattern. Constraining the modulator element in this fashion permitted the ends to move freely and did not interfere with the natural resonances of the driven structure. A collimated light beam having a diameter of approximately 0.2 cm was bandpass filtered at 5461 Å and passed through a polarizing element before falling at normal incidence upon the stressed-plate modulator. The collimated light beam was subsequently passed through a Babinet compensator, a quarter-wave plate, and finally an analyzer. Detection of the transmitted light flux was accomplished by means of a photomultiplier operating at approximately 800 volts. Figure 24 shows the optical configuration used for the stressed-plate modulator tests. The axes of the polarizer were located at 45° to the long (X) axis of the modulator.

The pretest setup and adjustment consisted of initially obtaining the best extinction between crossed polarizers by means of compensator adjustments, thus optically compensating for residual strains within the stressed-plate modulator element. The quarter-wave plate was then inserted to shift the modulator operating point to the point of maximum slope of its light transfer curve, and electrical excitation was applied to the piezo-electric transducers. The resulting modulation of the light beam was detected by the photomultiplier

Figure 23. A Photographic View of Two Plastic Stressed Plate Modulators

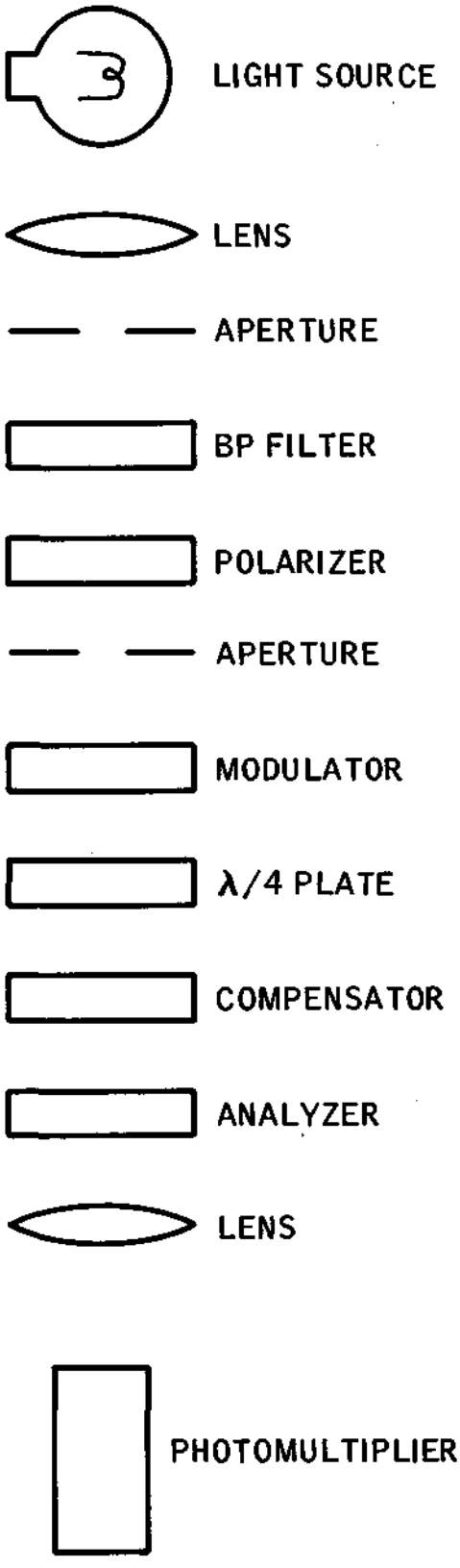

Figure 24. Optical Test Configuration

and displayed by an oscilloscope. Measurements of modulation amplitude were made from the displayed oscilloscope traces.

Experimental results.

1. Glass stressed-plate modulator

A glass stressed-plate modulator was fabricated with the dimensions shown in figure 22 and a measured thickness of 0.381 inches. Initial tests were made to locate the mechanical resonant frequencies over a frequency range extending up to 500 kHz. Mechanical resonances were identified by driving one end of the modulator structure and observing the energy coupled to the other end by means of the piezoelectric transducers. A constant drive voltage of 10 volts peak-to-peak was used during the resonant sweep.

The results of the resonance sweep are shown in figure 25. The frequency and amplitude of each resonant peak are plotted. The fundamental mode resonance was identified at 38.1 kHz. Figures 26, 27, and 28 show the optical modulation depth as a function of position along the length of the modulator plate obtained in the fundamental vibrational mode for three different end-drive conditions. Figure 26 is connected for additive drive contributions from the two transducers. Figure 27 is for subtractive drive, that is, with the polarity of one transducer reversed with respect to the other. The fact that effective modulation is obtained in this connection indicates a large acoustic asymmetry or unbalance in the modulator structure. Figure 28 is the corresponding curve for drive applied to one transducer only. Modulation depth of approximately 20 percent is indicated in the center region of the stressed-plate, with both transducers adding.

The mechanical Q of the fundamental mode was measured to be approximately 126. This value of mechanical Q was the highest exhibited by any of the other structures tested and represents an efficient modulator structure in view of its modulation efficiency of

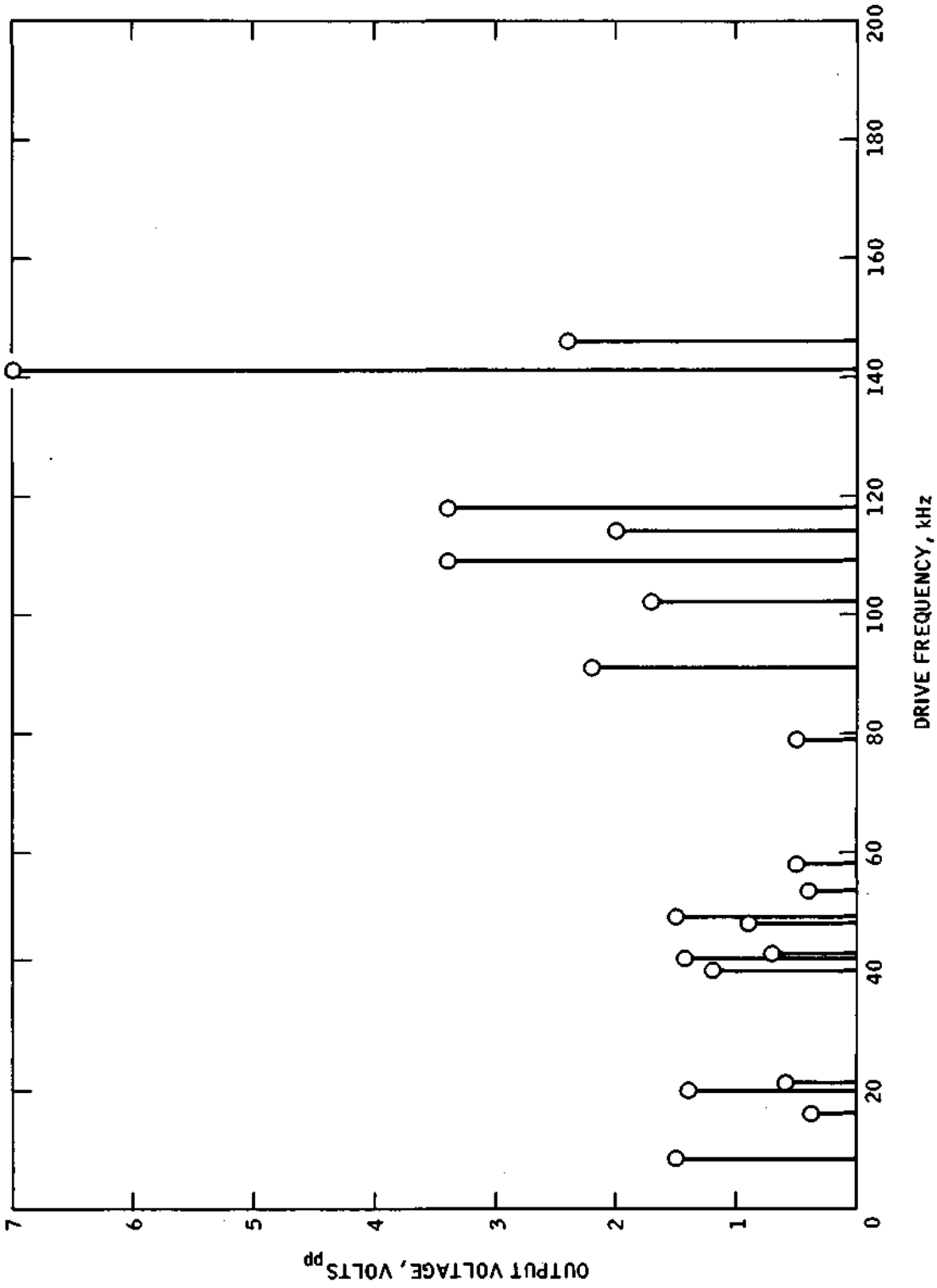

Figure 25. Glass Stressed Plate

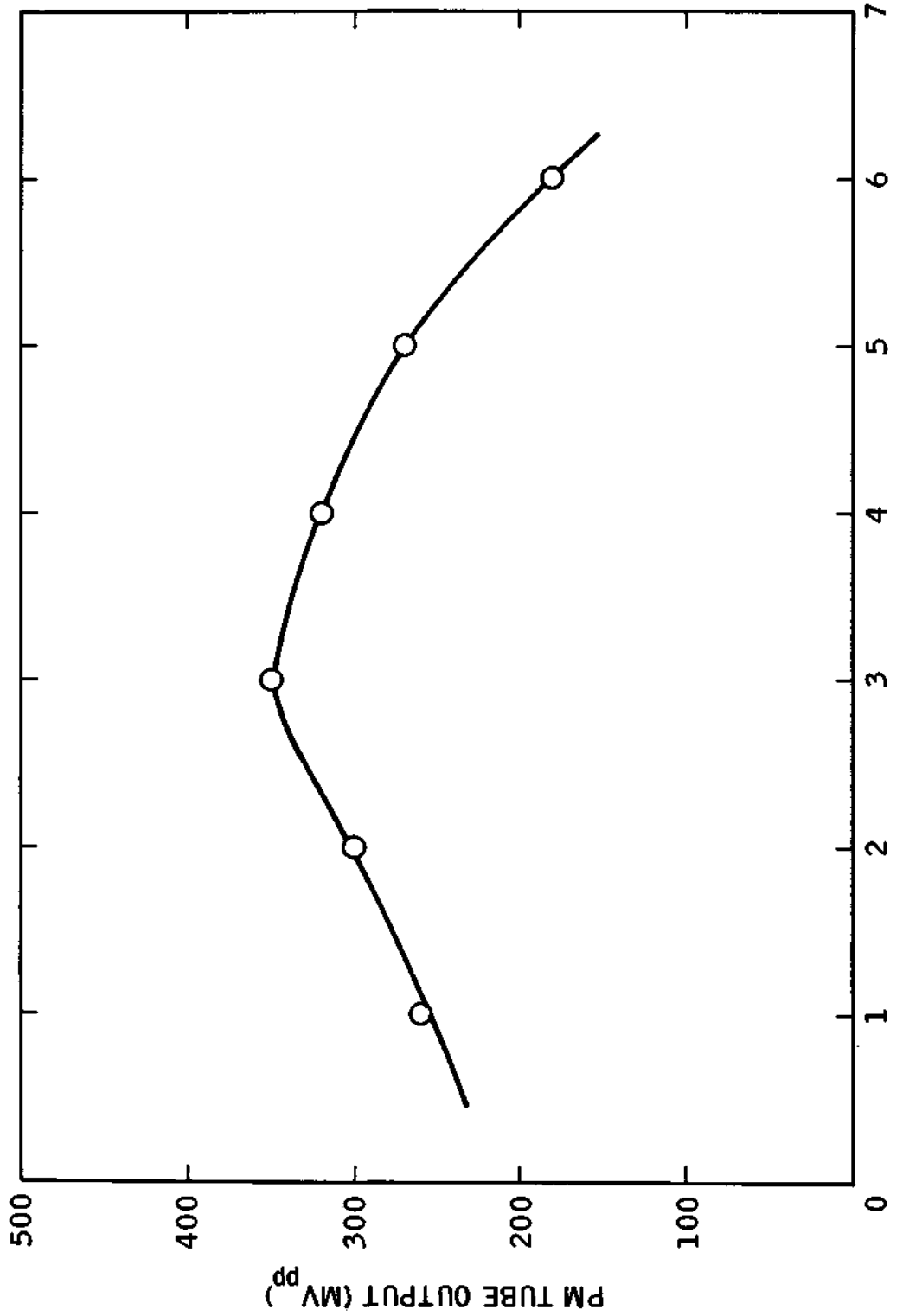

Figure 26. Optical Modulation Depth as a Function of Position, Glass Modulation Transducers Additive

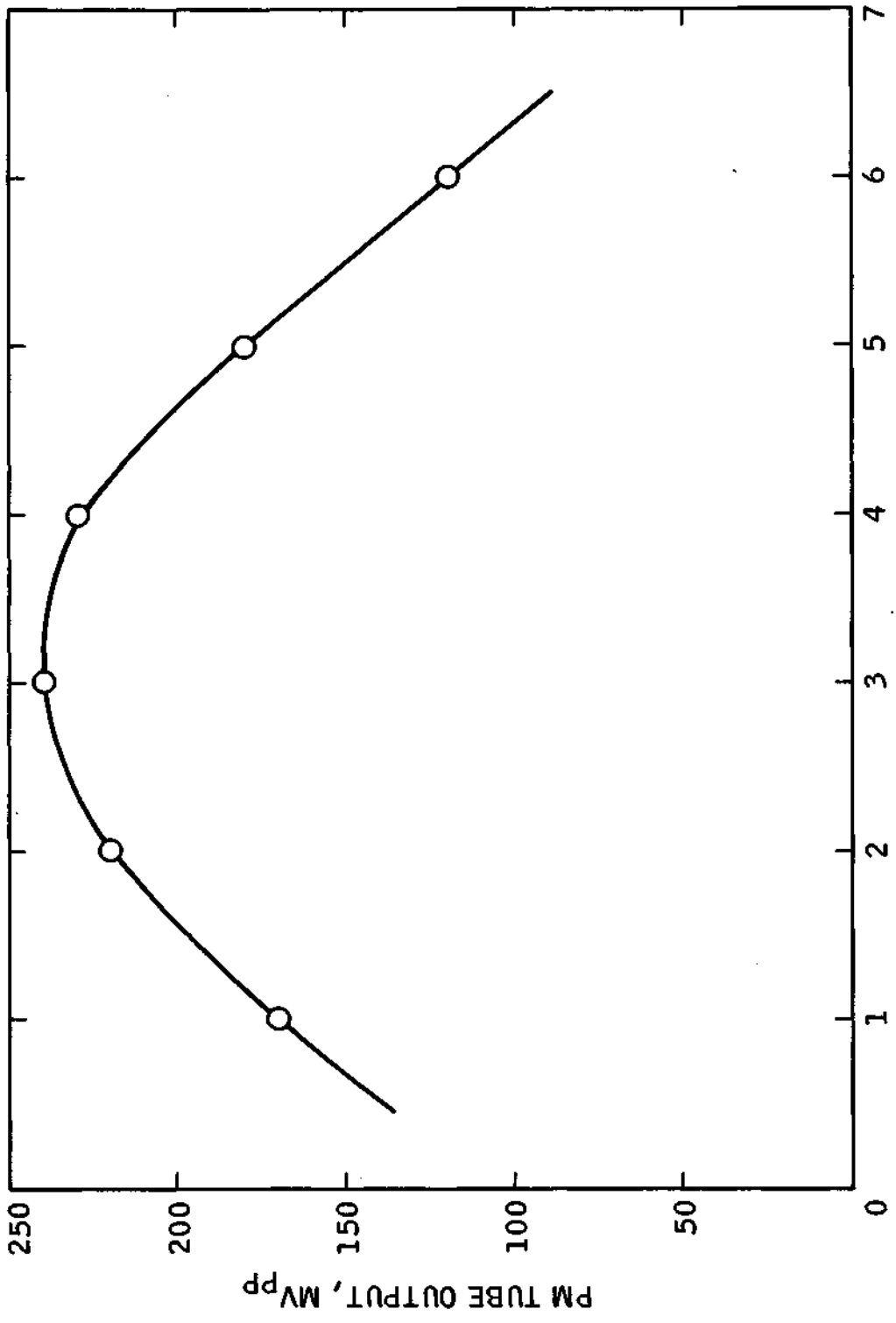

Figure 27. Optical Modulation Depth versus Position, Glass Modulator Transducers Opposing

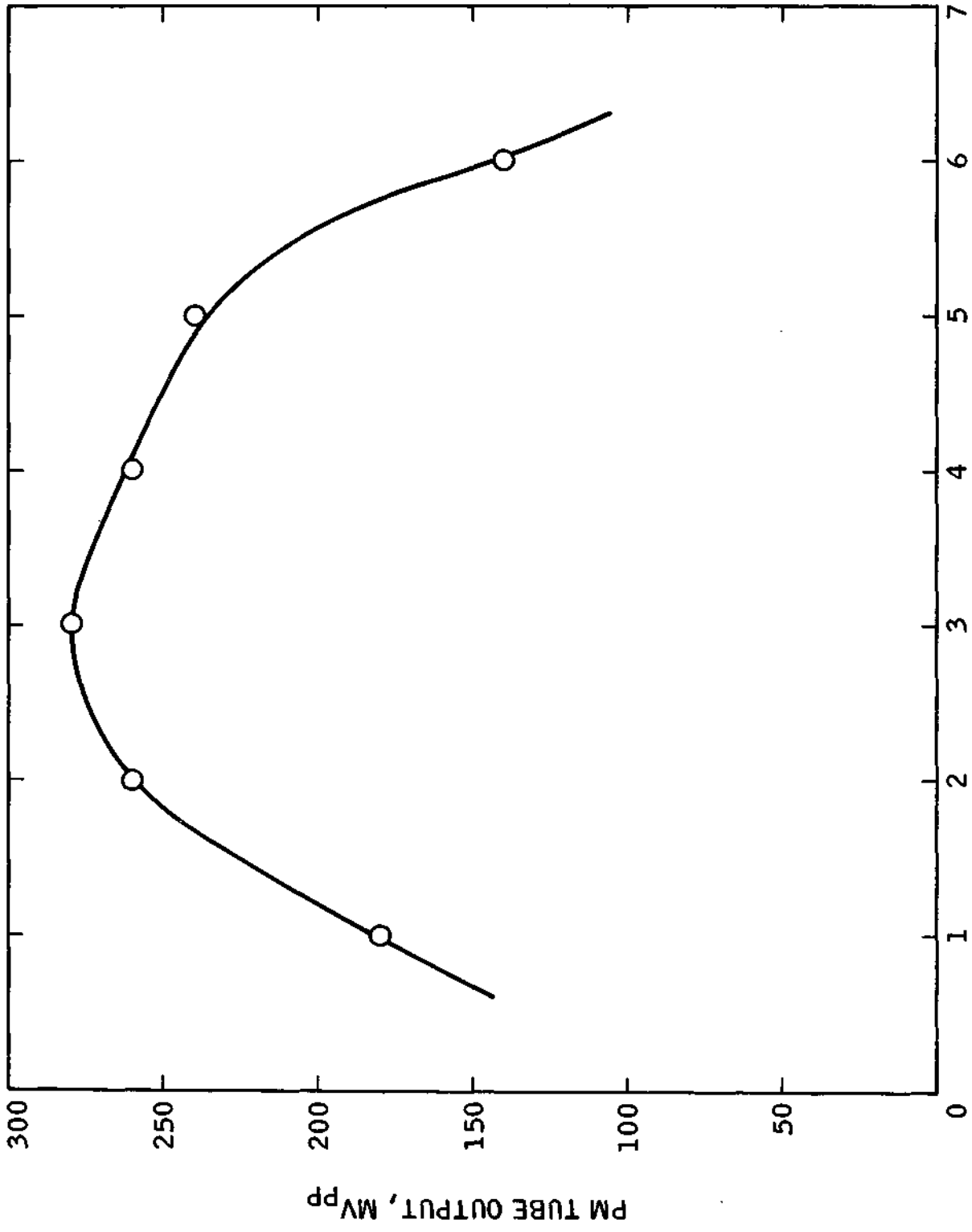

Figure 28. Optical Modulation Depth versus Position, Glass Modulator, One Transducer Activated.

20 percent at 80 V peak-to-peak sinuosoidal drive. The experimental modulation depth near resonance is shown graphically in figure 29 as a function of frequency, exhibiting the width of the resonance curve. The mechanical Q was determined from this data.

2. Casting resin stressed-plate modulators

Borrowing from the techniques used in photoelasticity, the use of several plastic materials as stressed-plate modulators was explored. Photoelastic techniques are used to evaluate stress levels in complex structures by constructing scale models of them in transparent plastic materials and observing their birefringence under load. A number of resins have been identified in this field as having large stress-optical coefficients. One of these is the Araldite 6060 (ref. 5) mentioned below. However, other resins not used in photoelastic HAPOL-1300-1E (ref. 6) and Abelstik (ref. 7), were equally effective and were clear and colorless, unlike the Araldite resin. A number of castings were made from several materials for evaluation of the stressed plate concept. Table IV summarizes the castings and the measurements obtained from them.

A stressed-plate modulator was fabricated of HAPOL-1300-1E casting resin with the dimensions shown in Figure 22, and a thickness of 0.425 inches. Our stressed-plate element had residual strains resulting from the casting process. Care was taken to compensate these residual strains optically at each point prior to any measurement. The fundamental mode of the mounted structure was identified at 2.84 kHz using the same procedures described above for the glass plate. The results of the resonance sweep are shown in figure 30, and the resonant profile of the optical modulation depth is shown in figure 31.

The measured mechanical Q of this modulator was 43. The optical modulation depth was nearly constant along the length of the stressed-plate element, as shown in figure 32. Modulation efficiency

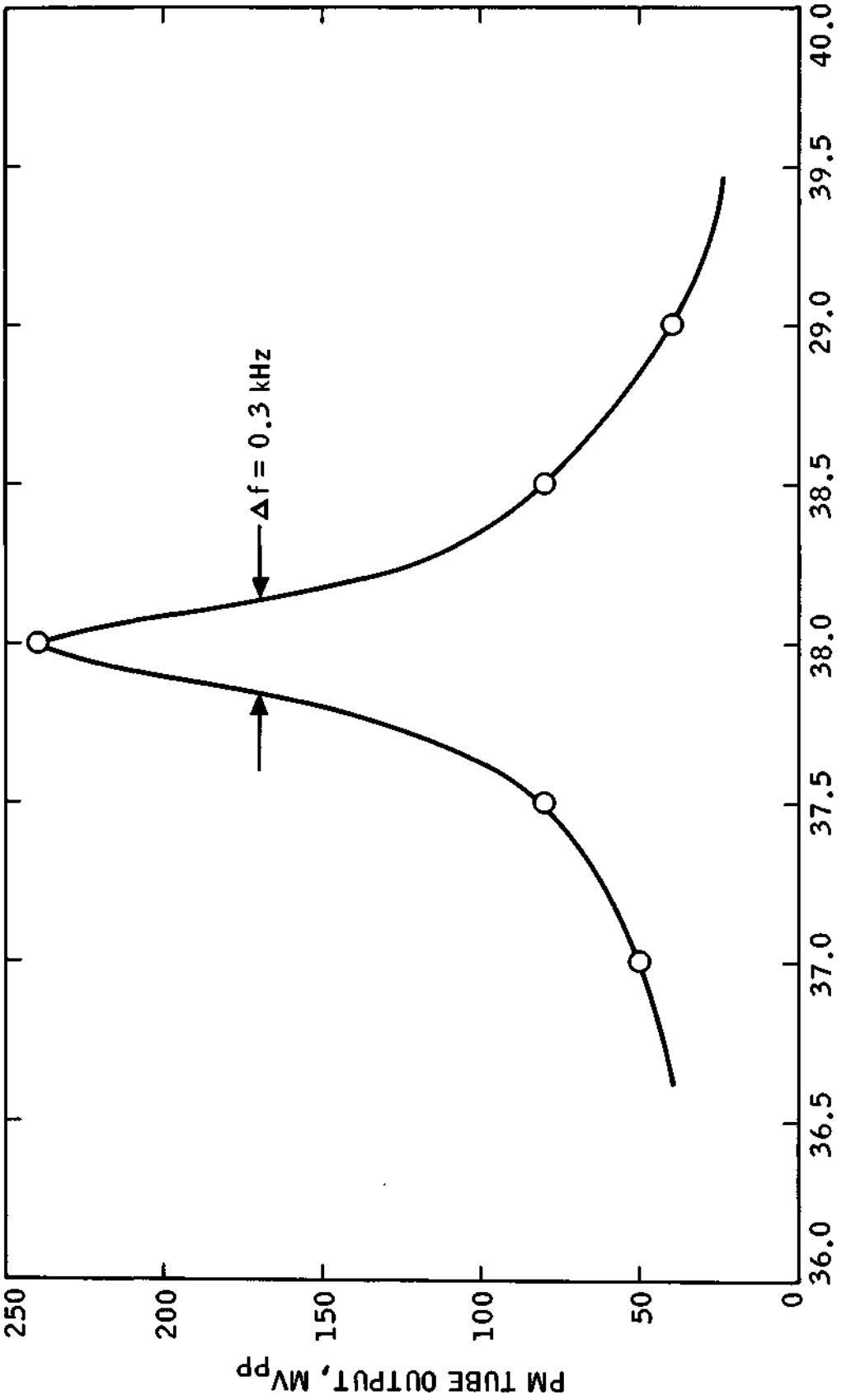

Figure 29. Optical Modulation Depth versus Frequency Near Resonance, Glass Modulator

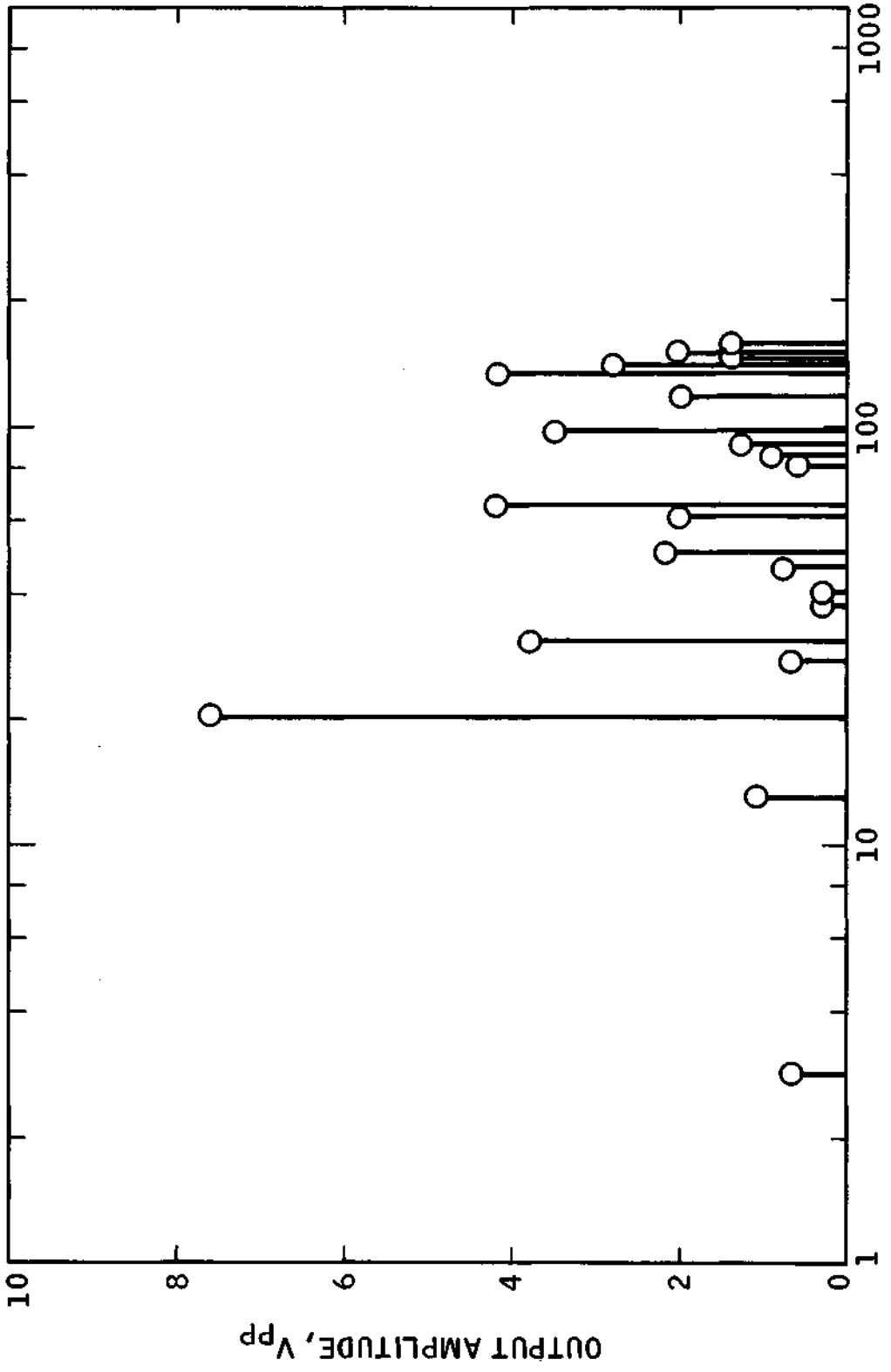

Figure 30. Resonance Sweep

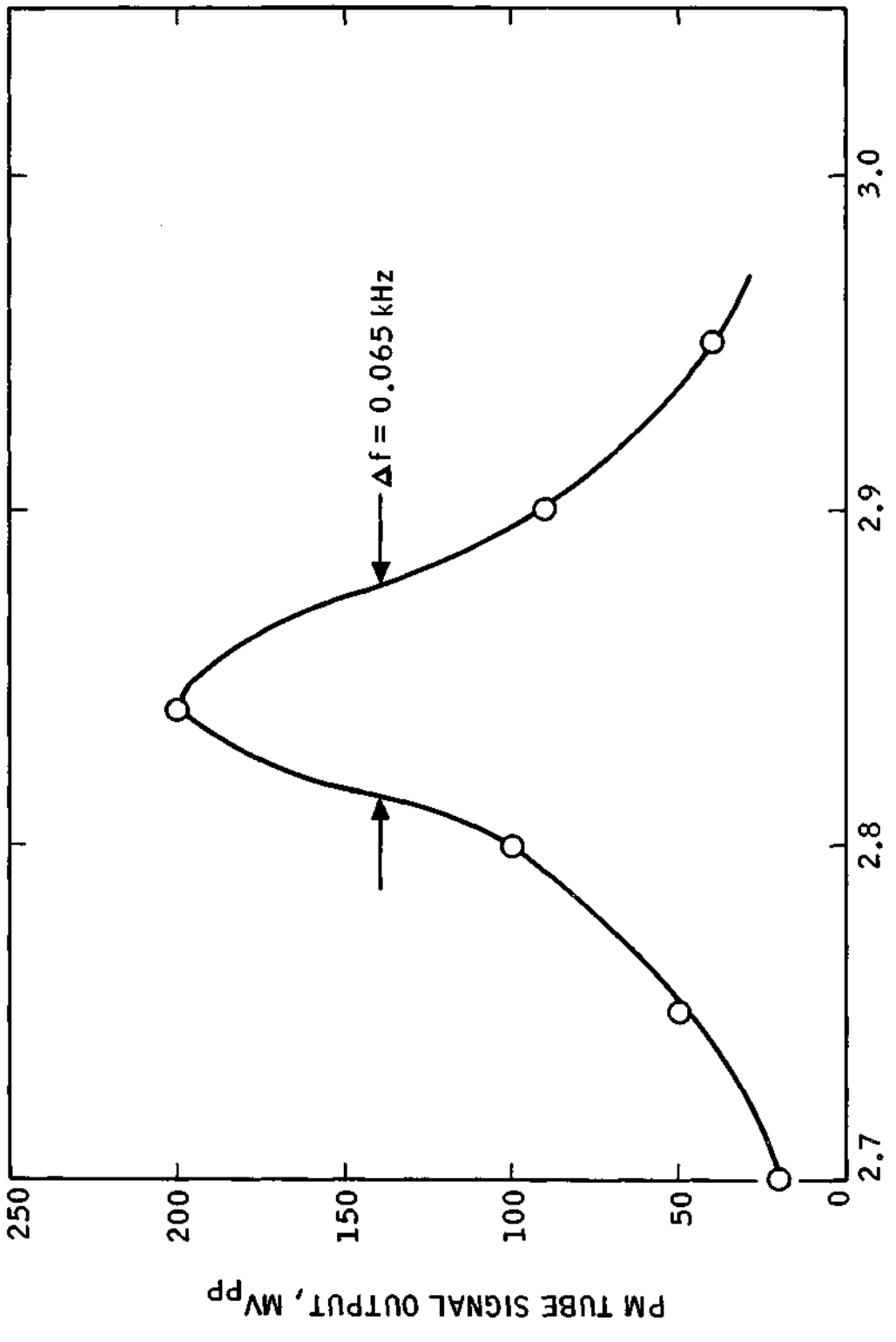

Figure 31. Optical Modulation Depth Resonance Curve for Hepol 1300-1E Resin

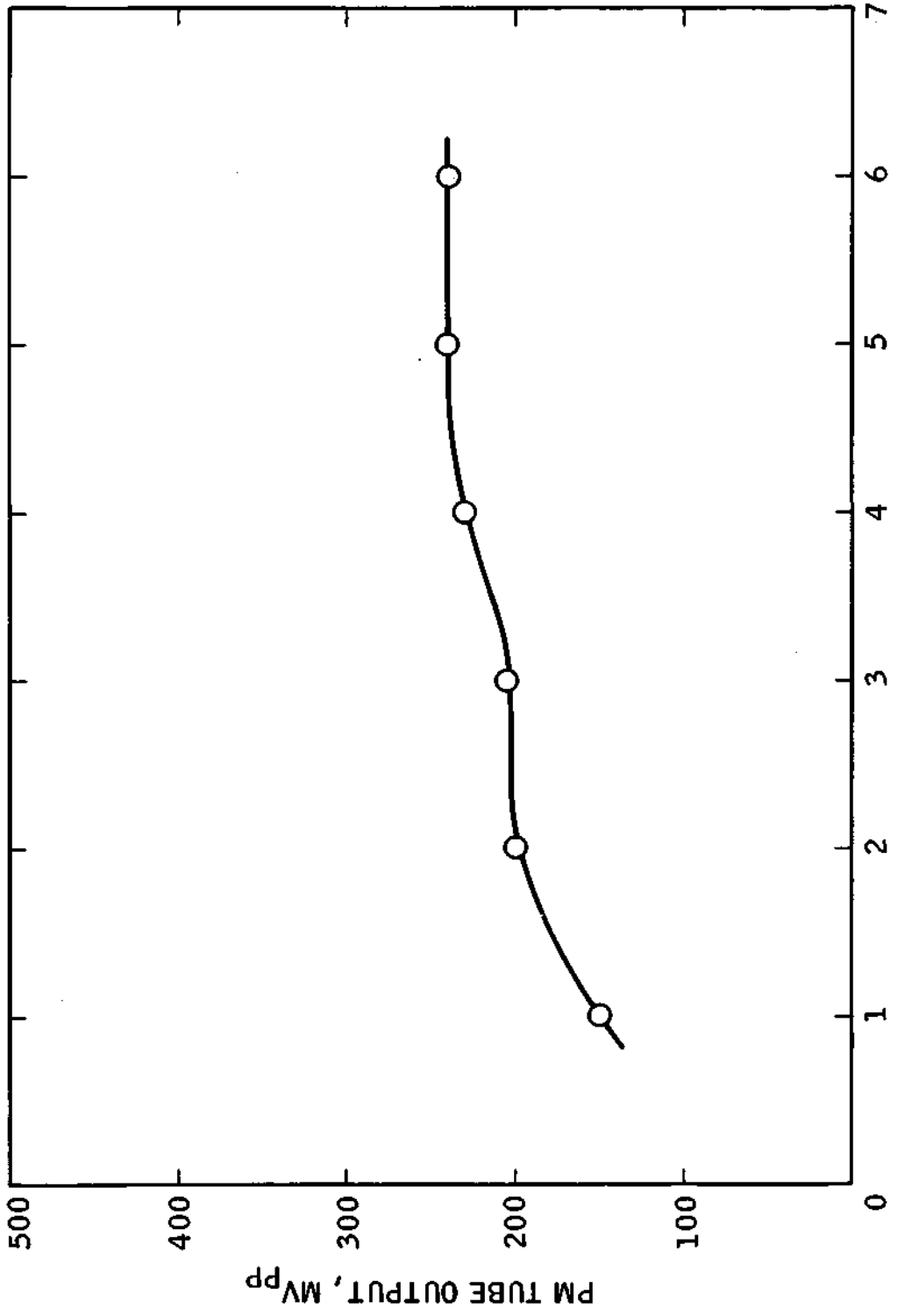

Figure 32. Optical Modulation Depth versus Position, Hepol 1300-1E

TABLE IV. – MODULATOR TEST SUMMARY

Material	Size, Inches	Resonant Frequency, kHz	Q	Efficiency, %	Comment
Glass, Light Crown	3 x 2 x 0.381	38.1	126	20	Highest Q
Hapol 1300-1E	3.x 2 x 0.425	2.84	43	17	
Araldite	3 x 2 x 0.490	2.51	23	23	Yellowish color
Lucite	3 x 2 x 0.5	3.45	38	3	Lowest efficiency
Abelstik 342-1	1.375 x 1 x 0.5	5.3	53	23	
Hapol 1300-1E	1.375 x 1 x 0.5	5.49	91	60	Highest efficiency
Hapol 1300-1E	2 1/4 x 3 1/2 x 1/2				18 castings made
Abelstik 342-1	2 1/4 x 3 1/2 x 1/2				23 castings made
Abelstik 342-1	2 3/4 diam. x 5/8 thick				2 castings made

was measured as approximately 17 percent, roughly the same as was measured for the glass stressed-plate modulator at the same drive voltage.

The effects of modifying the end-weights on resonant frequency, mechanical Q, and modulation depth, were investigated using this modulator. End-weight increments of 35 grams were added to each end and the modulator was then tested. The resonant frequency depended on loading, as expected, but the mechanical Q remained relatively unchanged. The modulation depth was unaffected by changes in the end-loading. The results of these tests are shown in figures 33 and 34.

A second plastic stressed-plate modulator having a thickness of 0.49 inches was fabricated per figure 22 using Araldite 6060 casting resin. The Araldite 6060 stressed-plate element was also found to contain residual strains induced during the casting process. Residual strains were similarly compensated prior to any measurements.

The fundamental mode resonance was located at 2.51 kHz and the mechanical Q was measured to be 23. The modulation efficiency was 6 percent in the center of the stressed-plate and decreased rapidly off-center. Its utility as a stressed-plate modulator was further degraded by the higher optical attenuation of the yellowish Araldite 6060 material. It was judged that the HAPOL-1300-1E was a far more satisfactory material for use as a stressed-plate modulator.

A third plastic stressed-plate modulator was fabricated from Lucite having the nominal dimensions shown in figure 22. The thickness of the Lucite plate was 0.5 inches. The bonding agent used to attach the PZT-4 transducers was ARON ALPHA No. 102 (ref. 8) because the EPON 828 would not adhere properly to the Lucite material. The Lucite stressed-plate contained relatively small residual strains which also were optically compensated prior to any measurements.

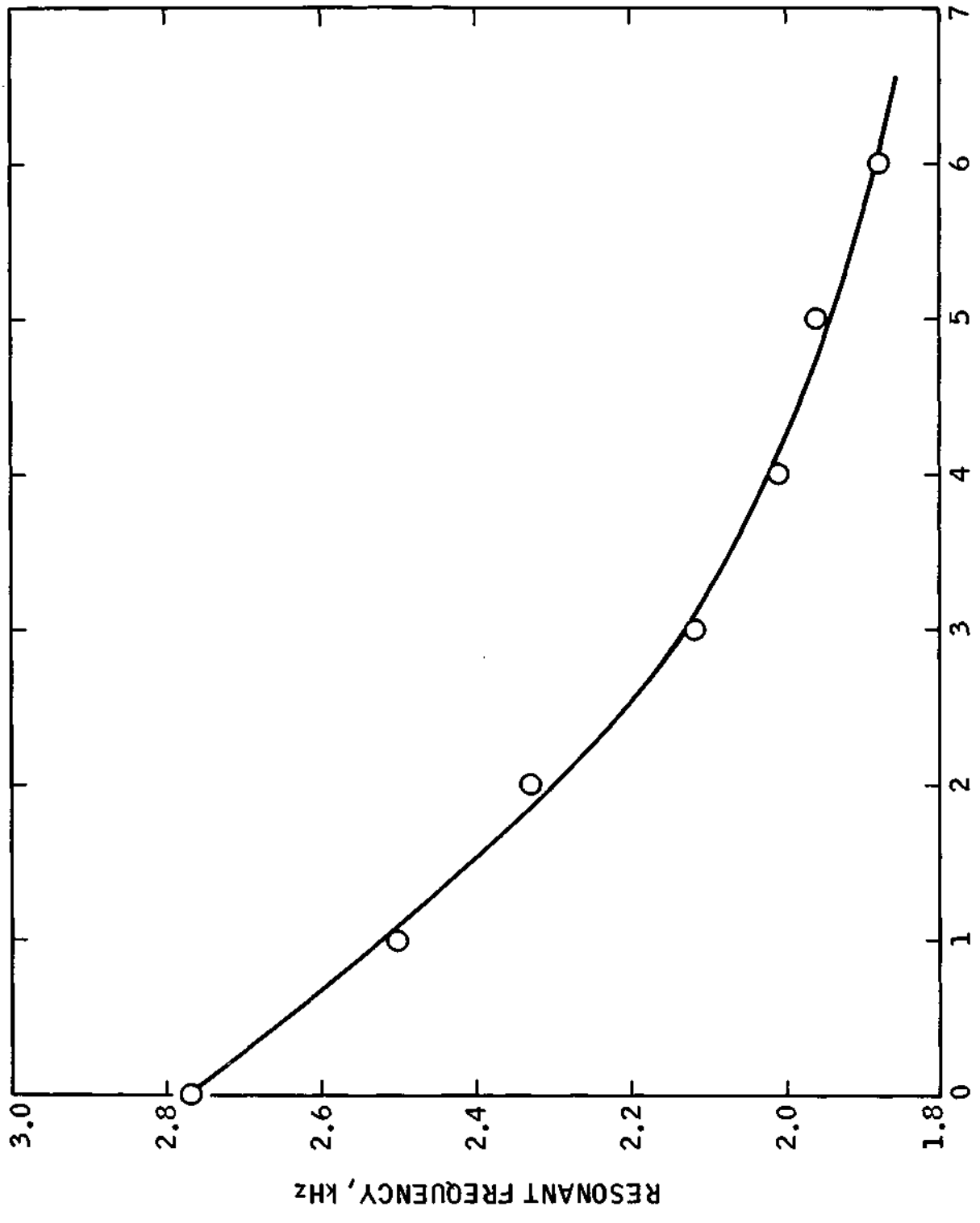

Figure 33. Resonant Frequency versus End Weight, Hapol 1300-1E

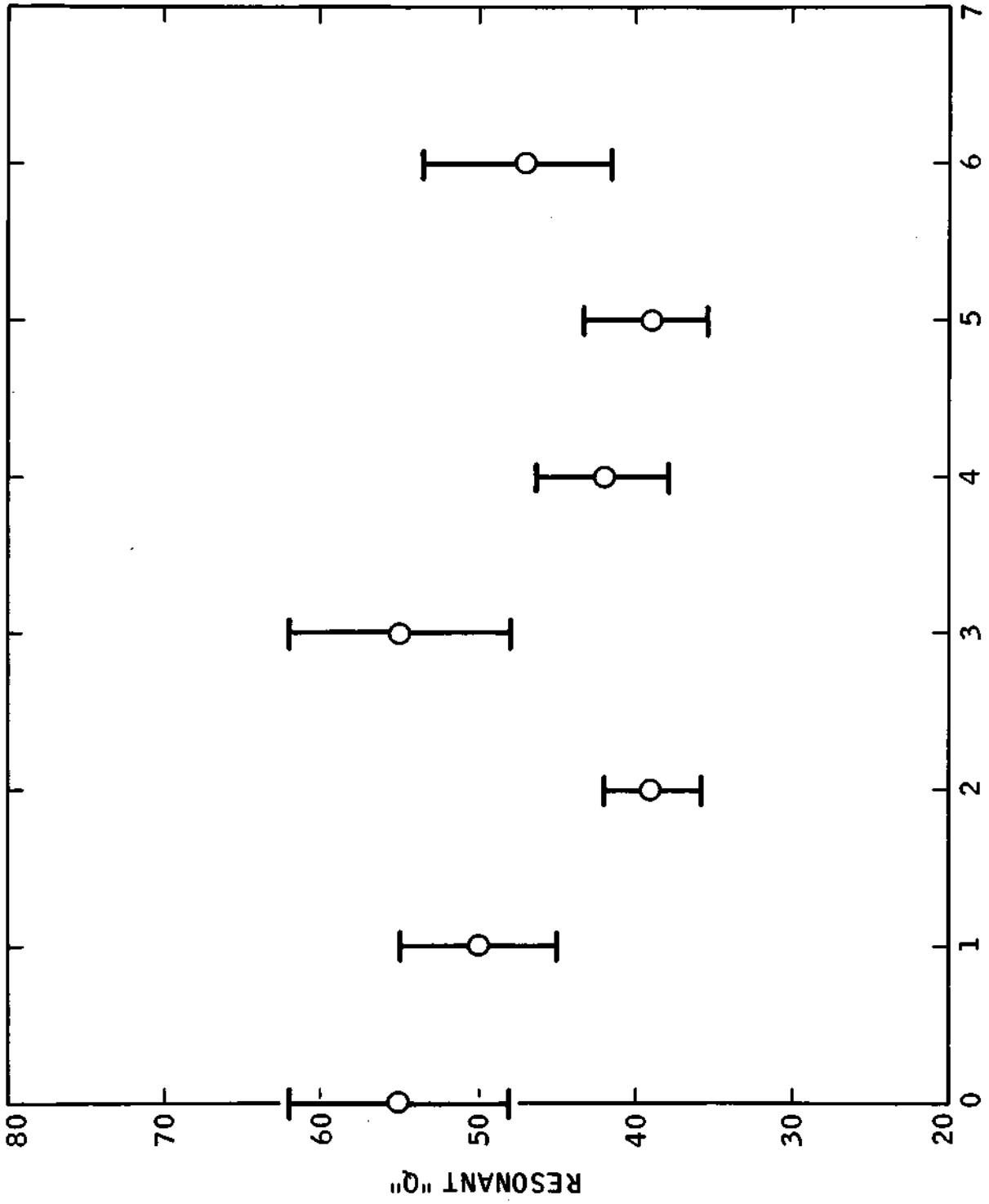

Figure 34. Resonant "Q" versus End Weight, Hapol 1300-1E

The fundamental resonance was located at 3.45 kHz for this modulator with a mechanical Q of 38. The percentage of modulation was measured as 3 percent with a peak-to-peak resonant drive of 80 volts. The percentage modulation, although comparatively low, was quite uniform over the length of the stressed-plate element. No further tests were performed with the Lucite modulator because of its rather low modulation efficiency.

Two stressed-plate modulators were fabricated in a smaller size but using the same structural configuration as the previously-described modulators. The active stressed-plate elements measured 1.375 inches long by 1.0 inches high. The element thicknesses were 0.505 inches. The stressed-plate elements were fabricated from HAPOL-1300-1E and Abelstik casting resins. Both materials are optically transparent and are readily machined and polished.

The characteristics of both of these smaller modulators were far superior to their larger counterparts in terms of mechanical Q and modulation efficiency. The HAPOL modulator exhibited a mechanical Q of 91 at a resonant frequency of 5.49 kHz. The modulation efficiency at the center of the stressed-plate element was measured as 60 percent at resonance, at the same 80 volt peak-to-peak drive. Variations in the modulation efficiency along the length of the stressed-plate were found to be less than 12 percent. The Abelstik modulator exhibited a mechanical Q of 53 at a resonant frequency of 5.30 kHz. The modulation efficiency was measured as 23 percent in the center of the stressed-plate at resonance, with a 10 percent reduction in modulation efficiency at the ends of the stressed-plate.

The small HAPOL stressed-plate modulator was incorporated into the EODS in place of the existing electro-optic modulator to evaluate its performance in the EODS system.

The response of the EODS to a star input, using the mechanically-tuned stressed-plate modulator was then determined. The modulator

was driven at its resonant frequency of 5.49 kHz by an 80 volt peak-to-peak sine wave. Synchronous detection of the resulting EODS output signal was performed as before. The remaining elements of the EODS were set up as during earlier tests. Figure 35 shows the EODS output as plotted against input angle over a range of $-2\alpha_{max} < \alpha < 2\alpha_{max}$. Figure 36 is an actual recorder plot of sensor output made by scanning the star angle at a constant slow rate with a motor. The EODS response shown in figures 35 and 36 illustrate that satisfactory performance can be obtained with the mechanically-tuned stressed-plate modulator while at the same time improving the efficiency of the modulation method.

The improvements in efficiency to be obtained by using a resonant stressed-plate structure depend largely upon the mechanical Q and modulation efficiency of the structure. The obvious advantage of the stressed-plate is that high-voltage (1000 V rms) modulator drive is no longer required and the electronic circuitry becomes simpler and more reliable. The HAPOL modulator used in these final experiments represented an efficient but by no means optimum structure. Further investigations would be desirable to optimize the mechanical Q and modulation efficiency of the structure. Additionally, a physically smaller structure with the same clear aperture would be desirable to minimize the size of an EODS optical package.

ADP Wave Plate Modulator

This phase of our activity was directed toward the construction and evaluation of an electroded ADP combination directional wave plate-modulator element. The material selected was ADP rather than KD*P because of its larger electromechanical coupling.

Considerable data exists on the characteristics of electromechanical coupling in ADP, because of its early use as an ultrasonic transducer (ref. 9). Examination of this data indicates that a plate cut with [1, 1, 1] orientation would be efficiently excited in the desired stress pattern by an electric field in the

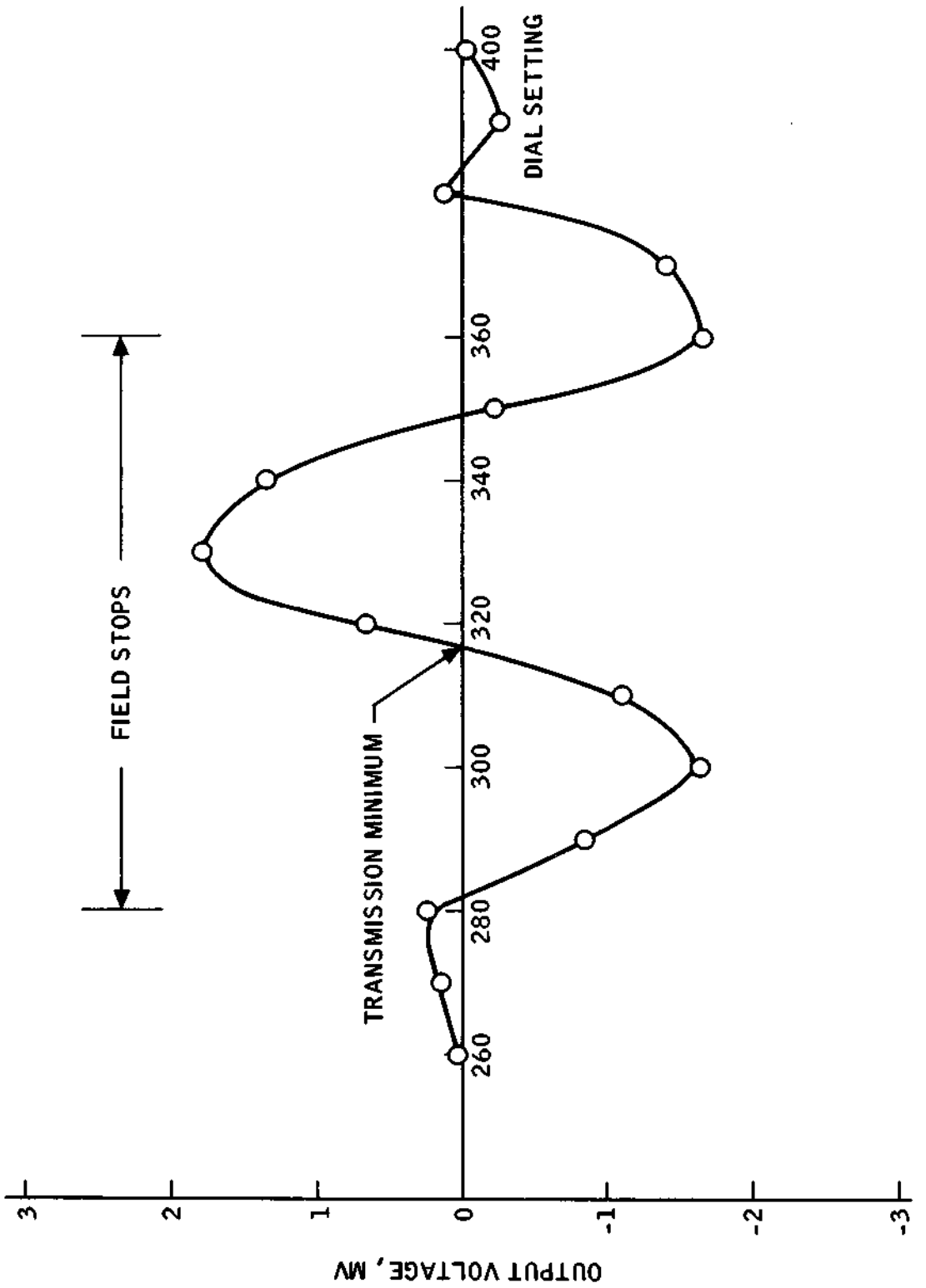

Figure 35. EODS Response to Star Input using Hapol 1300-1E Modulator

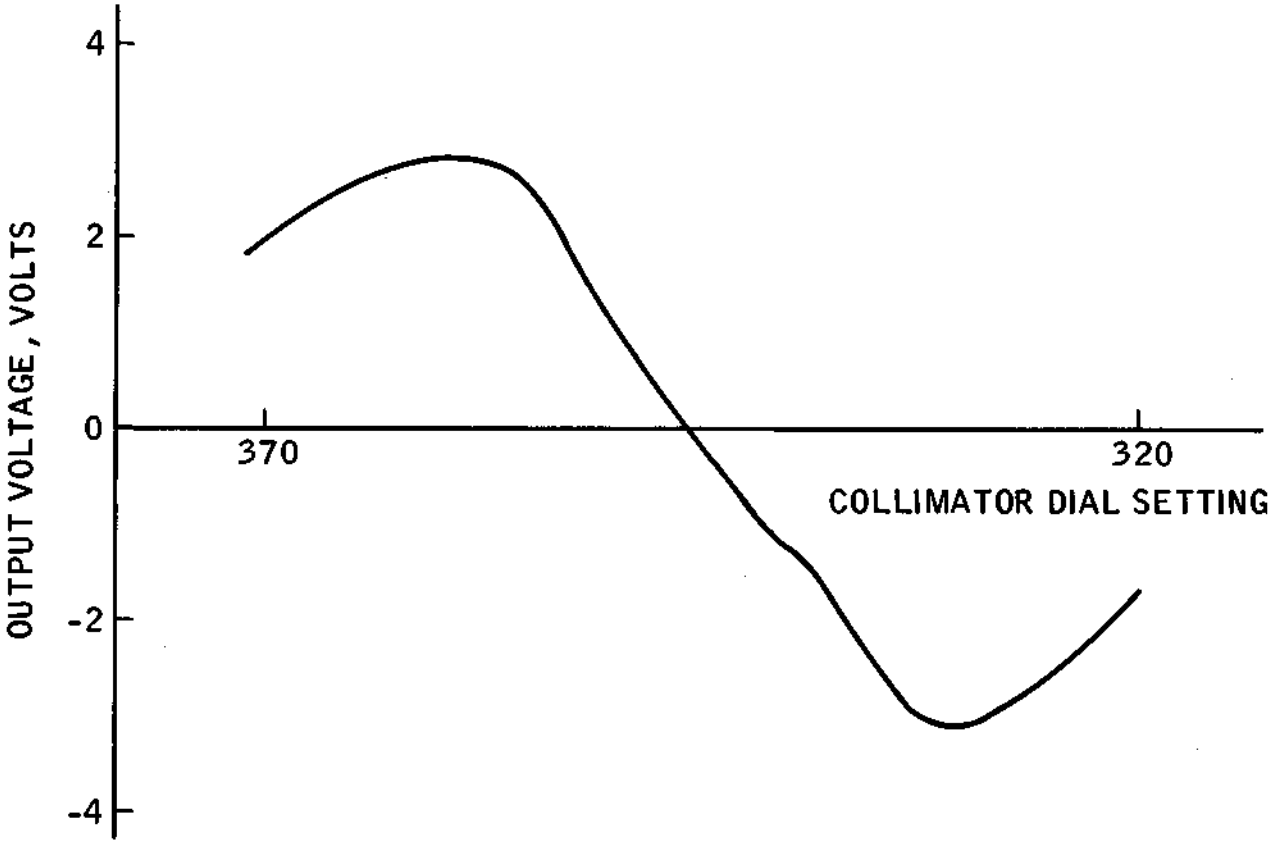

Figure 36. EODS Response to Star Input using Stressed Plate Modulator

direction of its thickness. The [1, 1, 1] orientation places the optic axis at roughly 45°, so the same plate could perform as the DWP.

Accordingly, we sought to evaluate a configuration shown in figure 37. The combination DWP-modulator would have its "c" axis at 45°, and the two "a" axes equally inclined as shown in the figure. The plate was rectangular with length to width ratio of roughly 1.5 to 1 to separate the frequencies of the extensional mode in the two directions. The desired mode would involve stretching along the longer dimension of the plate.

When an ac voltage is applied across the plate, two effects occur. There will be a direct electro-optic response, not connected with mechanical resonance. This response will be considerably smaller than that from a conventionally oriented KD*P plate. A stress optic birefringence induced by the electromechanical coupling of the material and amplified by the resonance will be superimposed on the direct effect. It was hoped that the combined response at resonance will produce a highly efficient modulator element.

To test this hypothesis, a small 5 mm x 5 mm 45° cut plate was made up. This ADP test sample was mounted between NESA-coated glass plates and electrically excited at a frequency of 500 Hz. Electrical contact to the ADP sample was assured by glycerin wetting the contact surface of the NESA-coated glass support plates and the contacting ADP surface. A quarter-wave plate was cemented to the output side of the ADP structure for optical compensation — a substitute for the compensator element in the EODS DSM. The completed assembly was held together by spring clips and mounted on an optical bench support fixture. The modulator assembly was then aligned within the optical test configuration shown in figure 24.

The fundamental resonance of the ADP test plate was located at 86 kHz with a measured Q of 43. A driving voltage of 100 volts peak-to-peak was used. At this level of driving voltage, a modulation efficiency of 2 percent was recorded. The mechanical Q and perhaps also the modulation efficiency were undoubtedly affected by the viscous damping effects of the electroding method used. Figure 38 shows the resonance characteristic obtained.

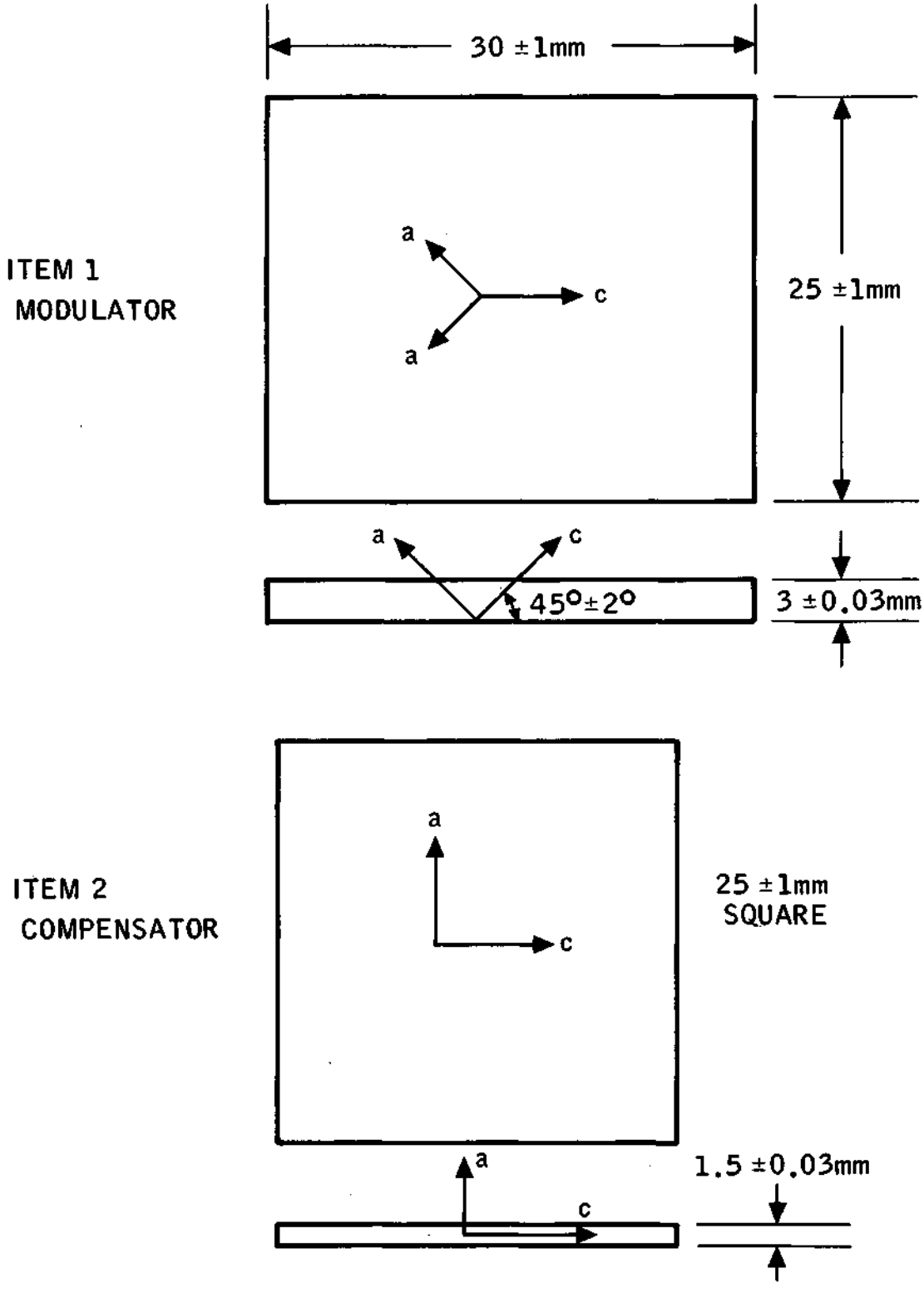

Figure 37. Configuration of the ADP Combination Wave Plate – Modulator and its Matching Compensator.

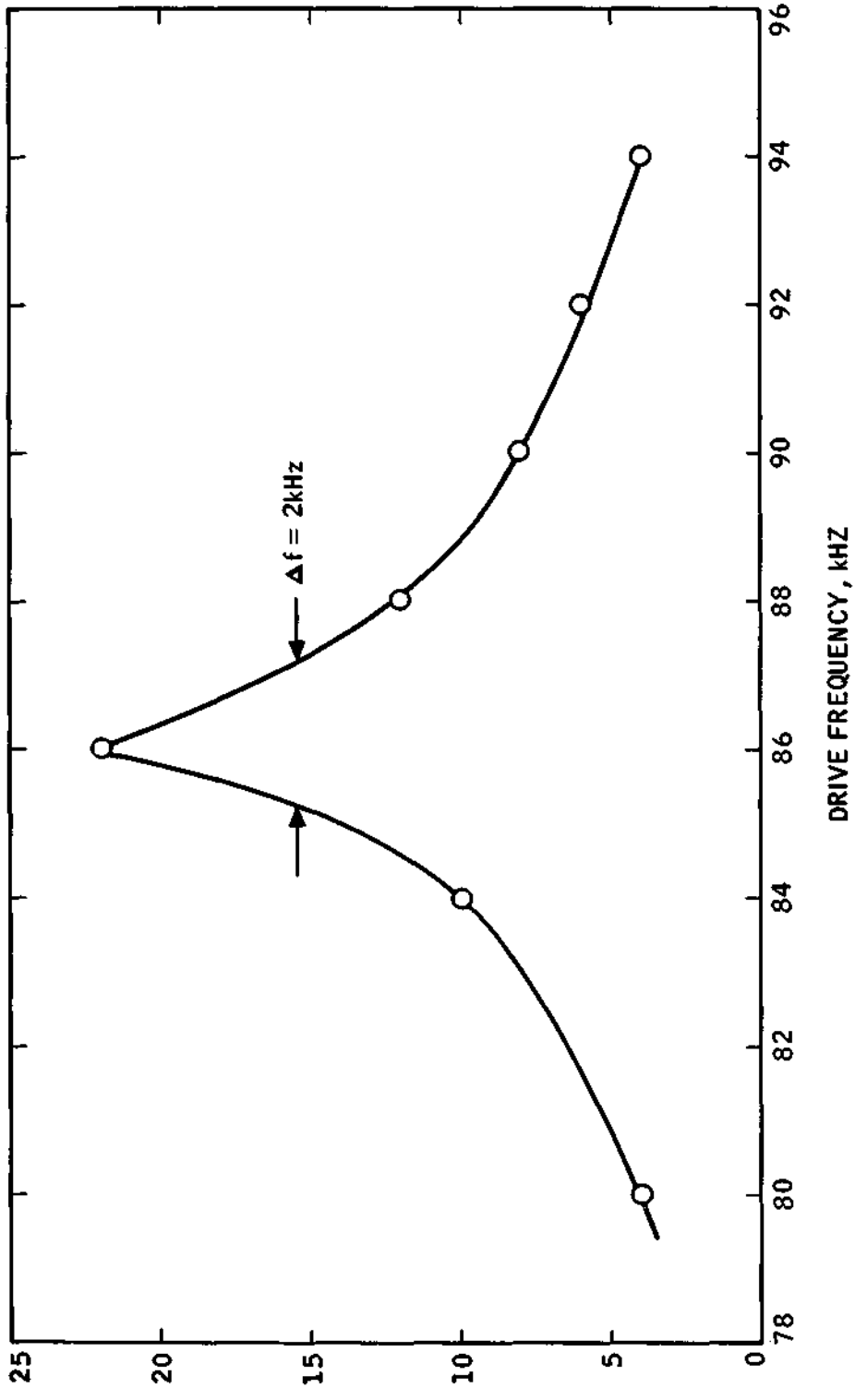

Figure 38. Modulation Characteristics of ADP Test Sample

The equivalent electro-optic constant for this ADP sample was also measured at 500 Hz at driving voltage levels of 50, 100, 150, and 200 volts peak-to-peak. The value obtained for the effective electro-optic constant was 1.32×10^{-4} radian per volt peak-to-peak. This constant refers to the rotation of the plane of polarization of the incident light per volt of excitation and is roughly one order of magnitude smaller than the figure for KD*P. This suggests that resonance could indeed yield a highly efficient modulator.

Although not conclusive, these results were sufficiently encouraging that a design specification was prepared and a purchase order placed with Isomet Corporation for an electroded ADP wave plate and compensator. Figure 37 illustrates the configuration ordered. Properly electroding the ADP material should result in higher mechanical Q and consequently a greater modulation efficiency than was exhibited by the test sample.

Unfortunately, the wave plates were not received in time to evaluate them experimentally under the present task. However, their optical quality is excellent. A quick electrical check resulted in 10 percent modulation at 40 volts peak-to-peak drive at 48 kHz. This data point extrapolates to a drive voltage requirement of 100 V rms at 48 kHz. Firm conclusions regarding the tuned ADP plate must follow from a complete evaluation, so at the present, this approach remains an interesting and perhaps a very promising possibility.

VIII. HORIZON SENSOR OPERATION

Objectives

The objectives of this phase of the development activity were to demonstrate the EODS in a horizon sensing configuration. The ability of the EODS to generate a usable error signal when viewing a diffuse luminous source containing a dark-to-light boundary (horizon) was evaluated. The relationship between the star signal output and the horizon signal output were to be investigated in terms of form relative null position. The effects of modifying the EODS field stops on horizon sensing error signal output were also determined.

Theoretical Analysis

The analysis of the form of the EODS sensor output with a horizon source begins by considering the previously derived (ref. 1) expression for the output signal from a point source,

$$V_o = I_o \eta T R G^{1/2} \sin\left(\frac{\pi\alpha}{2\,\alpha_{max}}\right) \tag{13}$$

where

η = modulator drive factor

I_o = collected light flux

T = transmission of optical elements

R = detector responsivity

G = power gain of phase sensitive detector

α = angle being sensed

α_{max} = center to edge field-of-view

Define an instrument constant, M, such that

$$M = \eta T R G^{1/2} \tag{14}$$

then the sensor output expression may be simplified to

$$V_o = I_o M \sin\left(\frac{\pi\alpha}{2\,\alpha_{max}}\right) \tag{15}$$

Assume a perfect field stop that completely attenuates the input light flux beyond the limiting angle, α_f, such that

$$I_o = 0 \text{ for } |\alpha| \geq |\alpha_f|$$

and is independent of the modulation function, η.

The flux collected by the EODS in an increment of angle, $d\alpha$, is

$$Io\alpha = A\delta B(\alpha)d\alpha \,(\text{watts}/\text{cm}^2) \tag{16}$$

where

A = collecting aperture area

δ = accepted field angle perpendular to the sensitive plane

$B(\alpha)$ = source radiance

and the EODS output for a distributed source within the field stop limits, $\pm\alpha_f$, is then

$$V_o = \int_{-\alpha_f}^{\alpha_f} A\delta B(\alpha)M \sin\left(\frac{\pi\alpha}{2\,\alpha_{max}}\right) d\alpha \tag{17}$$

Since $B(\alpha)$ is translated in α if the sensor axis moves, let

$$B(\alpha) \rightarrow B(\alpha - \alpha_o)$$

where

α_o = pointing angle of sensor as a whole.

For a horizon input, the corresponding luminance function is

$$B = 0;\ (\alpha - \alpha_o) < 0$$

$$B = B_o;\ (\alpha - \alpha_o) \geq 0$$

which corresponds to an intensity step occurring at $(\alpha - \alpha_o) = 0$

G

Evaluating between α_o and α_f, we have

$$V_o = \int_{\alpha_o}^{\alpha_f} A\ B_o M \sin\left(\frac{\pi\alpha}{2\,\alpha_{max}}\right) d\alpha \tag{18}$$

$$V_o = \frac{-2\,\alpha_{max}\, A\delta B_o M}{\pi} \cos\left[\frac{\pi\alpha}{2\,\alpha_{max}}\right]_{\alpha_o}^{\alpha_f} \tag{19}$$

If α_f is selected to be at a zero of $\cos \frac{\pi\alpha}{2\,\alpha_{max}}$ then the evaluation of eq. (19) yields

$$V_o = \frac{2}{\pi}\,\alpha_{max}\,\delta A B_o M \cos\frac{\pi}{2}\left(\frac{\alpha_o}{\alpha_{max}}\right) \tag{20}$$

Comparison of eq. (20) for a horizon source and eq. (13) for a point source indicates that there is a relative null displacement of magnitude α_{max} between the two sensor outputs. The sensor outputs for a point source and horizon source then have the same general form, providing that the field stops are set at a zero of the cosine term in eq. (19). The field stops must be carefully set at $\alpha = -\alpha_{max}$ and $\alpha = +3\,\alpha_{max}$ for the horizon sensor to function properly. These characteristics are experimentally verified in the results which follow. The calculated EODS output in the horizon sensor configuration is shown in fig. 39.

Experimental Procedure and Results

The horizon sensor evaluation tests were performed with the EODS unmodified with the single exception of the field stops, which were made adjustable along the sensing axis. The EODS modulator was driven at a frequency of 500 Hz at an rms level of 1000 volts.

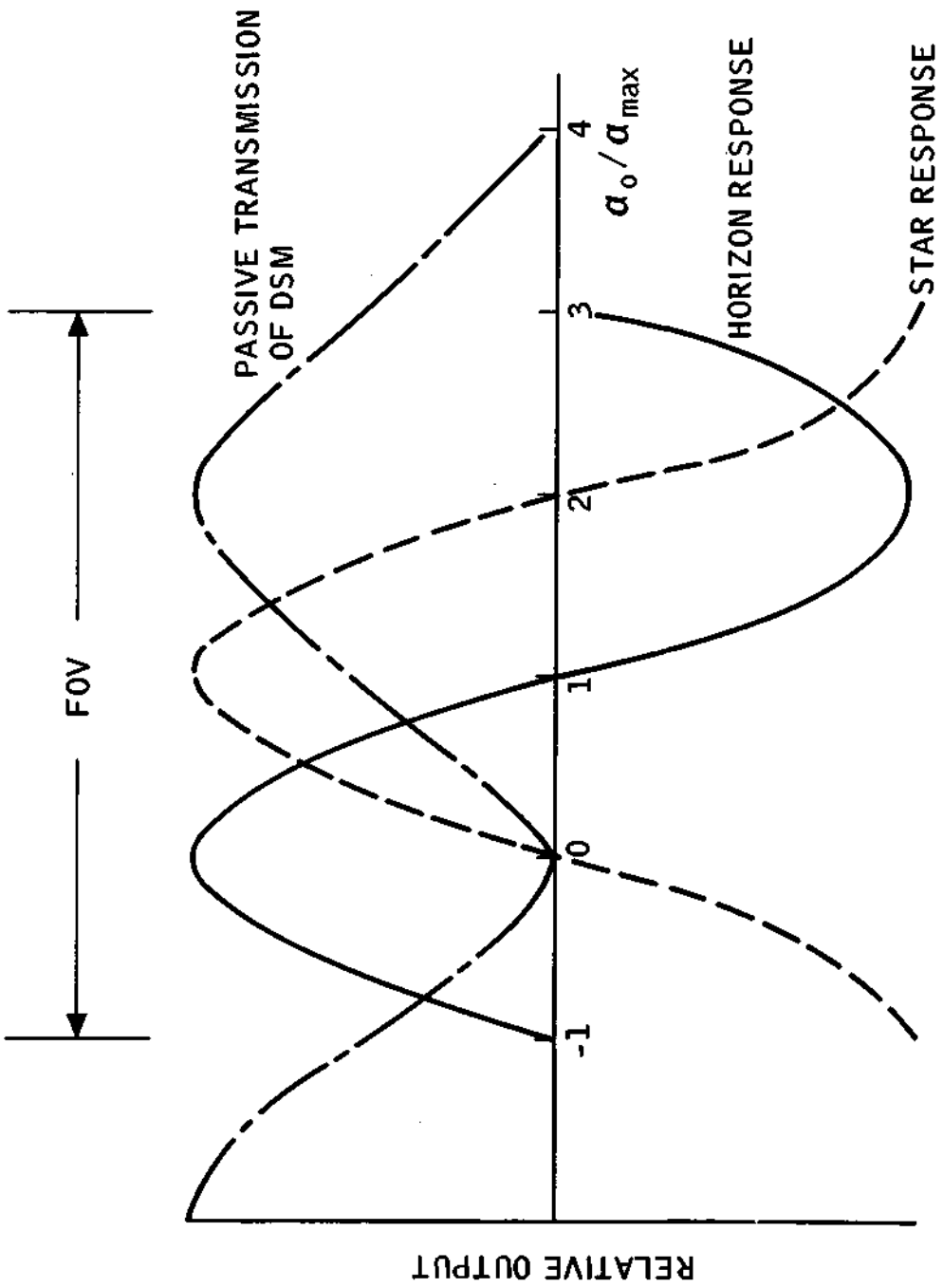

Figure 39. Calculated EODS Response in Horizon Sensor Configuration

The test collimator was modified to accept a simulated horizon source aperture and provide uniform illumination of the aperture. Flattening of the illumination field was accomplished by removing the condensing lenses from the collimator light source assembly and replacing them with an opal glass diffuser. The illuminated portion of the horizon aperture was then quite uniform in brightness.

The EODS output was detected by means of a photomultiplier and PAR type HR-8 Lock-In Amplifier. Phase-coherent detection was employed since the modulator drive was also derived from the HR-8. Precise photometric calibration was not maintained during this phase of the tests.

The initial setting of the field stops was determined by recording the EODS output with a star source, as a function of the angle to the source, and subsequently setting the field stops to the points of the desired portion of the EODS output voltage curve corresponding to $-\alpha_{max}$; $+3\,\alpha_{max}$. The adjustment was made visually by positioning the star source to the desired angle and adjusting the field stop to just "split" the star image. Adjustment of the other field stop was accomplished independently in a similar manner. With the field stops thus adjusted, the EODS response was measured for both the star source and horizon source as a function of angular position. The result is shown in figure 40.

The effects of widening the field stops are shown in figure 41. The EODS output in this case shows some degradation in terms of the shape and orthogonality of the resulting curves, with the horizon sensor output being biased away from its nominal position. Narrowing the field stops results in the output curves shown in figure 42. Again the output distortion and lack of orthogonality is clearly evident. The desired field stop positions are shown in figure 40.

In summary, the EODS can be easily configured to operate in a horizon sensing mode. To do so, the field stop must be accurately positioned, and the null position will be offset by α_{max} with respect to the point-source null. Unlike the star-sensing case, the output depends on the field stop position in

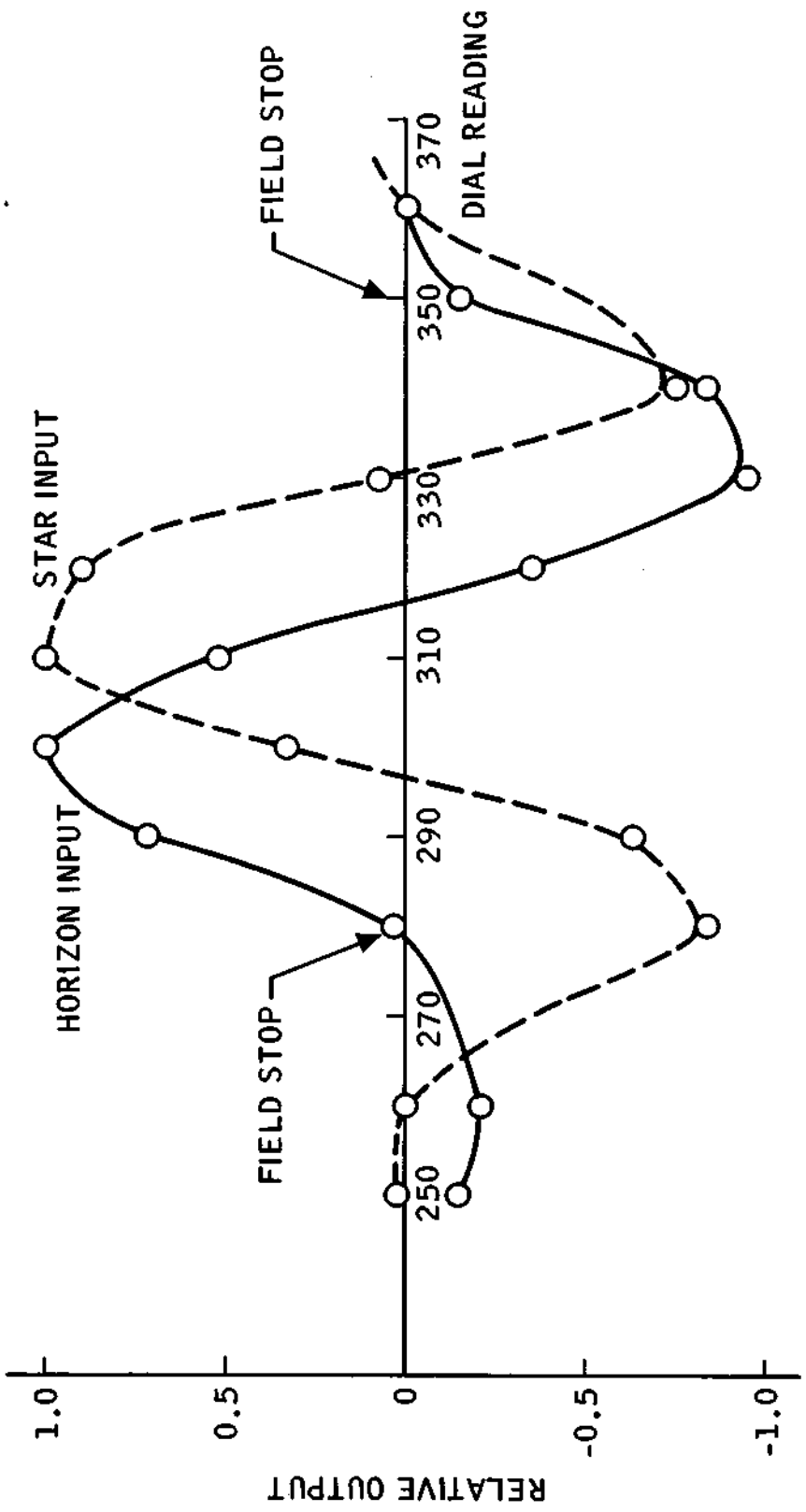

Figure 40. Plot Showing EODS Output when Sensing a Simulated Horizon

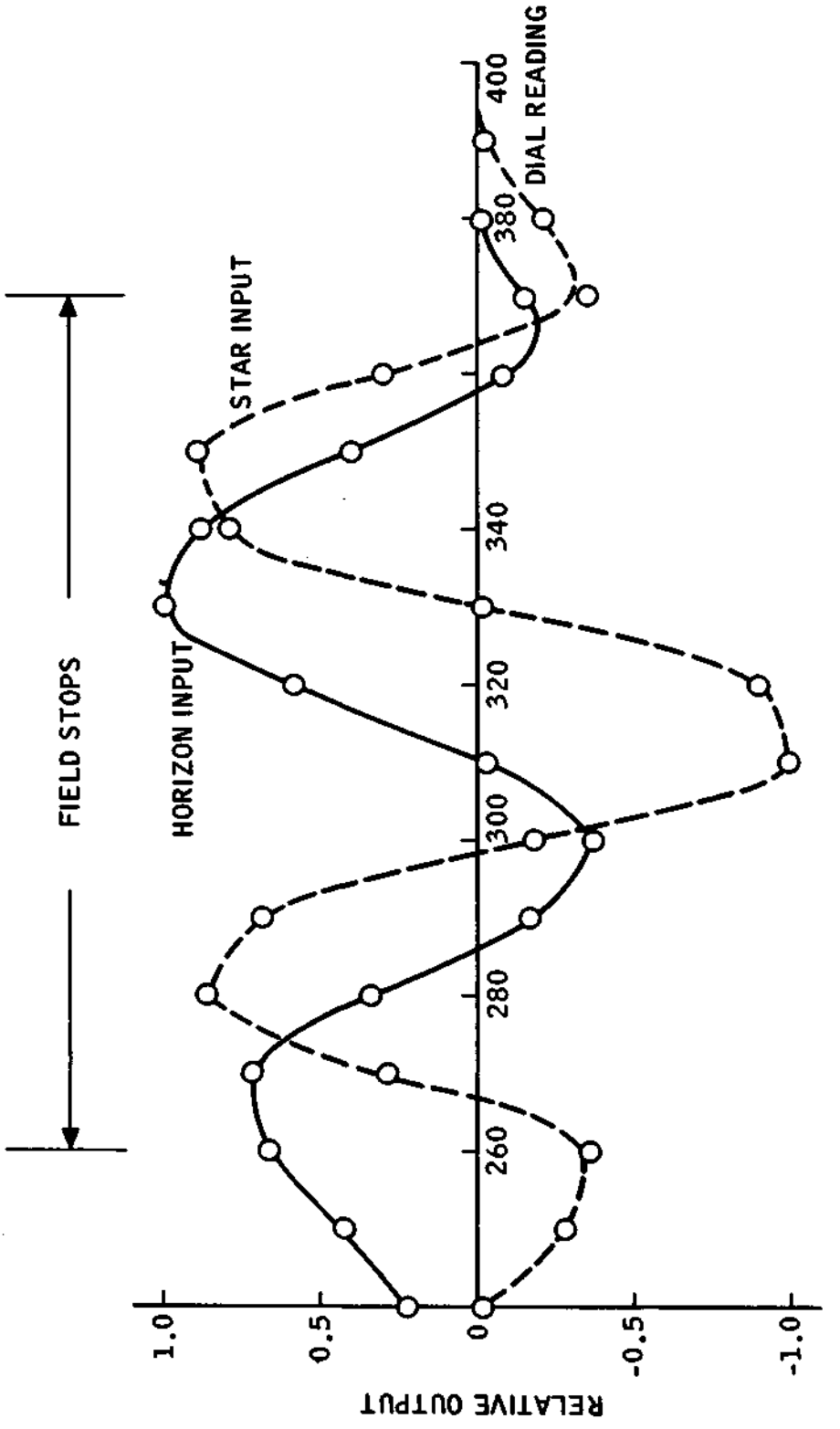

Figure 41. Horizon Sensor Output with Field Stops Placed too Wide. Curves are to be Compared with Figure 40.

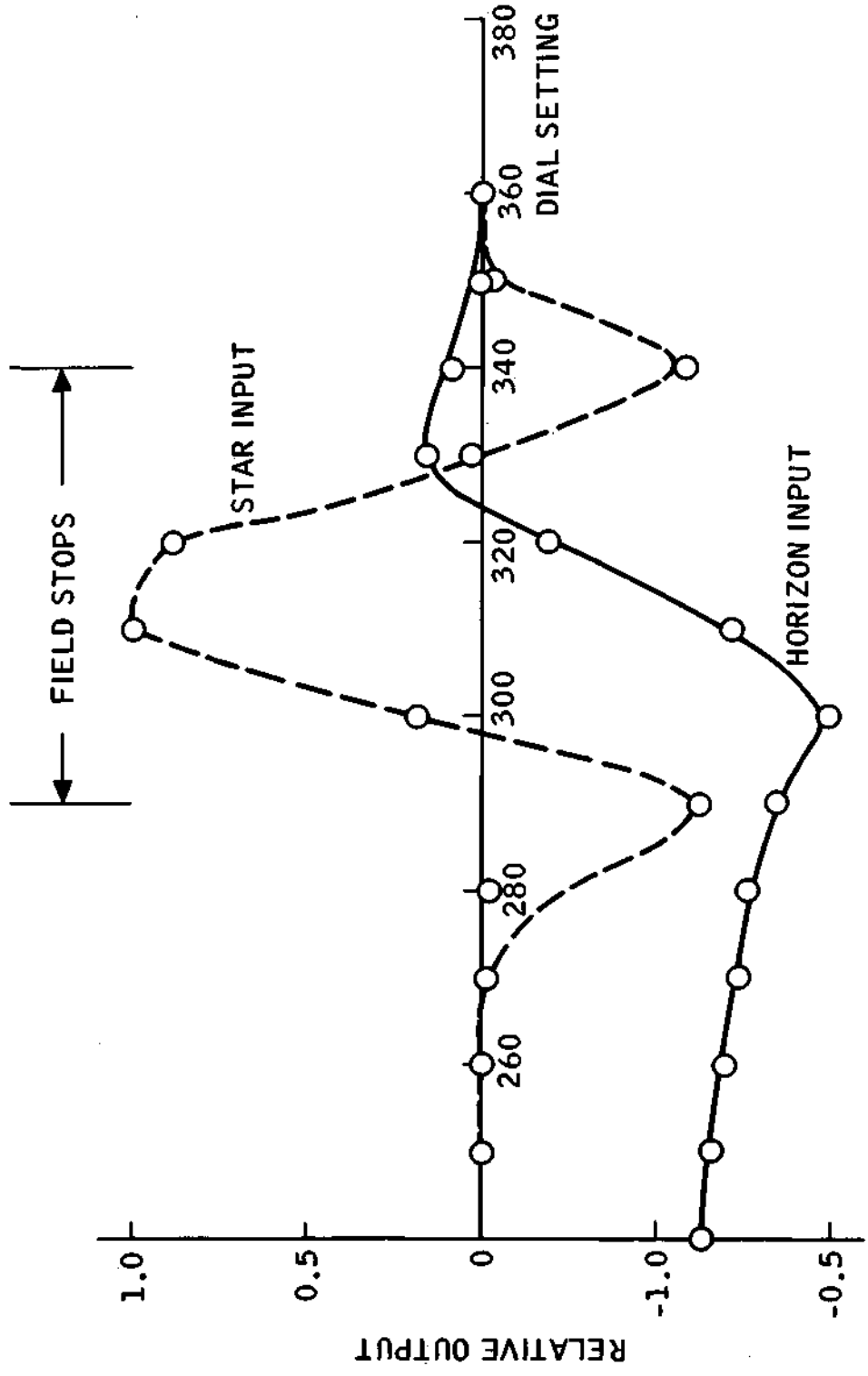

Figure 42. EODS Horizon Sensor Output, Fieldstops too Closely Spaced. Compare to Figure 40.

the telescope optics. The transfer characteristic also depends on the uniformity in brightness of the luminous area. The errors in null position resulting from non-uniform brightness, or physical motion of the stop can be evaluated using eq. (17). Qualitatively, the sensitivity of the sensor to field-stop positioning can be visualized by reference to figures 41 and 42, and to nonuniform brightness by noting that a given fractional brightness variation across the luminous area will produce a null shift of roughly the same fraction with respect to α_{max}. In other words, if $\Delta B/B$ is ~ 0.1, then one expects $\Delta V_o/V_{max} \approx 0.1$ and $\delta\alpha_{null} \approx 0.1\ \alpha_{max}$.

IX. DISCUSSION

Summary of Results

In this section, conclusions are summarized, and, recommendations for future work with the EODS concept are discussed. The questions of modulator type and detector type are examined, and two possible configurations of a prototype EODS sensor are described. The EODS sensors are also compared to an existing star sensor (ref. 11).

It is our present opinion that an EODS using a small photomultiplier and a KD*P modulator is amenable to immediate application. Such a design would be straightforward and would involve a minimum of additional development. KD*P modulators of the type we have used are obtainable from commercial sources and all other optical and electronic parts are standard engineering items.

Application of the more sophisticated mechanically tuned type of modulator, though promising, would require further development work.

Am important question is whether a solid-state detector can be used in place of a photomultiplier, thus eliminating the need for the high-voltage dc supply and avoiding the temperature limitations associated with a photomultiplier. It is indeed possible to use a solid-state detector. However, the quantitative benefits from doing so are not clear-cut, because the much larger dark

noise of the solid-state detector requires a larger light-collecting aperture. In effect, the photomultiplier is traded against larger optics, and qualitatively, the balance between the two approaches appears to be very close. A more detailed analysis based on the experimental data given in this report would determine the most advantageous approach. The answer is expected to depend on the specific application. If the source were brighter than a star, for example, if it were a laser beacon, then the silicon detector might be strongly preferred. Another factor is that the silicon detector requires the best state-of-the-art in techniques and design for the preamplifier. This is not a factor when using a photomultiplier because its internal gain brings the signal up to a more tractible level before it enters the preamplifier.

A special effort was made to determine if the avalanche type of photodiode offered benefits in this sensor application. Our conclusion based on test data from four devices is that no improvement in noise should be expected. The observed N.E.P. of the avalanche photodiodes was essentially the same as that of the silicon PIN devices. We feel this is a coincidence. On paper, the dominant noise source should be dark current, from surface leakage on the detector chip. Since surface leakage follows the internal gain in the avalanche device, better N.E.P. figures should result if the same leakage could be achieved. However, the leakage current of our avalanche photodiode samples was larger than in the Si PIN devices, resulting in the same N.E.P. value.

However, the internal gain of the avalanche diode is quite useful, since it would sidestep the critical first preamplifier stage, and would provide a convenient means for implementing an a.g.c. input. For example, the 2ω acquisition signal could be servoed to a predetermined value by controlling the bias supply of the avalanche diode. This is a useful technique that has often been used with photomultipliers to control the gain of the detector channel.

For these reasons an avalanche photodiode would merit first consideration for a solid-state detector configuration, even though it would initially present more unknowns.

Mechanical tuning of the modulating element to lower the drive voltage appears to be a promising technique. Two configurations were potentially useful, one a mechanically driven, tuned, stressed plate, and the other being essentially a combination of the modulator with the DWP, which was then mechanically resonated. Both offer an order-of-magnitude reduction in drive voltage, essentially an impedance change. The combined modulator-DWP approach has the added advantage of eliminating the modulator as a separate optical element. The combined modulator/DWP approach is an intriguing one well worth further investigation because of the simplification it offers to the EODS concept. Both mechanically tuned modulator types will require further development before reaching their ultimate application. It was for this reason that the well-known KD*P modulator was suggested above for more immediate use in an EODS prototype.

The stressed plate modulator, in particular, needs further study in the area of the service lifetime of the cemented joints used in fabricating it, and also in optimizing its acoustic design. The benefits to be expected from the stressed plate modulator are the complete removal of aperture and field-of-view constraints. Selection of angular scale factor and field-of-view could be based entirely on system requirements that are external to the sensor. Unique requirements of this nature should be present before considering the stressed plate.

Comparison of Proposed Configurations

The configuration an EODS prototype might take using the KD*P-photomultiplier combination is shown in figure 43. The purpose of the sketch is to indicate approximately the sensor configuration. The overall size is based partly on the use of a 3/4 in. diameter (20 mm x 80 mm envelope) photomultiplier. Perhaps 4 cm could be removed from the total length by substituting a smaller tube, such as the RCA 8571. However, the rectangular cathode of an 8571 would have to be used itself as the field stop, as this tube has an opaque cathode used in a side looking configuration well inside the surface of the glass envelope. Therefore, change of angular scale would require a change in the telescope objective lens focal length.

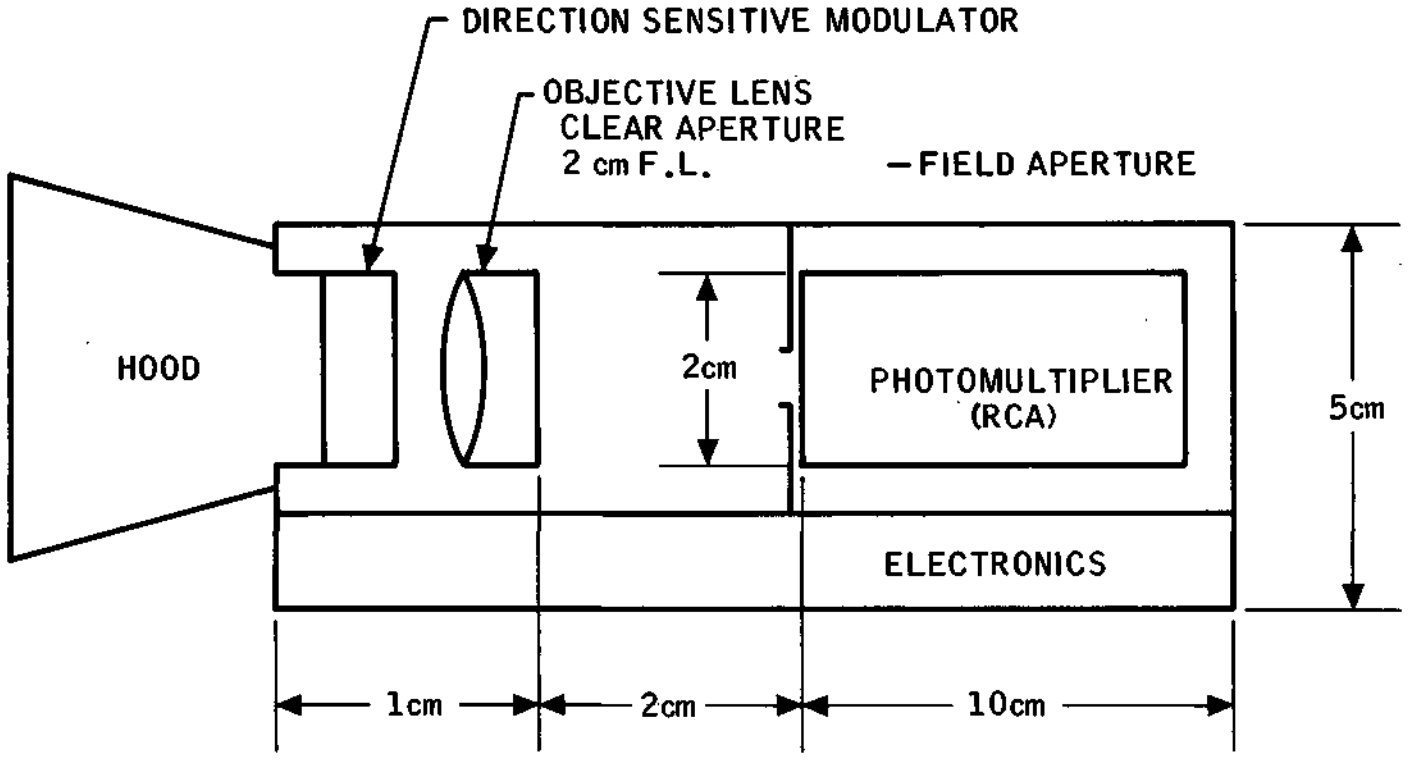

Figure 43. Diagramatic View of an EODS in a Photomultiplier Configuration

The approximate configuration of an equivalent solid-state detector EODS configuration is indicated in figure 44. Note the larger optics.

Several parameters characterizing the two EODS configurations are listed in Table V. It should be remembered that many of the parameters given are not fixed, but rather were arbitrarily selected to present a definite example. Field-of-view and angular scale α_{max}, in particular, can be easily decreased by appropriately changing the DWP-compensator design to as small as $\alpha_{max} \cong 2'$. This could be achieved with a 5 mm thick calcite DWP and would be consistent with an 8' edge-to-edge field-of-view in the sensitive direction combined with any field from the order of 4' to 1^{o} in the cross direction. Corresponding parameters from the Mariner Canopus tracker (ref. 11) are also listed in the table to permit comparison of the EODS with one present state-of-the-art design. In the case of field-of-view, direct comparison is not possible because the Mariner sensor has a tracking capability not shared by EODS. The instantaneous field of the Canopus tracker corresponds most closely with the field of the EODS. Weight for the EODS was estimated from the Canopus tracker weight by assuming it to be proportional to total sensor volume. The required hood size for the EODS units is pure assumption. The hood sizes cannot be directly compared with the Mariner tracker hood except in a qualitative way. The samller size was based on the restricted field-of-view covered by EODS compared to the Mariner sensor.

The importance of systematic drifts can only be estimated for EODS. A reasonable estimate of achievable overall accuracy is given by the effective angular noise input. The noise level is the known limit to accuracy. No drift errors have been identified in experiments that could not be made smaller than the noise level with careful design.

In summary, the applications best fitted to the EODS concept will involve small sensor field-of-view and a requirement for relatively precise pointing. The sensor could be made significantly smaller and lighter than other types of star trackers. It should lend itself to low-cost design, since no expensive items are incorporated. The modulator and wave plate cost in small quantities

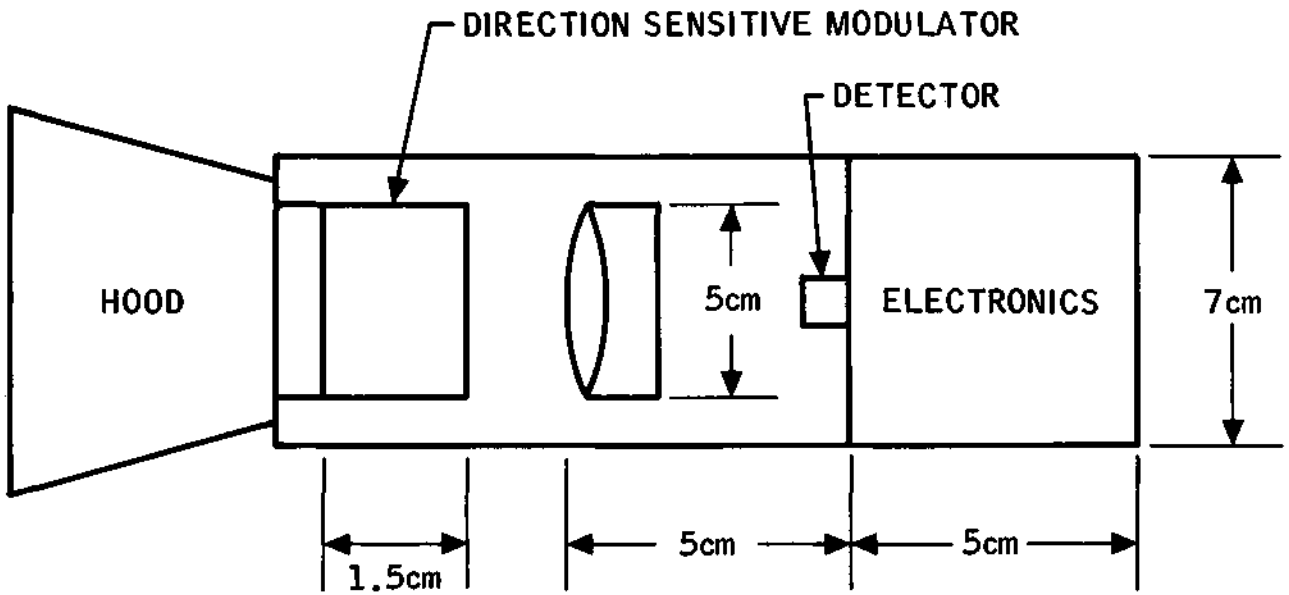

Figure 44. Diagram of an EODS in a Solid State Defector Configuration

TABLE V.– COMPARISON OF TWO EODS' CONFIGURATIONS WITH AN IMAGE DISSECTOR STAR SENSOR

	EODS Photomultiplier	EODS Solid-State Detector	Mariner Image Dissector
Size (no hood)	14 x 5 x 5 cm	14 x 7 x 7 cm	29 x 11 x 13 cm
Hood Size	2 x 2 x 2	10 x 7 x 7	25 x 12 x 12 cm
Weight	0.75 lb	1.5 lb	9 lb
Power	<1 W	<1 W	1 1/2 W
max	0.5°	0.25°	-
Angular Field	2° sensitive 4° cross axis	1° sensitive 4° cross axis	2° sensitive (instantaneous) 10° cross axis 10° x 36° in track mode
Time Constant	1 sec	1 sec	0.5 sec
Aperture	1 cm	5 cm	1 cm
S/N for 0 mag star	100	30	>100
Null Accuracy	0.005° (est.)	0.01° (est.)	0.01°
Noise equivalent input angle	0.005°	0.01°	0.005°

will be in the neighborhood of $500 each for the two or three plates required in a complete sensor.

The potential for low cost and small size opens up an unexplored possibility in optical tracking; namely, that of using multiple independently acting sensors. Multiple sensors for star tracking could be permanently mounted such that each sensor was directed at a different star, thus eliminating the problem of identifying the object being tracked. Redundance would also be obtained from such an approach.

The next step in the development of EODS would logically involve construction of a prototype sensor; that is, one packaged in a form similar to flight hardware, similar to figures 43 and 44. This prototype should be built with a specific application in mind. A multi-sensor satellite attitude control unit or an instrument gimbal pointing device could be suggested as example. Detailed design for achieving a neat small package, environmental testing, and evaluation of null drifts would remain as the primary objectives of such an effort.

REFERENCES

1. Alan R. Johnston, "An Electro-Optic Direction Sensor," J. Spacecraft and Rockets 9, 690 (1972).

2. Alan R. Johnston, "Noise in the Electro-Optic Direction Sensor," Proceedings of the AAFE Principal Investigators Review, Langley Research Center, October 1971, p. 453.

3a. Joseph P. Stephany, "Piezo-Optic Resonances in Crystals of the Dihydrogen Phosphate Type," J. Opt. Soc. Am. 55, 136 (1965).

3b. James C. Kemp, "Piezo-Optical Birefringence Modulators," J. Opt. Soc. Am. 59, 950 (1969).

4a. L.F. Mollenauer, D. Dawnie, H. Engstrom, and W.B. Grant, "Stress Plate Optical Modulator for Circular Dichromism Measurements," App. Opt. 8, 661 (1969).

4b. S.M. Hauser, L.S. Smith, D.G. Marlowe, and P.R. Yoder, Jr., "The Stressed Plate Shutter," Appl. Opt. 2, 1175 (1963).

4c. S.N. Jasperson and S.E. Schnatterly, Revs. Sci. Instr. 40, 761 (1969).

4d. Michel Billardon and Jacques Badoz, Compte Rendu, Acad. Sci. Paris Series B 263, 139 (1966) and Ibid., 262, 1972 (1966).

5. Obtained from CIBA Products, Co., Summit, N.J.

6. Obtained from Hastings Plastic Company, Santa Monica, Calif. HAPOL 1300-1E is a Polyester Casting Resin.

7. Obtained from Abelstik Laboratories, Gardena, Calif.

8. Alpha Cyanoacrylate, obtained from Toagosei Chemical Industry Co., Tokyo; equivalent to Eastman 910.

9. W.P. Mason, "Piezo-Electric Crystals and Their Application to Ultrasonics," van Nostrand, N.Y., 1950.

10. Obtained from Texas Instruments, Dallas, Texas.

11. W.C. Goss, "The Mariner Spacecraft Star Sensors," Applied Optics 9, 1056 (1970).

NASA — JPL — Coml., L.A., Calif.

Reprinted from JOURNAL OF SPACECRAFT AND ROCKETS, Vol. 9, No. 9, September 1972, pp. 690-696

An Electro-Optic Direction Sensor

ALAN R. JOHNSTON*
Jet Propulsion Laboratory, California Institute of Technology, Pasadena, Calif.

A single-axis star sensor is described in which a wave plate having direction-dependent retardation, together with an electro-optic modulator, provides the basis for indicating the direction of a distant point source of light. An alternating current photosignal is obtained, thus avoiding problems associated with detector drift. An analysis of the nominal sensor performance is compared with measurement and found to be in good agreement. The effect of varying the optical geometry on field of view is calculated. The effective noise input is evaluated. Satisfactory tracking of a + 1 magnitude star with a 1 cm aperture and a photomultiplier detector was demonstrated, showing a signal-to-noise ratio of about 50 on an rms basis.

Introduction

A NEW type of star sensor, called an "electro-optic direction sensor," will be described in this paper. It is a device which generates an angular error signal useful for pointing an instrument or for attitude control of a spacecraft by sensing a distant light source such as a star. The sensor is inherently a single-axis device—i.e., it senses an angle in one plane, while its output is independent of angle in the perpendicular direction. Two such devices would be used for pointing an instrument toward a beacon, but one would suffice for roll-axis stabilization of a spacecraft about the sun line. The basic phenomenon on which the sensor depends is the direction-dependent birefringence of an optically anisotropic crystal. No moving parts are involved. An electro-optic modulator permits operation of the detector itself in an a.c. mode, thus avoiding effects from dark-current drift or low-frequency detector noise. A simple detector such as a photomultiplier or low-noise, solid-state detector suffices, as $X - Y$ outputs are not needed.

In the past, three identifiable methods of optical direction sensing have been used frequently and, of course, many variations also exist.[1] Background material on celestial star trackers is given in Ref. 2, and a bibliography is available in Ref. 3. Arrays of detectors can be arranged in the image plane of a lens in such a way that the directional information is obtained by noting which detectors are illuminated.[4, 5] Alternatively, various mechanizations in which the image is either scanned or nutated over a detector have been constructed, usually with a mirror or counter rotating prisms. Mechanical chopping by means of rotating or vibrating elements has also been used[6] rather than scanning. Finally, a technique may be employed in which image scanning is done with electron optics using an image-dissector tube or vidicon.[7] The image-dissector approach has been developed to a very sophisticated state for roll-attitude stabilization of Mariner-type spacecraft about the sun line.[8] In all three approaches, the operation which yields the directional information occurs in the image plane. On the other hand, the essential sensing operation takes place in the entrance aperture instead of in the image plane of the device described in this paper.

Although the three methods mentioned have been successfully applied, it is felt that our device has potential advantages that may be of value in future applications. It would offer an alternative no-moving-parts approach that is independent of the relatively complex and expensive image-dissector tube. It is also relatively simple and compact, and therefore promises good reliability and low weight.

In the following sections, the optical and electronic configuration of the sensor will be described, and the principle of its operation will be explained qualitatively. The behavior of the important optical elements is then analyzed in detail. The results, given in graphical form, would be useful for sizing the optical elements for a given task, and also for calculating the expected output signal. Next, the calculated parameters are compared with experiment for a specific set of optics which were set up on an optical bench. The expected noise behavior of the sensor is then calculated from detector noise-effective power (NEP) figures. The entrance aperture required for a given star intensity, response time, and noise level is estimated and compared with some initial noise data.

Description of the Device

A pictorial diagram of the sensor optics is shown in Fig. 1. The optics can be divided into two main parts: a sandwich of birefringent optics, called a "direction-sensitive modulator," and a set of conventional telescopic optics which collects the light, directs it onto a detector, and also defines a field of view. Since the function of the telescope is straightforward, it will not be discussed further. The direction-sensitive modulator consists of five elements: a polarizer, directional wave plate (DWP), compensator, modulator, and analyzer. Optically, the DWP and compensator are both fixed retarders (optical phase shifters), whereas the modulator acts as a time-varying retarder. A more complete discussion of the anisotropic optics of crystals is contained in a text by E. A. Wood.[9] These elements are illustrated again in Fig. 2, but separated in order to show the optic axis and orientation of each element. The coordinate system shown, with Z along the nominal axis of the sensor, will be used throughout this discussion.

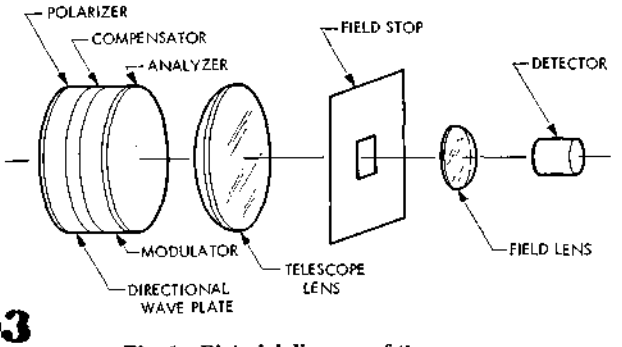

Fig. 1 Pictorial diagram of the sensor.

Received June 28, 1971; presented as Paper 71-966 at the AIAA Guidance, Control and Flight Mechanics Conference, Hempstead, N.Y., Aug. 16–18, 1971; revision received May 8, 1972. This paper presents the results of one phase of research carried out at the Jet Propulsion Laboratory, California Institute of Technology, under Contract NAS 7-100, sponsored by NASA.

Index category: Spacecraft Attitude Dynamics and Control.

* Member of the Technical Staff.

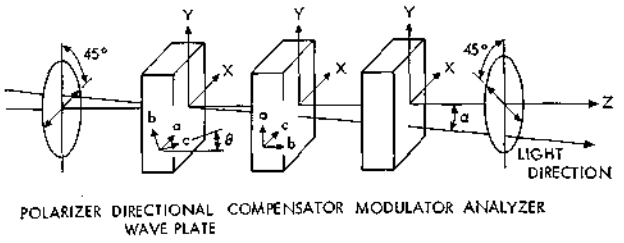

Fig. 2 Diagram of the direction-sensitive modulator, showing the orientation of each component.

The directional wave plate is cut from an optically uniaxial material, such as quartz or calcite, so that the optic axis forms an angle θ with the normal to its faces. It is oriented normal to Z and rotated about Z so that the projection of its optic axis on its surface is parallel to Y. Aligned thus, the birefringent axes of the wafer coincide with X and Y. For near-axial rays, its retardation will depend linearly on the direction of propagation of the light in the $Y-Z$ plane. The inclination of a ray from the Z direction is specified by α in Fig. 2. The compensator is made from the same material as the DWP, but is cut with its optic axis parallel to its surfaces and oriented with its axis along X. Its function is to compensate the large birefringence of the DWP for light traveling parallel to the instrumental axis ($\alpha = 0$), and even more importantly, it compensates the dispersion in retardation so that the device will function in white light.

The modulator, following the DWP and compensator in the figure is oriented such that its induced axes of birefringence are aligned along X and Y. It superimposes a sinusoidally varying (with time, not direction) retardation on the direction-dependent retardation of the wave plates. It is desirable for the modulating element to be isotropic when not being driven in order to avoid distortion of the desired dependence of the total retardation on direction. Unfortunately, this is not the case for potassium dihydrogen phosphate (KDP), the most convenient modulator material, and a field-of-view limitation (to be discussed later) results. The crossed polarizer and analyzer, at 45° to Y, convert the total modulated retardation into an intensity which can be detected and processed electronically.

Taken as a whole, the direction-sensitive modulator behaves like a filter in which the transmission depends on the direction the light travels through it.

A quantitative analysis of the sensor will be made in the next section of this paper, but its function can be qualitatively described in the following way. The directional wave plate and compensator, when placed between crossed polaroids, will exhibit a set of, let us say, horizontal fringes on a distant screen if floodlighted from the opposite side. This pattern of fringes corresponds to the interference figure of a crystal as displayed by a polarizing microscope, and in fact is the interference figure of the direction-sensitive modulator.[9] If the screen is far enough away, a position on the screen will correspond to a specific direction of incidence. When the electro-optic modulator is energized, it wobbles the entire fringe pattern in the vertical direction with frequency ω. The substitution of a distant point source such as a star for the floodlight can be modeled by putting a small hole at the appropriate point in the screen and detecting only the light passing through the hole. The amount of light passing through will be modulated as the fringes move up and down, with phase and amplitude depending on the position of the hole with respect to the unmodulated fringe position. The resulting photosignal is converted to a slowly varying dc error signal by means of a phase-sensitive detector.

A block diagram of the sensor electronics is shown in Fig. 3. The preamplifier is matched to the detector and should be optimized to bring the signal above the noise level of the following electronics in the most expeditious way. The phase-detector reference is supplied from the modulator driver so that the signal component containing the directional information is extracted from the photodetector output at frequency ω. The phase-sensitive detector also provides filtering, which determines the information bandwidth of the device.

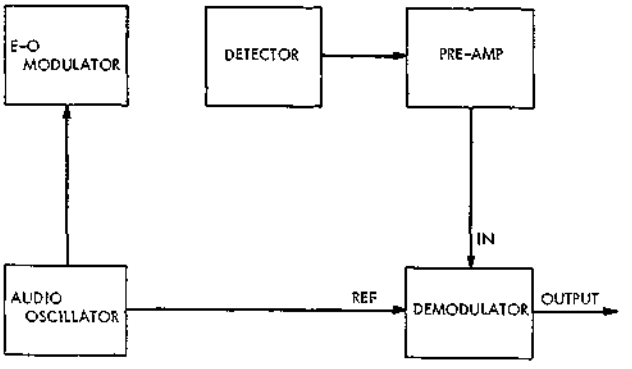

Fig. 3 Block diagram of the sensor electronics.

Analysis

In this section, expressions are derived for the useful angular field of the sensor, for the transfer function between direction and the sensor output, and for the magnitude of the second harmonic component of the photosignal. The latter is potentially useful as an acquisition signal to verify the presence of the light source in the field of view. Both DWP and compensator are assumed to be plane-parallel slices of thickness t_w and t_c, respectively, of the same optically uniaxial material. The geometry has already been given in Fig. 2. An incident light beam from a distant point source is assumed. The direction of propagation of this plane wave is specified by a unit vector $\bar{S}$ along the wave normal.

$$\bar{S} = S_x, S_y, S_z \tag{1}$$

Consider first the directional wave plate. Its crystallographic axes are the system a, b, c, with c in the $Y-Z$ plane at an angle θ to Z. In general, the angle θ is not small. The orientation of the identical a and b axes is not important, but for convenience we arbitrarily choose a along X.

In the crystal, the extraordinary index (E vector of light in the $Y-Z$ plane) will depend on the angle between the wave normal and c. Accordingly, the direction of the wave normal within the crystal must be found with respect to the a, b, c coordinates in terms of the direction $\bar{S}$ of the incident light. Inside the wave plate, the wave normal is bent toward the Z axis, resulting in a new propagation vector $\bar{S}'$

$$\bar{S}' = S_x', S_y', S_z' \tag{2}$$

Assuming that the ray is nearly parallel to Z, $S_x \approx S_y \approx S_z$, and

$$S_x' = S_x/n_e;\ S_y' = S_y/n_e \tag{3}$$

Similarly, the components of $\bar{S}'$ can be given, with respect to the crystal system, as

$$\bar{S}' = p, q, r \tag{4}$$

The components p, q, r can be obtained from S_x', S_y', S_z' by means of a coordinate rotation, with the result that

$$r = S_y' \sin\theta + S_z' \cos\theta \tag{5}$$

The phase velocity v_p for a wave with e polarization and wave normal at an angle ψ to the c axis ($\cos\psi = r$) is given by Born and Wolf[10] as

$$v_p^2 = v_0^2 \cos^2\psi + v_e^2 \sin^2\psi \tag{6}$$

where v_o and v_e are the two principal propagation velocities: $v_o = c/n_o$, and $v_e = c/n_e$. From (6) we can obtain an effective index $n = c/v_p$,

$$n^2 = \frac{{n_e}^2}{1 + r^2[(n_e^2 - {n_0}^2)/{n_0}^2]} \tag{7}$$

The optical path for the e ray, measured in radians, is

$$\Gamma_e = 2\pi t_w n/\lambda S'_{ze} \tag{8}$$

where t_w is the geometrical thickness of the wave plate, and λ the light wavelength in air. The direction cosine S'_{ze} allows for the slight increase in geometrical thickness caused by the inclination of the light beam. It is included here for completeness, but is not a significant correction since S_x, S_y are assumed small

$$S'_{ze} = [1 - (S_x/n_e)^2 - (S_y/n_e)^2]^{1/2} \tag{9}$$

A similar expression can be written for the ordinary ray by substituting n_o for n_e and noting that the ordinary index does not depend on direction

$$\Gamma_o = 2\pi t_w n_o/\lambda S'_{zo} \tag{10}$$

The retardation of the directional wave plate $\Delta\Gamma$ is the difference

$$\Gamma_e - \Gamma_o = \Delta\Gamma = (2\pi t_w/\lambda)(n/S'_{ze} - n_o/S'_{zo}) \tag{11}$$

In principle, the retardation can be calculated from (11) for any direction of incidence, since n depends on S_y through (3), (5), and (7).

Note that if $\Delta\Gamma$ from (11) is expressed as a power series in S_y, the leading term is linear, as follows:

$$\Delta\Gamma = (\text{constant term}) + 2\pi t_w\, \Delta n \sin^2\theta S_y/\lambda n_o + (\text{higher order terms}) \tag{12}$$

where Δn is the birefringence of the material, defined as $n_e - n_o$. We have assumed small birefringence; that is, $\Delta n \ll n_e$. Note that $\Delta\Gamma$ does not depend on S_x; angles in the X direction are not sensed.

The retardation of the compensator can be obtained in a similar way, by taking into account the different orientation of its a, b, c coordinate system. In the result from the preceding analysis for the DWP, the x and y axes must be interchanged and θ set equal to $\pi/2$. The result is

$$\Delta\Gamma_c = (2\pi t_c/\lambda)(n_o/S'_{zo} - n_e/S'_{ze}) \tag{13}$$

The quantity $\Delta\Gamma_c$ does not contain a linear term in either S_x or S_y because the $\cos\theta$ term in (5) vanishes for $\theta = \pi/2$, so that r in (7) becomes $r = S'_z$. Physically, this means that the retardation of the compensator is nearly independent of the propagation direction for small inclinations. We can therefore conclude that the retardation of the DWP and compensator together will vary linearly with S_y, but will be independent of S_x. Accordingly, S_x can be ignored and the behavior of the device described in terms of a light beam traveling in the $Y-Z$ plane. We will specify the direction of the ray in terms of the angle α it forms with Z ($\sin\alpha = S_y$).

In order to achieve the desired on-axis compensation, we require that the total retardation be zero for an axial ray

$$\Delta\Gamma + \Delta\Gamma_c = 0 \qquad \text{for } \alpha = 0 \tag{14}$$

From (11), (13), and (14), and by making the approximation that $\Delta n \ll n_o$, the following condition on the relative thickness of DWP and compensator can be derived

$$t_c/t_w = \sin^2\theta \tag{15}$$

Eq. (15) states that the ratio of the thicknesses of the DWP and compensator must be properly adjusted for exact on-axis compensation. The condition for compensation is wavelength-independent since it does not contain λ or Δn, a fact which permits the device to function in white light.

Up to this point, the analysis has been concerned with the DWP and compensator only. The retardation introduced by the modulator Γ_m must also be included in order to calculate the modulated light intensity as a function of α. We assume a sinusoidal modulator drive at frequency ω, so

$$\Gamma_m = \Gamma_{mo} \sin\omega t \tag{16}$$

The quantity Γ_{mo} is a modulation index given by

$$\Gamma_{mo} = \pi V_p/V_{\lambda/2} \tag{17}$$

where V_p is the peak value (not peak to peak) of the voltage applied to the modulator, and $V_{\lambda/2}$ is the half-wave voltage of the modulator—namely, the voltage that would be required to obtain 100% modulation with it between crossed polaroids. Figure 4 gives Γ_{mo} in terms of V_p and $V_{\lambda/2}$.

The total retardation of the three elements will be

$$\Delta\Gamma_{tot} = \Delta\Gamma + \Delta\Gamma_c + \Delta\Gamma_m \tag{18}$$

Substituting (11) for $\Delta\Gamma$, (13) for $\Delta\Gamma_c$, (16) for $\Delta\Gamma_m$, and making the approximations appropriate for small birefringence and small α that were obtained earlier, we obtain

$$\Delta\Gamma_{tot} = (2\pi t_w/\lambda)(\Delta n\alpha/n_{av})\sin^2\theta + \Gamma_{mo}\sin\omega t \tag{19}$$

The quantity n_{av} is an average index, and can be taken as either n_o or n_e with small error. In deriving the aforementioned expression (the condition for compensation on-axis, (15) has also been used. This condition by its design has eliminated terms in $\Delta\Gamma_{tot}$ not containing α, with the result that $\Delta\Gamma_{tot}$ must equal zero for $\alpha = 0$ and no modulation.

The analyzer is set at 45°, as shown in Fig. 2, and converts the total retardation into an intensity

$$I = I_o \sin^2(\Delta\Gamma_{tot}/2) \tag{20}$$

Here, I_0 is the intensity of the polarized beam incident on the analyzer, and I is the intensity transmitted to the detector. Defining I_0 after the beam has passed through the polarizer means that the 50% loss inherent in polarizing an incoherent beam must be taken into account by including it in the transmission factor for the optics. The transmission must be defined as the fraction of the intensity passed with polarizer

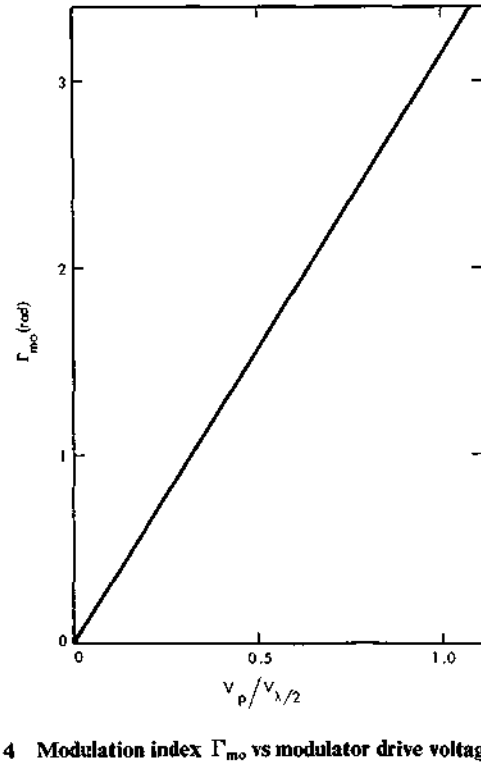

Fig. 4 Modulation index Γ_{mo} vs modulator drive voltage V_p.

and analyzer parallel, instead of crossed for an axial beam $\Delta\Gamma_{tot} = 0$.

Rewriting (20), we obtain

$$I = I_0/2\{1 - \cos[(\pi/2)\alpha/\alpha_{max} - \Gamma_{mo}\sin\omega t]\} \quad (21)$$

where a number of constants have been grouped into an angular scale factor α_{max}

$$\alpha_{max} = \lambda n_{av}/4t_w\,\Delta n\sin^2\theta \quad (22)$$

Thus, α_{max} depends on the wave plate material and thickness. Eq. (21) can be expanded to

$$\frac{I}{I_0} = \frac{1}{2} - \frac{1}{2}\cos\left(\frac{\pi}{2}\frac{\alpha}{\alpha_{max}}\right)J_0(\Gamma_{mo}) - \sin\left(\frac{\pi}{2}\frac{\alpha}{\alpha_{max}}\right)J_1(\Gamma_{mo})\sin\omega t$$
$$- \cos\left(\frac{\pi}{2}\frac{\alpha}{\alpha_{max}}\right)J_2(\Gamma_{mo})\cos 2\omega t + \text{higher harmonics} \quad (23)$$

where J_i are the Bessel functions of order i.

Thus the transmitted intensity has a component at frequency ω which varies as $\sin A\alpha$, where $A = \pi/2\alpha_{max}$, which can be isolated by a phase-sensitive detector using the modulator drive as a reference. If $|\alpha| \gtrsim \frac{3}{4}\alpha$ max, one can operate the quasi-linear part of the sinusoidal curve; but if $\alpha > \alpha$max, the output will decrease again. Accordingly, α_{max} will be considered the useful field of view, and the telescopic optics should be made to accept a field roughly $2\alpha_{max}$ wide—i.e., $-\alpha_{max} < \alpha < \alpha_{max}$. The useful field of view in the X direction, perpendicular to the sensitive axis of the sensor, is not similarly restricted, and could be set many times larger than α_{max} if desired.

Figure 5 is a plot made from Eq. (22) showing the dependence of the useful field of view α_{max} on DWP thickness for three materials of widely differing birefringence: quartz, KDP, and calcite, with $\theta = 45°$.

Figure 6 gives the magnitude of the fundamental component of the transmitted intensity $(I/I_0)^{\omega}$ as a function of α and the parameters α_{max} and Γ_{mo}. This quantity is proportional to the output signal available from the phase detector.

Figure 6 shows that the optimum value of Γ_{mo} is 1.8, corresponding to a V_p of approximately half of $V_{\lambda/2}$. However, the modulator could be operated at 50% of optimum drive ($\Gamma_{mo} = 0.9$) with a signal loss of less than 30%.

As mentioned before, the component of transmitted intensity at 2ω, $(I/I_0)^{2\omega}$, could be detected with a tuned preamplifier and used as an acquisition signal. Figure 7 is a

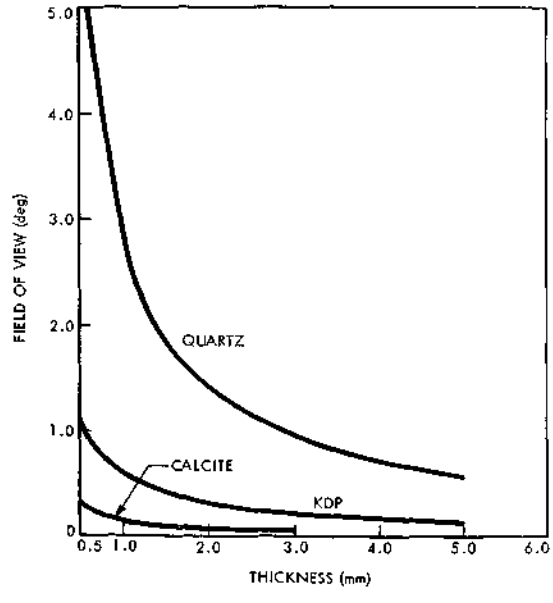

Fig. 5 Field of view as a function of DWP thickness.

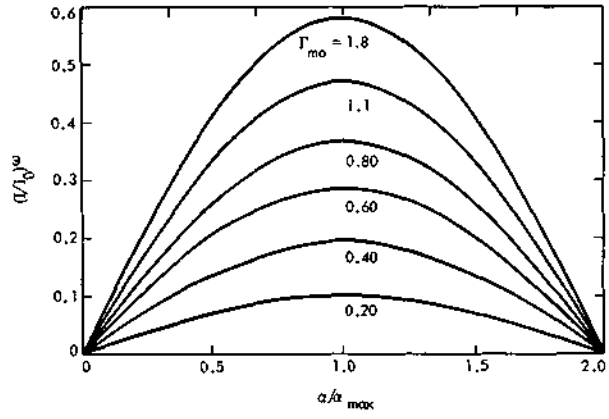

Fig. 6 The component of transmitted intensity at frequency ω as a function of α/α_{max}.

plot showing the magnitude of this signal in terms of Γ_{mo}, α_{max}, and α. The quantity $(I/I_0)^{2\omega}$ is a maximum at $\alpha = 0$ and varies little over the central part of the useful field.

Experimental Verification

The feasibility of the concept has been shown in the laboratory with optical bench hardware and a simulated star. The star image was obtained from a pin hole illuminated by a tungsten ribbon lamp and placed at the focus of a 65-cm focal length collimating lens. The intensity of the source was adjusted with neutral-density filters, while other filters were used to approximate the spectral distribution of a 5500°K blackbody.

The experimental hardware was set up as shown in Fig. 1; however, the elements of the direction-sensitive modulator were spaced out along the axis so that they could be separately mounted for convenience in adjusting their orientation. Since the modulator operates in collimated light over a small field of view, this arrangement presents no optical problems. The limiting aperture of the system was the 1-cm-diam wave plate. A number of DWP-compensator pairs of differing thickness and material were fabricated, but all with $\theta = 45°$, and therefore $t_c = \frac{1}{2}t_w$.

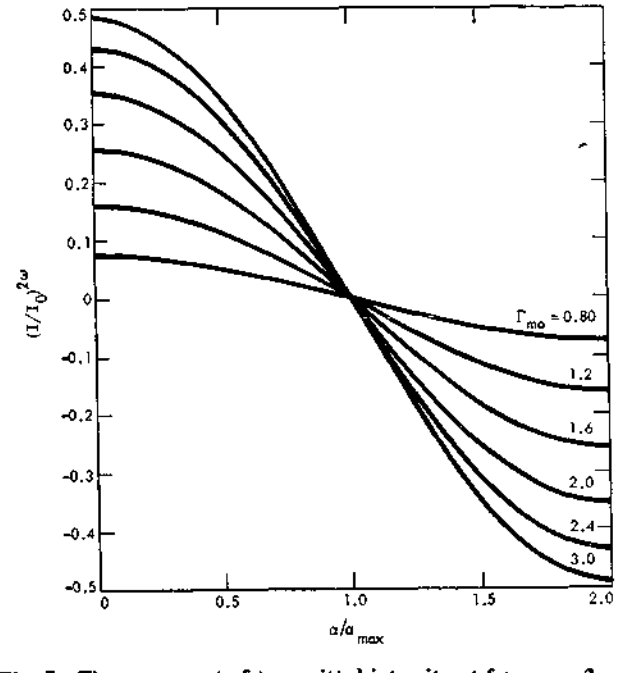

Fig. 7 The component of transmitted intensity at frequency 2ω as a function of α/α_{max}.

The electro-optic modulator was a KD*P (deuterated KDP) wafer 2 mm thick with transparent electrodes (obtained from Crystalab Inc., Rochelle Park, N.J.). Its measured half-wave voltage was 4.4 kv, a value significantly greater than the 3.2 kv expected for KD*P. The reason for the difference is not understood, but may arise from incomplete deuteration.

The polarizer and analyzer were commercial polaroid material (HN-38). The telescope lens was a standard enlarging lens of 100-mm focal length. The detector was an EMI 9536B photomultiplier. No preamplifier was needed, since the phase-sensitive detector was a commercial lock-in amplifier (Princeton Applied Research HR-8).

The magnitude of the photosignal at frequency ω was measured and compared with the $(I/I_0)^\omega$ calculated with the methods of the previous section, using parameters appropriate to the laboratory optics. The DWP for this experiment was of KDP, 2-mm thick with $\theta = 45°$. The modulator was excited with a 500-v peak sinusoidal voltage. The value of I_0, needed in order to find the calculated output, was obtained by turning the analyzer 90° with the simulated star on-axis, and the modulator drive turned off. The d.c. detector signal was then measured to give I_0.

The results are shown in Fig. 8. The nearly linear portion of the output extends roughly to $\alpha = \pm 0.08°$, although a signal indication useful for acquisition would be available out to $\alpha = \pm 0.2°$. The signal at α_{max} is seen to be in close agreement with the calculated value. The calculated α_{max} is somewhat larger than observed, but the difference is reasonable in view of the off-axis birefringence of the modulator, which was neglected in the analysis, and errors in measuring thicknesses.

Figure 9 shows the dependence of signal output on modulator drive voltage at a fixed α for the same experiment. The range of modulator drive voltage shown is low, covering only a portion of the first quarter cycle of $J_1(\Gamma_{mo})$.

Figure 10 is a tracing made with an X-Y plotter, showing data analogous to that in Fig. 8.

This plot was made by scanning the simulated +1 magnitude star at a constant angular rate, while plotting the sensor output as a function of α. The information bandwidth was limited by the lock-in amplifier to a 1-sec time constant, and the aperture was 1 cm in diameter. The figure, showing the observed noise fluctuations, demonstrates that a useful signal-to-noise ratio can be obtained for the bright stars with 1-cm collecting aperture.

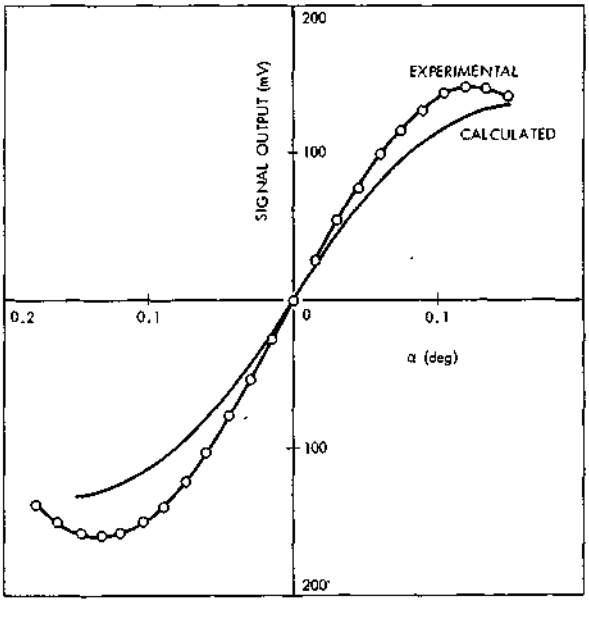

Fig. 8 Experimental sensor output signal compared with the calculated output.

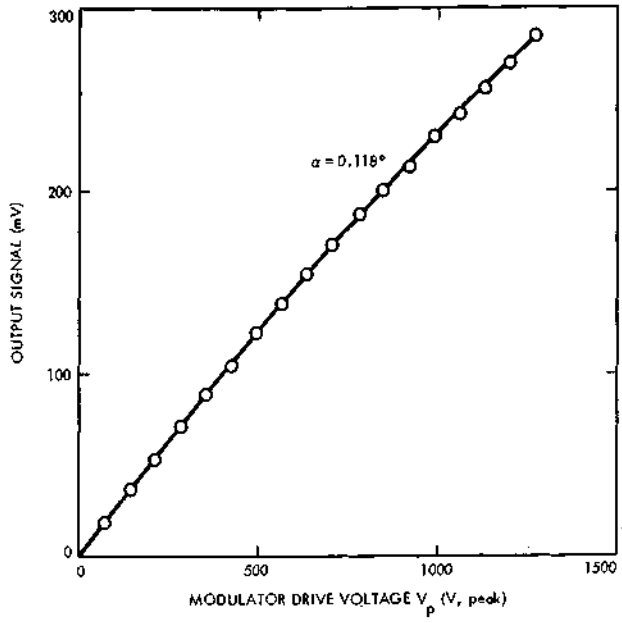

Fig. 9 Experimental sensor output as a function of modulator drive voltage.

Evaluation of the Noise Limitation

The accuracy of pointing toward a dim source, such as a star, is inherently limited by noise, and there is an inverse relationship between pointing accuracy and system-response time. The magnitude of this noise fluctuation is an important constraint in a typical application. An estimate of the equivalent noise input of the present sensor is given below.

There are a number of noise sources, including the noise associated with the electronics, the dark noise from the detector, and the photon noise of the incident light, which is

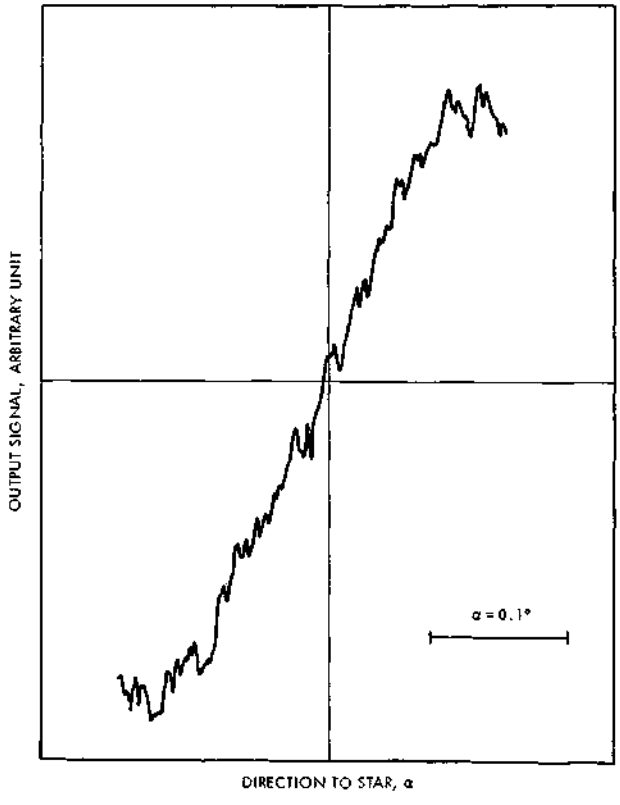

Fig. 10 Experimental output as a function of angle for +1 magnitude star, 1-cm aperture and a photomultiplier detector.

aggravated by the imperfect quantum efficiency of any real detector.

We assume that detector dark noise will dominate, and the following treatment is made in terms of dark noise only. However, for a low-noise photomultiplier, it is possible for photon noise to dominate, requiring modification of the analysis. Our photomultiplier example represents a limiting case, since either reduced dark noise or increased light flux would produce a photon-noise-limited situation.

Let us define a photodetector responsivitity R, a constant which gives the electrical power delivered into the detector load R_L, in terms of the light flux I falling on the detector

$$P = i_{\text{anode}}^2 R_L = (RI)^2 \tag{24}$$

The light flux I_i incident on the sensor optics is

$$I_i = M_v A \tag{25}$$

where M_v = the flux from the star in lumens/cm^2, and A is the area of the collecting aperture.

Assume a transmission T for the optics, so that at the detector the maximum available intensity I_0 (analyzer parallel) will be

$$I_0 = M_v A T \tag{26}$$

The (peak) amplitude of the modulated components of the transmitted intensity of the frequency ω is given in terms of this same I_0 by Eq. (23)

$$I^\omega = I_0 \eta \sin[(\pi/2)\alpha/\alpha_{\max}] \tag{27}$$

The quantity η has been introduced for brevity

$$\eta = J_1(\Gamma_{m0}) \tag{28}$$

The light signal at the detector at ω is then

$$I^\omega = (\pi/2) M_v A T \eta (\alpha/\alpha_{\max}) \tag{29}$$

for α small enough to be on the linear part of the response curve. The rms noise voltage existing at the output of the sensor is calculated from p_n, the noise-effective power of the detector observed under its actual operating conditions and normalized to a 1-Hz bandwidth.

The electrical noise output power of the detector is then

$$P_n = (p_n R)^2 B \tag{30}$$

where B is the signal bandwidth. The noise power at the output of a phase detector is that of the input existing in a band $B = \dfrac{1}{8\tau_1}$, where τ_1 is the time constant of the output circuit of the phase detector, multiplied by the power gain G of the phase detector at its signal frequency[11]

$$P_0^{dc} = G P_{in}^{(\omega)} \tag{31}$$

The P_0^{dc} and P_{in}^{ω} are, respectively, the output and input electrical powers of the phase detector. Therefore, the noise power at the phase-detector output due to detector dark noise of magnitude p_n would be

$$N = (p_n R)^2 \frac{G}{8\tau_1} \tag{32}$$

The signal power at the phase-detector output is obtained from (24), (29), and (31)

$$S = [(\pi/2)\eta M_v A T R\, \alpha/\alpha_{\max}]^2 G \tag{33}$$

From (32) and (33) an equivalent noise fluctuation $\langle\alpha\rangle_n$ of the input angle α can be obtained

$$\langle\alpha\rangle_n/\alpha_{\max} = 2p_n/\pi\sqrt{8\tau_1}\,\eta M_v A T \tag{34}$$

The time constant τ_1 is the time constant of the filter in the output circuit of the phase detector. However, a sensor such as this would normally be used as the error sensor in a control loop, and the response time of the closed loop would be expected to be slower than that of the sensor itself. The slower response of the loop averages the noise, and it can be shown that the fluctuation in the closed-loop pointing angle caused by sensor noise is given by the same expression, Eq. (33), with τ_1 replaced by the loop response time. Note that the result calculated from (34) is an rms noise

$$\langle\alpha\rangle_n = (\langle\alpha(t)^2 - \langle\alpha\rangle^2\rangle)^{1/2} \tag{35}$$

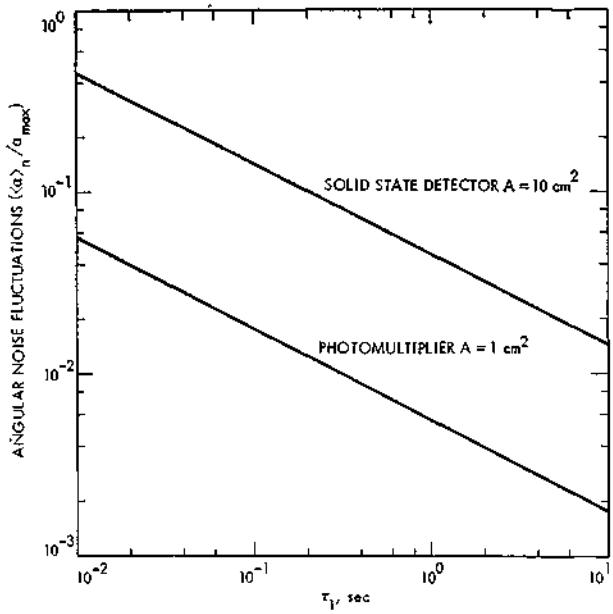

Fig. 11 Calculated noise as a function of response time. Parameters used in the calculation are given in Table 1.

Numerical results are plotted in Fig. 11 for two cases: a photomultiplier detector and a silicon solid-state detector. The significant parameters are given in Table 1. The noise expected for different values of A, p_n, and M_v can easily be obtained by referring to Eq. (34).

The magnitude of the noise observed experimentally and expressed as an equivalent input angular fluctuation was estimated using data of which Fig. 10 represents a sample. The peak-to-peak voltage signal-to-noise ratio observed is approximately 16. The entrance aperture was 1 cm in diameter, the simulated star was +1 magnitude and a 1-sec time constant was used. If the peak-to-peak noise is converted somewhat arbitrarily to rms by dividing it by 3, and appropriate adjustments are made for M_v and A in order to compare it with Fig. 11, an experimental $\langle\alpha\rangle_n/\alpha_{\max} = 0.005$

Table 1 Parameters used in calculating the equivalent noise input of the sensor shown in Fig. 11

Parameter	Photomultiplier detector	Silicon detector
Detector NEP, p_n	4×10^{-13} lumen $Hz^{-1/2}$ (appropriate for 1P21 or 9536B)	3×10^{-11} lumen $Hz^{-1/2}$ (appropriate for HP-4204)
Area of objective A	1 cm^2	10 cm^2
Modulator drive parameter η	0.4	0.4
Transmission of optics T	0.3 (ideal polarizer +60% transmission for remaining optics)	0.3
Incident flux M_v	2×10^{-10} lumen/cm^2 (0 magnitude star)	2×10^{-10} lumen/cm^2

can be estimated. This value falls very close to the photomultiplier curve in Fig. 11, thus confirming the validity of the theoretical noise estimate.

In order to place this calculation in perspective, the equivalent noise input can be estimated for a hypothetical ideal sensor in which the incident energy is partitioned between two photocathodes as a linear function of angle. Only the noise inherently associated with photoemission is considered, the rest of the system being assumed noiseless. The result, taking an incident flux of 2×10^{-10} lumen and a 70 μA/lumen cathode efficiency in order to be comparable to the photomultiplier curve in Fig. 11, would fall a factor of $3\frac{1}{2}$ below it. Thus, the noise of the actual sensor is a factor of $3\frac{1}{2}$ larger than the limit theoretically attainable with a photomultiplier. This factor can be regarded as a measure of the efficiency of the modulation technique employed in the sensor.

Discussion

So far, pointing error and drift have not been treated. A detailed evaluation of this type of error source remains to be done, but we have observed in the laboratory that the null remains stable over a period of several days, at least within the readability of the instrumentation, which was roughly 1% of the angular range α_{max}.

One possible error source whose size can be estimated analytically is the effect of temperature changes on the wave plates. Temperature change to the modulator element does not affect the null. The refractive index and birefringence of all materials depend slightly on temperature, a dependence that will result in a small change in the retardation of each plate. No effect on the null position is expected from simultaneous change in the temperature of both DWP and compensator. A temperature difference between the two elements will cause a shift, however. The magnitude of this shift can be estimated for a pair of quartz plates because the temperature coefficient of the refractive indices is available.[12] The result is $d(\alpha/\alpha_{max})/dT \approx 10^{-5}$/°C, which does not appear to be a serious problem.

The most significant error source is likely to be the presence of unwanted light sources, such as a field of very dim stars or a lighted background within the sensitive field of view, in addition to the desired star or beacon. The concept assumes that there is only one point source present in the sensitive field of view; if there are more than one, their inputs will be averaged. The laboratory model was found to be very insensitive to scattered light—i.e., to light scattered into the detector from sources outside the field defined by the telescope.

A practical constraint on the sensor field of view, as opposed to a null drift, arises from off-axis retardation of the modulator. KD*P appears to be the best choice of material because of its availability in reasonably large size with good optical quality. The modulator crystal is operated with its optic axis along Z in Fig. 2. Therefore, off-axis rays suffer retardation, and distortion of the idealized sensor output occurs. In principle, it would be possible to take into account the effect of the modulator crystal in calculating the sensor output as a function in both X and Y directions. As an example, the null line ($\Delta\Gamma_{tot} = 0$) might be mapped out in two dimensions. Although straightforward, the calculation is complex and would have to be done numerically on a computer.

An angular field of view is often quoted for a KDP-type modulator and typically may be of the order of $\frac{1}{2}$–2°, depending on thickness. This angle is not always defined in the same manner, but one such definition sets the field of view at the angle where the static retardation of the crystal causes a 1% light leak between crossed polaroids. If $\sin^2(\Gamma/2) \approx 0.01$, then $\Gamma \approx 0.2$. The equality $\alpha = \alpha_{max}$ occurs at $\Gamma_{tot} = \pi/2 \approx 1.6$. Therefore, operation within the modulator angular field would result in a maximum distortion of the sensor response of about 12%. The distortion is constant, fixed in time. A reasonable limit on the sensor range is therefore set by the 1% modulator field of view for a KDP-type modulator. A considerably larger field could be available for acquisition, as mentioned before.

In summary, feasibility has been demonstrated for a new type of star tracker which relies on crystalline anisotropy in an oriented waveplate for its ability to sense direction. Its efficiency is such that useful performance can be obtained on the brighter stars with optics of 1–10 cm aperture. It has the advantages of simplicity and no moving parts, and the photodetector operates in an a.c. mode. A specific configuration has been analyzed and tested in the laboratory; however, further detailed work remains to be done in order to fully evaluate its characteristics and limitations.

Possible applications of the new sensor include spacecraft attitude control using a star reference, and pointing of a platform or other gimbaled instrument toward either a natural source or an artificial beacon. The source can be white light. By modifying the signal processing somewhat, the device can also be configured to sense a horizon—i.e., the edge of a lighted area—instead of a point source.

References

[1] Hatcher, N. M., "Spacecraft Attitude Sensors—Where We Stand Today," *Astronautics and Aeronautics*, Vol. 4, No. 12, Dec. 1966, pp. 58–67.

[2] *Celestial Tracker Issue, IEEE Transactions on Aerospace and Navigational Electronics*, Vol. 10, No. 3, 1963.

[3] *Spacecraft Star Trackers*, NASA SP 8026, July 1970.

[4] Koso, D. A. and Kolladge, J. C., "Solar Attitude Reference Sensors," *Proceedings of the Symposium on Spacecraft Attitude Determination*," Rept. TR-0066-(5306)-12, Vol. 1, Oct. 1969, Aerospace Corp., El Segundo, Calif., p. 155.

[5] Astheimer, R. W., "Instrumentation for Infrared Horizon Sensing," *Proceedings of the Symposium on Spacecraft Attitude Determination*," Rept. TR-0066-(5306)-12, Vol. 1, Oct. 1969, Aerospace Corp., El Segundo, Calif., p. 169.

[6] Lansing, J. C., Jr., "Calibration and Spaceborne Performance of the Surveyor Spacecraft Star Sensor," *Journal of Spacecraft and Rockets*, Vol. 5, No. 1, Jan. 1968, pp. 84–89.

[7] Birnbaum, M. M. and Salomon, P. M., "Strapdown Star Tracker for Space Vehicle Attitude Control," *Journal of Spacecraft and Rockets*, Vol. 5, No. 10, Oct. 1968, pp. 1188–1192.

[8] Goss, W. C., "The Mariner Spacecraft Star Sensors," *Applied Optics*, Vol. 9, No. 5, May 1970, pp. 1056–1067.

[9] Wood, E. A., *Crystals and Light*, Van Nostrand, New York, 1964.

[10] Born, M. and Wolf, E., *Principles of Optics*, Pergamon Press, New York, 1959.

[11] van der Ziel, A., *Noise*, Prentice-Hall, N.J., 1954.

[12] *American Institute of Physics Handbook*, 2nd ed., McGraw-Hill, New York, 1963.

NOISE IN THE ELECTRO-OPTIC DIRECTION SENSOR*

Alan R. Johnston

JET PROPULSION LABORATORY
CALIFORNIA INSTITUTE OF TECHNOLOGY
PASADENA, CALIFORNIA

October 5, 1971

100

1. INTRODUCTION

The purpose of this paper is to evaluate equivalent noise input fluctuations in a new type of sensor called an "Electro-optic Direction Sensor" (EODS). The direction sensor itself utilizes a pair of anisotropic or crystalline wave plates to derive information about the direction to a distant light source. The basic concepts of the sensor are first briefly explained in order to provide a background from which to discuss the noise problem. In order to further put the results in perspective, the noise equivalent input expected in an ideal star tracker is also calculated, first assuming basic or photon noise only, and again accounting for a detector cathode efficiency. These results represent an optimum noise performance against which the real sensor may be compared. Finally, both calculated and experimental equivalent noise inputs are presented for the EODS device. We assume that the dominant noise source is the detector, and that no other significant sources exist. This assumption can be a valid one with careful technique.

2. DESCRIPTION OF THE SENSOR (Ref. 1)

The Electro-Optic Direction Sensor generates an electrical error signal useful for attitude control or pointing from a distant light source. It is a single axis device suitable for roll axis attitude control, or two could be combined for a more general pointing application. The reference light source may be white light, such as a star, or a laser beacon. Although several techniques presently exist for star tracking, EODS has potential advantages, being simple, compact, having no moving parts and using an ordinary intensity detector rather than an x-y device.

The sensor optics can be divided into two main parts, as shown in Fig. 1, a sandwich of birefringent optics, called the direction-sensitive modulator (DSM), and a set of conventional telescopic optics which collects the light and directs it onto a detector. The function of the telescope is straightforward and will not be discussed further.

The DSM consists of five elements, oriented as shown in Fig. 2. The directional wave plate is made of a crystalline material, such as quartz, calcite, or KDP, (KH_2PO_4) such that the optic axis is at an angle θ from the normal to the plane of the plate. It exhibits a retardation (optical phase shift) dependent on the direction light passes through it, and is the element from which the directional information is derived.

The compensator is a matched wave plate of the same material, with optic axis in the plane of the wafer, permitting operation in white light. The modulator superimposes a sinusoidally varying component of retardation at frequency ω. Taken as a whole, the DSM is a filter in which transmission depends on direction proportional to $\sin^2\alpha$. The modulator oscillates, or wobbles the transmission function in the angle α, thus producing modulation of the photosignal depending in amplitude and sign on the angular position of the light source with respect to a minimum of the transmission function mentioned above.

---

*This paper presents the results of one phase of research carried out at the Jet Propulsion Laboratory, California Institute of Technology, under Contract No. NAS 7-100, sponsored by the National Aeronautics and Space Administration.

The photosignal actually contains all harmonics of the frequency ω. It is the component at ω that is proportional to the angle α, and a dc slowly varying signal is obtained by phase detection. The electronics are as shown in Fig. 3. The signal at 2ω has a broad maximum near null, and thus is available for an acquisition signal. Modification of the signal processing would make possible an alternative mode of operation as a horizon or planet limb sensor.

The analysis of the sensor operation will not be repeated here in detail (see ref. 1). It can be shown that the output signal, V_0 is given by

$$V_0 = I_0 \eta T R G^{1/2} \sin\left(\frac{\pi}{2} \frac{\alpha}{\alpha_{max}}\right) \qquad (1)$$

where

η = a dimensionless factor depending on the modulator drive level typically η may be 0.3 to 0.4

I_0 = collected light flux

T = transmission of the optics
$T \leq 0.5$ for natural light because of the polarizer

R = detector responsivity

G = power gain of phase sensitive detector

α = angle being sensed

α_{max} = the nominal field-of-view, center to edge.
α_{max} is determined by wave plate material and geometry.

The useful angular range includes most of the first quarter cycle of the sine function. The output is linear within 20% out to $\sim 0.7\,\alpha_{max}$, which may be somewhat arbitrarily taken to be the linear range, within which normal operation the device occurs after an acquisition is completed. A geometrical field-of-view somewhat smaller than $-2\alpha_{max} < \alpha < 2_{\alpha max}$ is available for acquisition.

In the following discussion of noise, α_{max}, the point at which output is maximum, is taken to be the angular range of the device for convenience. It should be remembered that the linear range is somewhat smaller and the range available for acquisition somewhat larger than α_{max}.

Feasibility of the concept has been shown in the laboratory, and the experimental results agree satisfactorily with the theoretical characteristics.

A theoretical estimate of the noise equivalent input angle was also made and compared with a preliminary experimental signal-to-noise obtained with a photomultiplier detector. The theoretical noise equivalent input angle was calculated in terms of the field-of-view α_{max} using equation (1) above for the signal output, and the nep (dark noise) of the detector P_n. The detector noise was traced through the phase detector using a result due to Van der Ziel (Ref. 2) that the output noise power of a phase detector is that existing at the input in a band 8τ, multiplied by the power gain. Here, τ represents the phase detector output time constant.

3. NOISE IN AN IDEAL DIRECTION SENSOR

In this section we describe a model of an idealized sensor and calculate its equivalent noise input angle for later comparison with the EODS.

The model can be described with the aid of Fig. 4. A distant point source is assumed, at an angle α from the axis. The total light flux collected is designated by I_0. The optics are assumed to divide the incoming radiation I_0 between two detectors D_1 and D_2 without loss, such that the proportion falling on D_1 varies linearly with α over a specified angular range; $\alpha_{max} \leq \alpha \leq \alpha_{max}$. Since there is no loss, $I_0 = I_1 + I_2$. The detailed nature of the optics necessary to accomplish this is unimportant. At the limits of the linear range $\pm \alpha_{max}$, all of the energy passing the entrance aperture falls on one of the detectors. The electrical signal from the two detectors is amplified by a noiseless differential amplifier, G resulting in an output signal V_0 where

$$V_0 = A(I_1 - I_2) \tag{2}$$

where A is an arbitrary gain factor. Introducing the linear dependence on α,

$$V_0 = \frac{A\alpha I_0}{\alpha_{max}} \tag{3}$$

The output as given by equation (3) is shown graphically in Fig. 5, which also indicates the relationship between the output noise voltage V_n and the equivalent input angle noise α_n.

Consider first the ideal case where the only noise is photon noise; the detectors are thus noiseless. The noise fluctuation can be estimated by the statistics associated with photon counting, which says that if N photons are being counted, on the average; the rms fluctuation in the count δN, is given by

$$\delta N = \sqrt{N} \tag{4}$$

Designating the counting period by τ_0, the number of photons N_1 received on D_1 during an interval τ can be expressed in terms of the received flux I_1.

$$N_1 = \frac{I_1 \tau_0}{\epsilon h\nu} \tag{5}$$

ϵ = an effective photometric efficiency to convert from radiometric to photometric units. ϵ depends on the spectral distribution of the light.

$h\nu$ = the energy transmitted by one photon.

The noise component of the output voltage can now be calculated using (2) - (5),

$$V_n = A\left(\frac{I_0 \epsilon h\nu}{\tau_0}\right)^{1/2} \tag{6}$$

Converting this noise voltage to a signal to noise ratio, expressed in terms of α_{max} we obtain the following result.

$$\alpha_n/\alpha_{max} = \left(\frac{\epsilon h\nu}{I_0 \tau_0}\right)^{1/2} \tag{7}$$

Thus the signal-noise ratio depends on both the input light flux and the sampling time. The characteristic tradeoff between noise level and response time is indicated by the factor $\tau^{-1/2}$.

If a more sophisticated analysis is used, in which a low-pass filter with time constant τ is placed at the amplifier output to define the sensor response time, the above result is modified to:

$$\alpha_n/\alpha_{max} = \left(\frac{\epsilon h\nu}{2I_0 \tau}\right)^{1/2} \tag{8}$$

The response time of the sensor τ is, as seems reasonable, half the sampling period τ_0. The result 8 is plotted in Fig. 6 as a function of I_0.

A more realistic (and less favorable) estimate of optimum noise performance would result if the quantum efficiency of the detector is taken into account. No near perfect quantum counting detectors exist, but the performance

of a real photomultiplier can be approximated very closely by the introduction of a cathode quantum efficiency. The noise added by the electron multiplication process is small.

The same analysis suffices, except that now photoelectrons are counted instead of photons. Equation 5 becomes

$$N_{e1} = \frac{I_1 q \tau}{\epsilon h \nu} \tag{9}$$

where

q = cathode quantum efficiency or

$$N_e = \frac{I \xi_c \tau}{e} \tag{10}$$

where ξ_c is the cathode luminous efficiency usually given in A/lumen. e is the electronic charge. The original noise ratio α_n/α_{max} is multiplied by $q^{-1/2}$, or if we use (10), we obtain:

$$\alpha_n/\alpha_{max} = \left(\frac{e}{\xi_c I_0 \tau}\right)^{1/2} \tag{11}$$

Equation 11 is also plotted in Fig. 6, and represents an optimum sensor noise input after allowing for the detector cathode efficiency.

Although the foregoing discussion has been made in terms of a conceptual model, it should be remembered that the specifics of the model are not important, and that the result can apply to several possible mechanizations. For example, the process of proportioning the collected light onto two detectors could be done by a nutating mirror and aperture combination, or by a biprism which splits the light in a telescopic image of a star according to its position.

Diffraction effects have been ignored, but if the optical geometry should be such that it is important, diffraction spreading must be taken into account in determining the proportioning range α_{max}; otherwise the reasoning would not be affected.

It should also be noted that the time constant τ can be interpreted in two ways. As discussed here it is the response time of the sensor output itself to a step change in the input angle. However, in almost any application, the sensor would be placed in a control loop to point or orient a large mass, and the control loop time constant would be much larger than the sensor time constant. In this situation it can be shown that the sensor noise is attenuated by the loop dynamics, with the result that τ can be interpreted as the loop response time constant, and α_n as the rms noise fluctuation in the orientation of the controlled mass.

4. NOISE IN THE ELECTRO-OPTIC DIRECTION SENSOR

a) General

We will now give a general expression for the equivalent noise input of the EODS, based on our earlier derivation. Measured noise obtained from the sensor using both a photomultiplier (EMI 9536B) and a Si Pin diode (HP 4207) will then be compared with the theory, confirming its value as a tool for estimating equivalent noise input. Finally, curves have been generated from the general noise expression, and are shown in Fig. 6 along with the ideal sensor case.

The normalized equivalent noise input of the EODS was calculated in Reference 1, assuming a given detector noise effective power. We wish to modify the result in order to take into account the shot noise component of the photocurrent. If the photocurrent is i_c, then the shot noise component δi_c per unit band width associated with it is

$$\delta i_c = \sqrt{2ei_c} \tag{12}$$

Again taking the detection efficiency to be ξ_c, we can convert to an equivalent fluctuation in light flux, δI_c,

$$\delta I_c = \frac{\delta i}{\xi_c} = \left(\frac{2eI_0}{\xi_c}\right)^{1/2} \tag{13}$$

which is then added to the dark noise contribution. The resulting normalized sensor noise is:

$$\alpha_n/\alpha_{max} = \frac{2\left(P_n^2 + \frac{2eI_0}{\xi_c}\right)^{1/2}}{\pi\eta I_0 T(8\tau)^{1/2}}$$

where the parameters are defined as follows

P_n = effective dark noise input of the detector, including preamplifier noise, per unit bandwidth

ξ_c = detection efficiency

η = modulation efficiency parameter

T = transmission of optics

τ_1 = time constant of phase detector output

I_0 = flux accepted by entrance aperture

A laboratory sensor was constructed for the experimental work using optical bench hardware. The significant facts about the apparatus are as follows:

The collecting aperture was 1.0 cm in diameter, the wave plates were of KDP, 2 mm thick for the DWP and 1 mm for the compensator. The modulator was of KD*P (potassium dideuterium phosphate) with transparent electrodes having a half wave voltage of 4.4 kV. The modulator drive was set at 1.0 kV rms, resulting in $\eta = 0.45$. Polarizer and analyzer were of HN-38. The source was a simulated star from a collimator incorporating a ribbon filament tungsten lamp filtered to a color temperature of approximately 5500°K. The filters used for adjustment of the spectrol distribution were two KG1 and one BG 38 (Ref. 3).

The sensor output, taken from the PAR HR-8 (Ref. 4) used for the phase detector was recorded in real time with the source set at the sensor null. The noise level was determined by hand calculating the rms fluctuation of the recorded signal. The quantity α_{max} was calculated from the full scale hard-over signal output as recorded on the same recorder on an appropriately compressed scale.

b) Photomultiplier Detector

The photomultiplier detector was operated at its maximum recommended gain, into a 1 MΩ load. No optical constraints enter, because of the large area photocathode. The applicable parameters were as follows:

Input flux (τ variable)	$I_0 = 1 \times 10^{-10}$	lumen
Time constant (I_0 variable)	$\tau = 0.3$	sec
Cathode efficiency	$\xi_c = 70$	μA/l

Dark nep	$\rho_n = 4 \times 10^{-13}$	lumen
Modulation efficiency	$\eta = 0.45$	
Optical Transmission	$T = 0.3$	

The experimental data are plotted in Fig. 7. The solid lines in the figure are derived from Eq. (14) using the above parameters. None of the parameters were made adjustable for best fit. Cathode efficiency and dark nep are from the manufacturer's literature, while the others were independently determined. The agreement is good. The data indicates that dark noise begins to dominate at $\sim 10^{-10}$ ℓm rather than 3×10^{-11} ℓm, thus the actual total dark noise was slightly larger than predicted. The functional form of the measured noise agrees with theory.

Application of a photomultiplier in EODS appears to be straightforward and the resulting noise characteristics are well explained in terms of the simple theory given by Eq. (14).

c. Silicon P.I.N Photodiode

Analogous data were obtained with a HP 4207 photodiode. The relevant experimental parameters are as follows.

Input flux (τ variable)	10^{-8}
Time constant (I_0 variable)	0.3 sec
Detector nep (calculated at 0.55μ)	5×10^{-11}
Modulation efficiency	0.45
Transmission of optics	0.3

Careful attention must be given to the diode mounting, both optically and electrically. The sensitive area of our detector was 1 mm in diameter, necessitating a well matched field lens in order to direct all the light into the detector from any position in the field of view. An 8 mm f.l. microscope objective was used. In addition, the load resistor, at the preamplifier input must be $10^8\Omega$ or larger in order to reach the inherent noise limit of the detector itself. The overall nep including a contribution from the amplifier would be dominated by the input resistor noise at smaller resistance values. We did not utilize a specially designed preamplifier, but rather mounted the detector directly to the 100 MΩ input of a Type D preamp for a PAR HR-8 phase resistive detector. This arrangement did not prove to be optimum; amplifier thermal noise still dominates. However, the improvement in sensor noise that could be obtained with an optimum circuit is felt to be roughly a factor of two.

The data are given on Fig. 8 along with the theoretical noise input. The solid lines were calculated using the numerical values given above.

The detector nep was derived from manufacturer's data, converted to luminous units at 0.55μ. Monochromatic light was assumed, but the result would be reasonably accurate if most of the incident energy lies between 0.5μ and 0.6μ. If the light is from a cool, red source, an adjustment would be needed to allow for the extended red sensitivity of a silicon detector.

The measured noise is somewhat larger than the theoretical result, but difference is not felt to be significant in view of the experimental uncertainty expected in this type of measurement. The functional form of the data is again correct. The actual detector noise is felt to be smaller than the calculated value, because of the spectral distribution of the source, but excess noise from the preamp, input resistor thermal noise and a lower than expected transmission factor all combine to raise the final noise level.

The same measurements were repeated with an EGG SGD-040 silicon PIN diode. The observed noise was much higher and the results are not given here. The reason was not high detector noise, but rather low responsitivity. The abnormally low response is not understood at present.

5. CONCLUSIONS

In this paper, we have characterized the limitations that are expected in the EODS due to noise from two points of view. First, the basic noise in a simple form of ideal detector was calculated in order to provide a reference point from which to judge the EODS concept. Secondly, the equivalent noise input of an experimental sensor was measured in the laboratory and compared with theory.

We find the EODS to be noiser by a factor of 3.5 than optimum, the difference being due to the transmission loss associated with a polarizer, and the inherent efficiency of the EODS modulation scheme. When used with a photomultiplier the EODS noise input is well understood. The brightest stars can be easily reached with a 1 cm^2 aperture, but substantial improvement over the presently observed noise input is not likely.

The situation for a solid state detector is somewhat different because the detector dark noise is by far the dominant source, completely overwhelming the basic photon noise component. As is well-known, state-of-the-art design of the preamplifier-detector interface is required for threshold signal operation with a solid state detector. In addition, the experimentally observed noise level was larger by a factor of 3 than can be accounted for on the basis of published detector dark noise, modified to 0.55μ, the visual peak. However, the results indicate that our theoretical estimate of sensor input noise is valid, and is adequate to estimate the sensor noise provided the detector noise is known correctly for the specific configuration being considered.

It is felt that the curve shown in Fig. 6 represents a reasonable expectation of what can be achieved with a silicon detector.

A 0 mag white star could be followed with a collecting aperture of approximately 10 cm^2 (4 cm diam.) or larger. It thus appears that the very desirable simplicity and compactness of the solid state detector can be taken advantage of at the cost of a larger lens aperture, and that in any specific application a trade-off could be made to determine the best approach.

Captions:

1. A pictorial diagram of the sensor.

2. Diagram showing orientation of the elements of the Direction Sensitive Modulator.

3. Electronic block diagram of the sensor.

4. Functional diagram of a hypothetical ideal sensor used to estimate basic noise limitations.

5. Transfer characteristic of the ideal sensor.

6. Normalized noise α_n/α_{max} for both an ideal sensor and EODS, plotted as a function of collected light flux.

7. A comparison of the experimental noise equivalent input with theory, using a photomultiplier detector. Circles indicate data vs time constant, while crosses are vs flux.

8. A comparison of experimental and theoretical noise for a HP-4207 Si PIN photodiode. Circles are vs τ, crosses vs I_0.

References:

1. This section is a resume of an earlier paper describing the EODS in more detail: A. R. Johnston, "An Electro-optic Direction Sensor", AIAA Guidance, Control and Flight Dynamics Conference, Hempstead, New York, August 1971, Paper No. 71-966.

2. A. Van der Ziel, Noise, Prentice-Hall, New York, 1954.

3. Schott filters obtained from Fish Schurman Co., New Rochelle, New York.

4. Obtained from Princeton Applied Research Corp., Princeton, New Jersey.

111

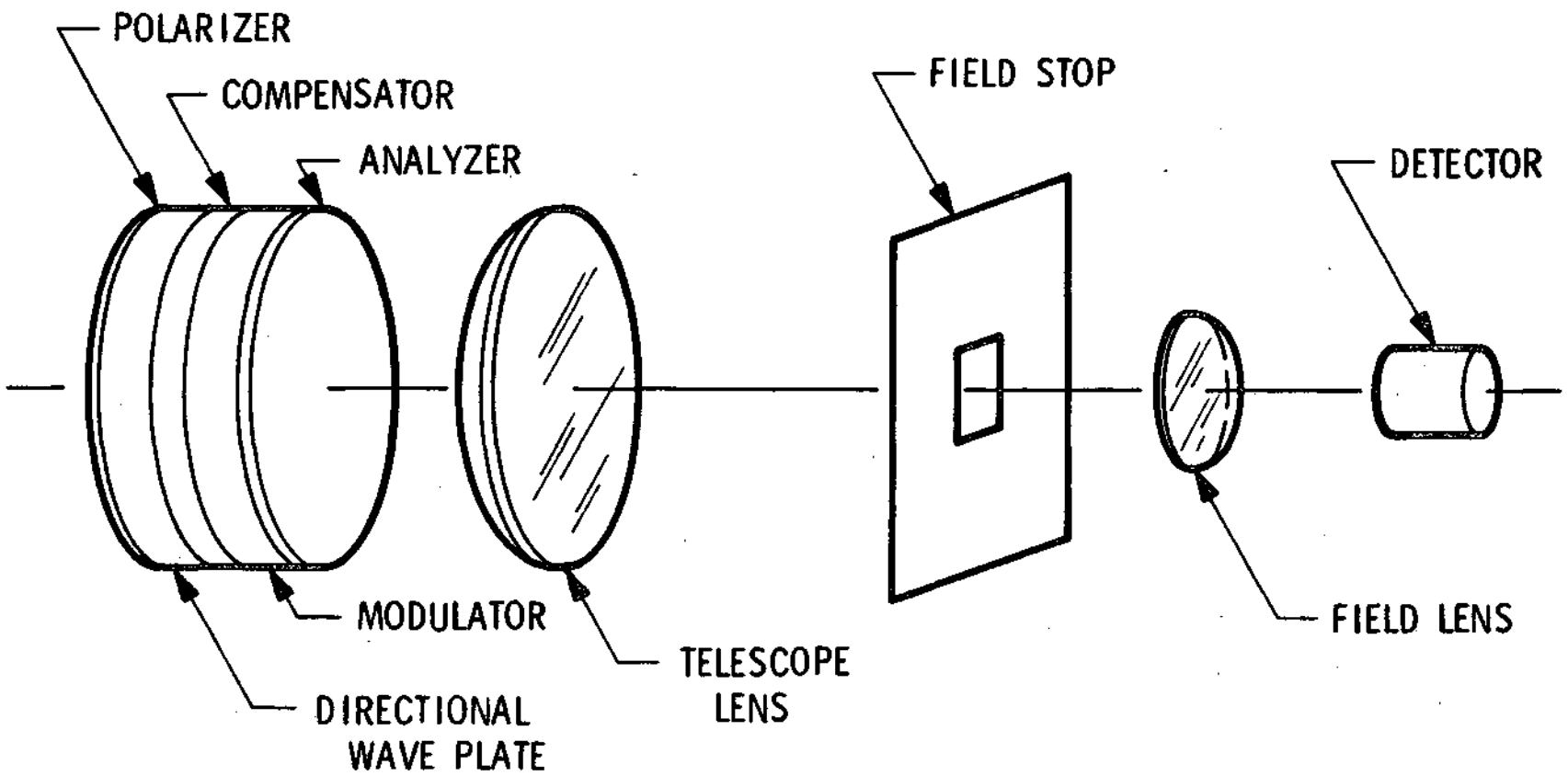
POLARIZER
COMPENSATOR
ANALYZER
FIELD STOP
DETECTOR
MODULATOR
TELESCOPE LENS
FIELD LENS
DIRECTIONAL WAVE PLATE

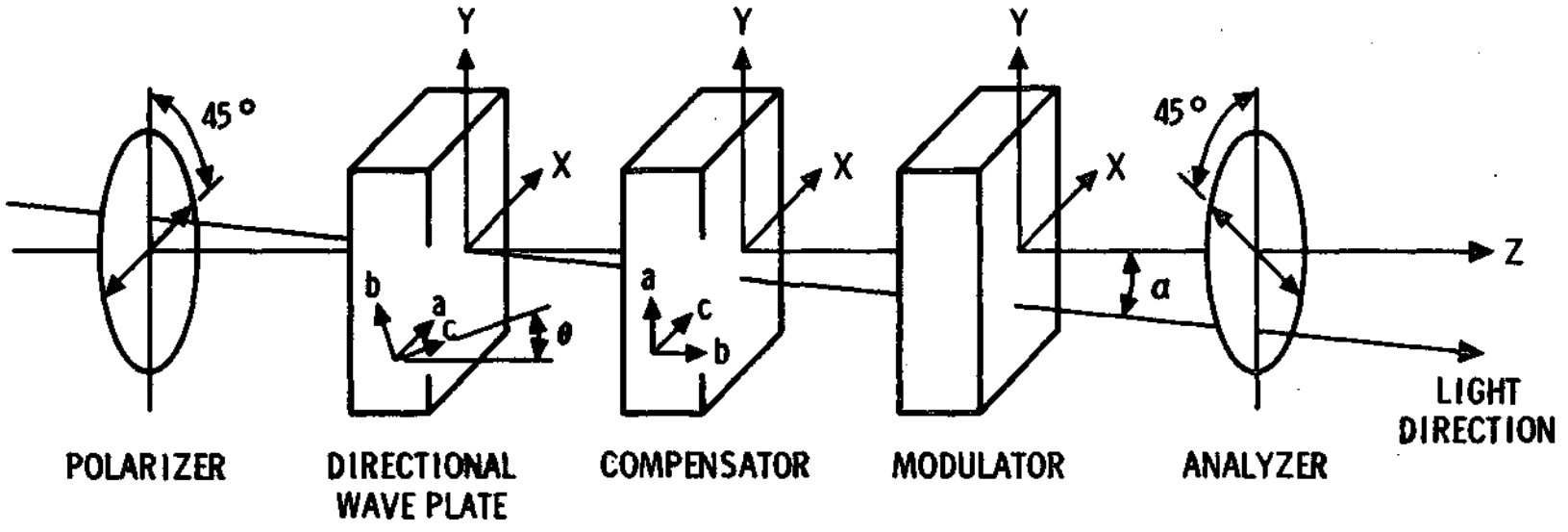
Y
Y
Y
45°
45°
X
X
X
b
a
c
θ
a
c
b
Z
a
LIGHT
DIRECTION
POLARIZER
DIRECTIONAL
WAVE PLATE
COMPENSATOR
MODULATOR
ANALYZER

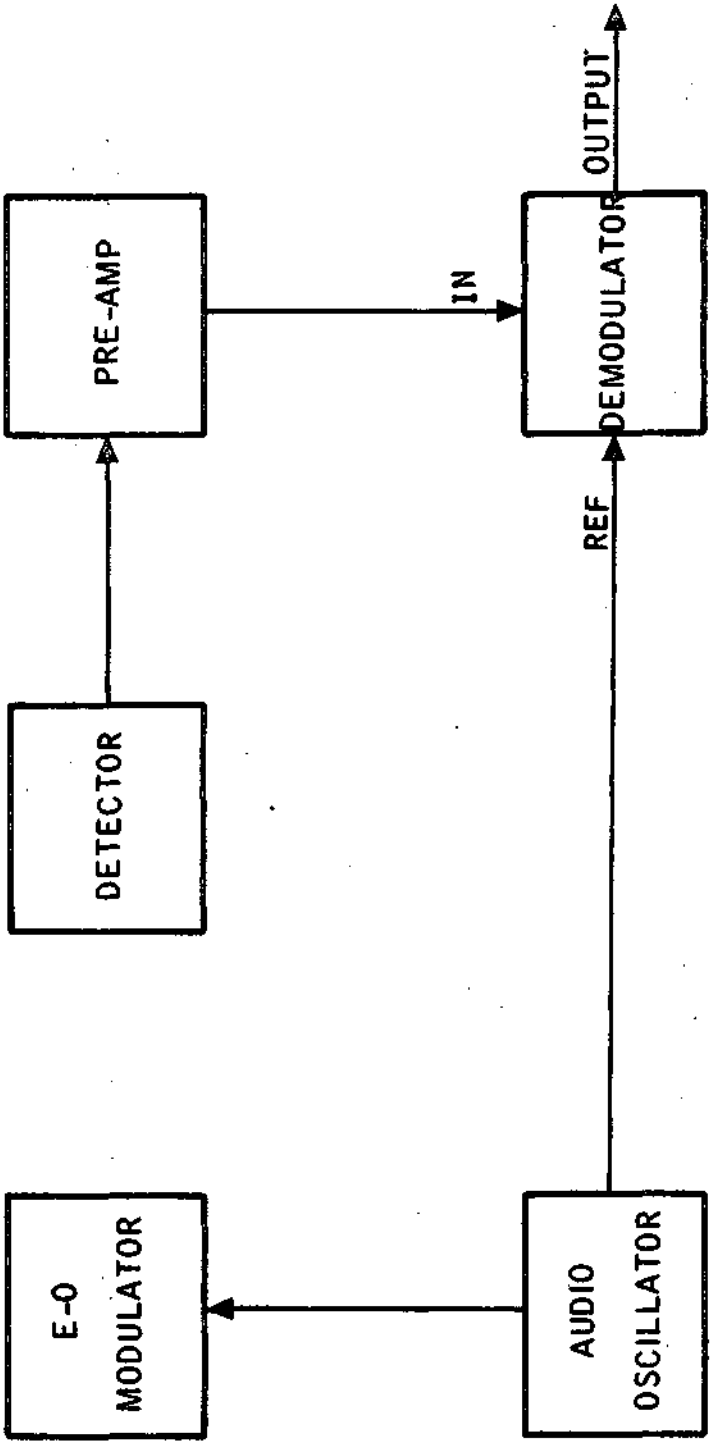

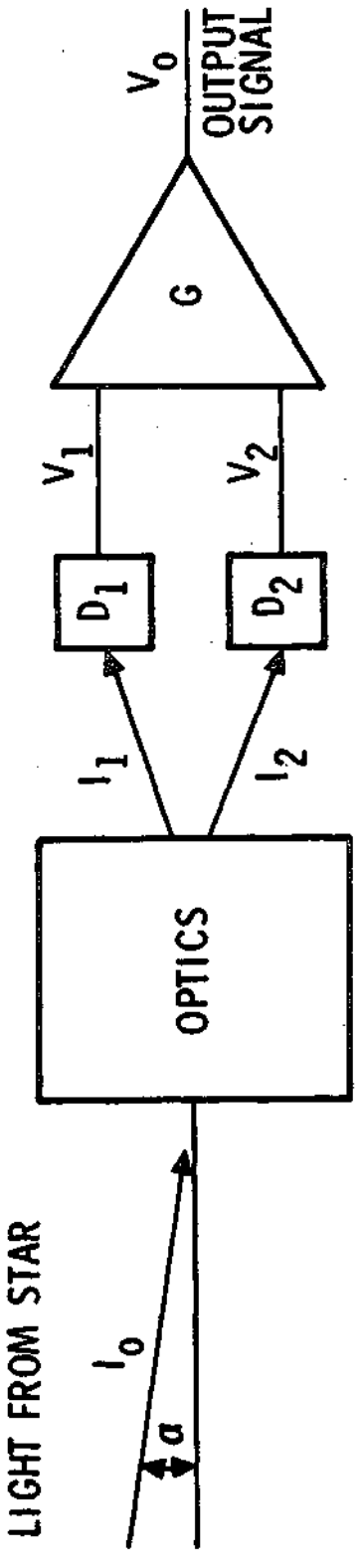
LIGHT FROM STAR
I_0
α
OPTICS
I_1
I_2
D_1
D_2
V_1
V_2
G
V_0
OUTPUT SIGNAL

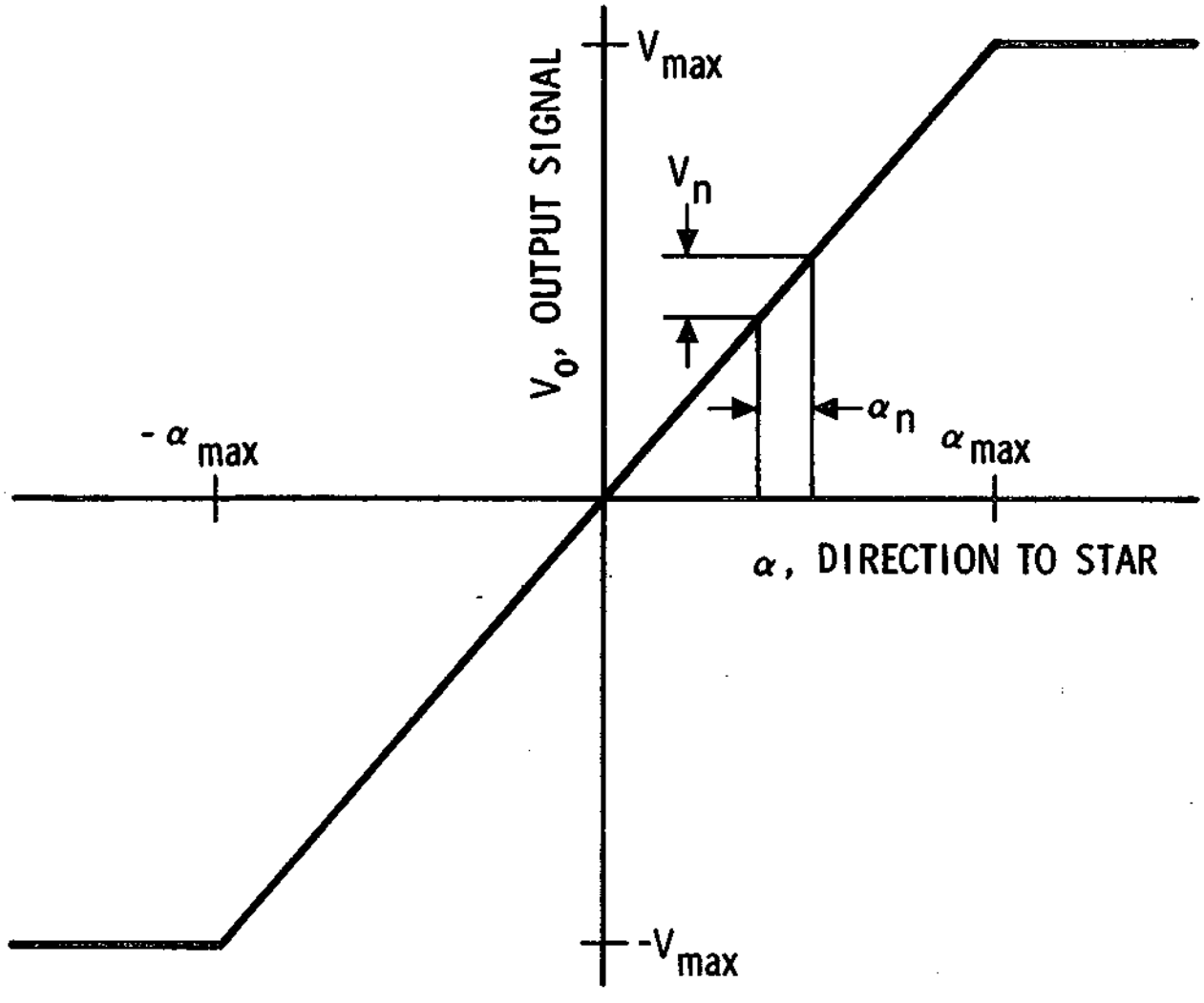
V_{max}
V_n
V_o, OUTPUT SIGNAL
α_n
$-\alpha_{max}$
α_{max}
α, DIRECTION TO STAR
$-V_{max}$

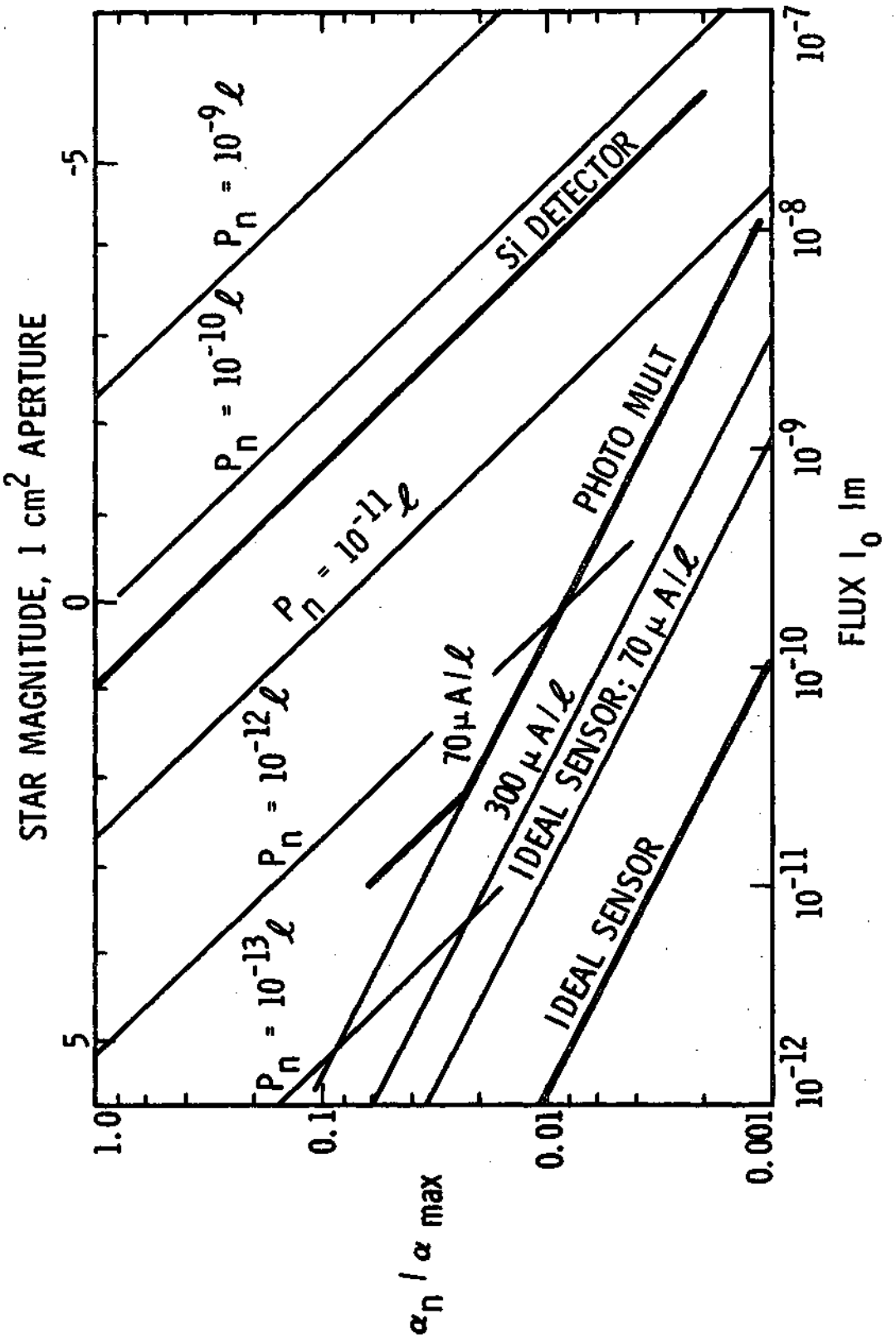

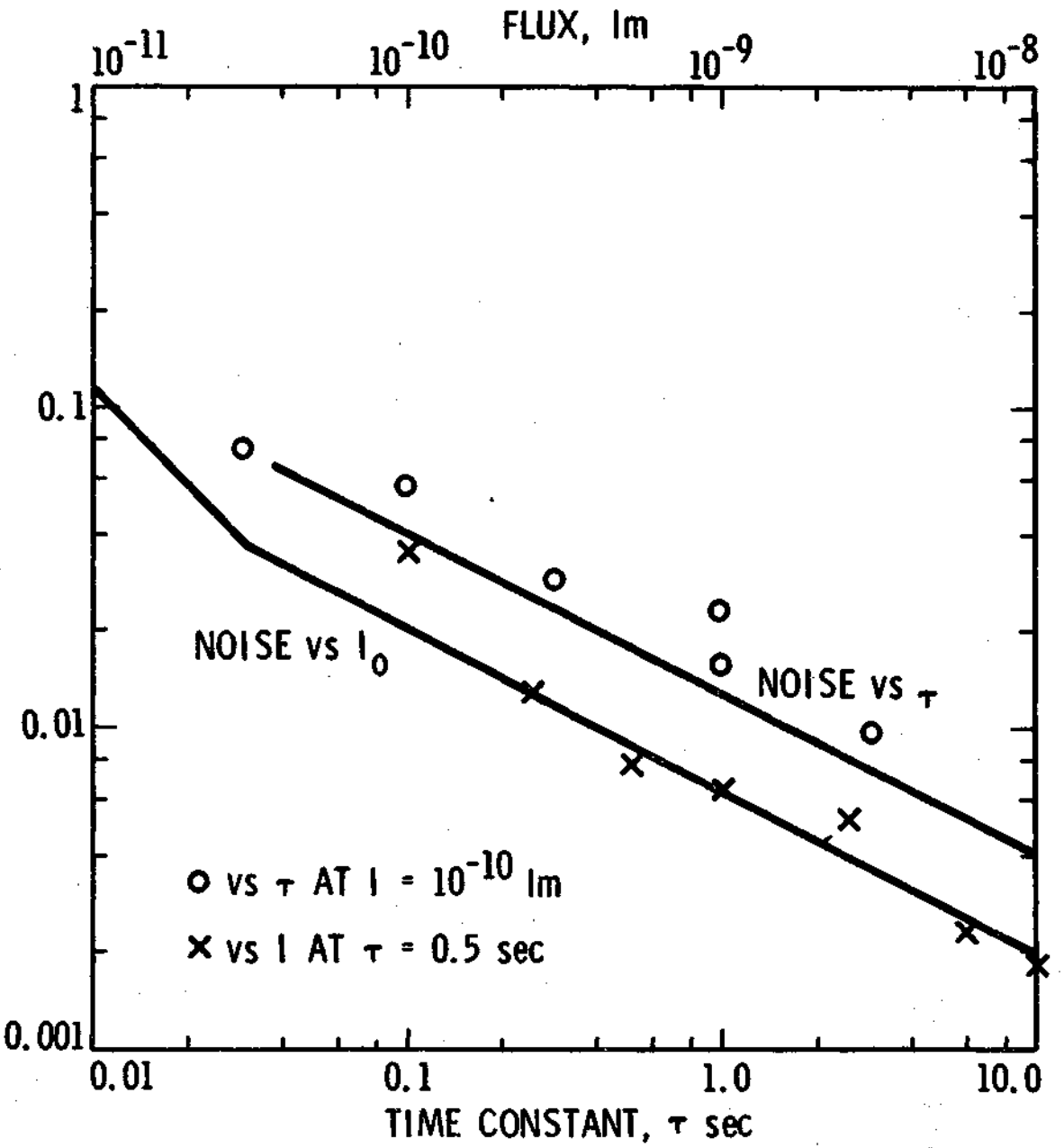
FLUX, Im
10^{-11}
10^{-10}
10^{-9}
10^{-8}
1
0.1
0.01
0.001
α_n / α_{max}
NOISE vs I_0
NOISE vs τ
o vs τ AT I = 10^{-10} Im
× vs I AT τ = 0.5 sec
0.01
0.1
1.0
10.0
TIME CONSTANT, τ sec

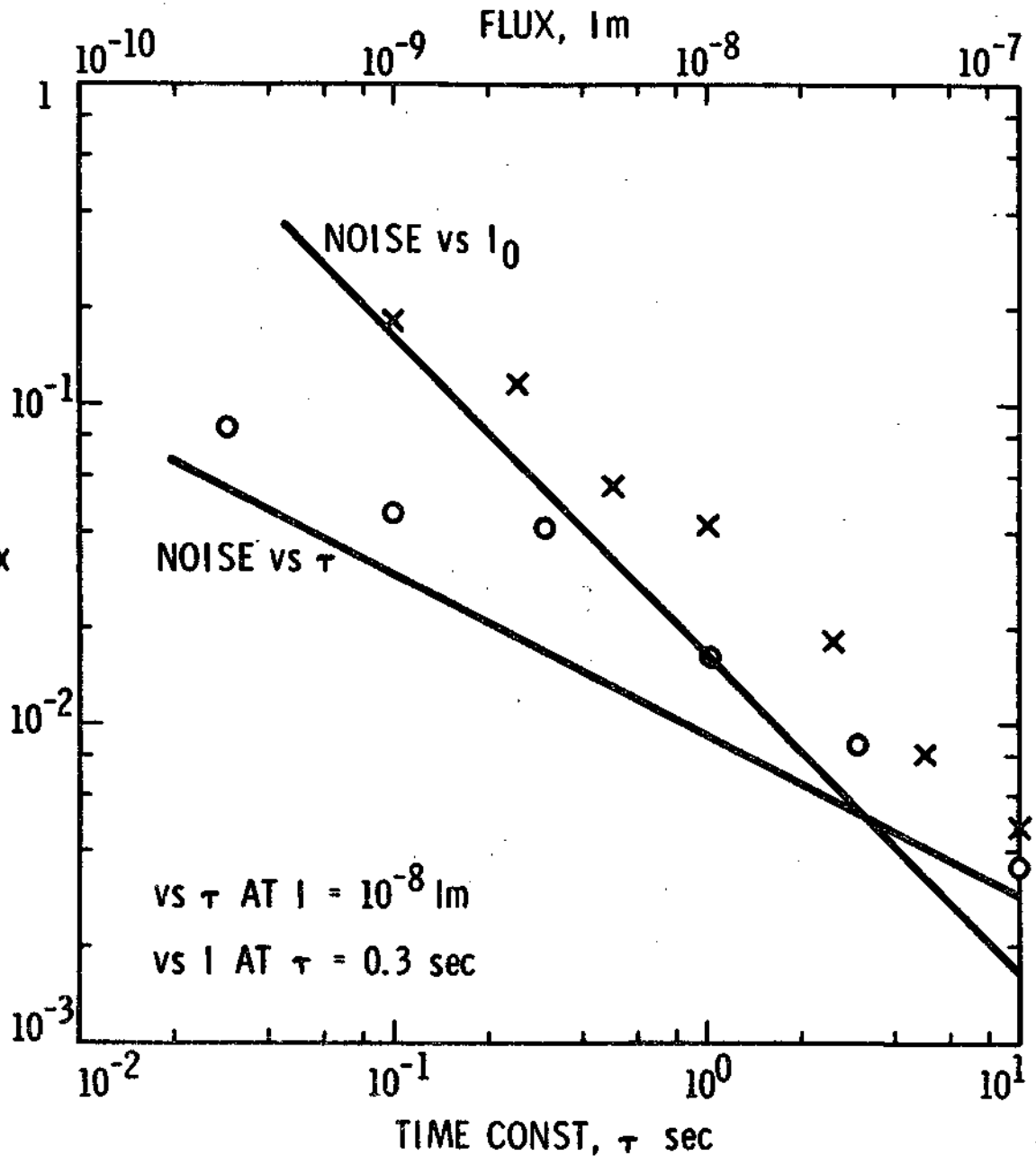
FLUX, Im
10^{-10}
10^{-9}
10^{-8}
10^{-7}
1
10^{-1}
10^{-2}
10^{-3}
α_n / α max
NOISE vs I_0
NOISE vs τ
vs τ AT I = 10^{-8} Im
vs I AT τ = 0.3 sec
10^{-2}
10^{-1}
10^{0}
10^{1}
TIME CONST, τ sec